A COUPLED ELECTRONIC-OPTICAL SIMULATION MODEL OF GAN-BASED LEDS

BY
MOHAMMED ZIA ULLAH KHAN

A Thesis Presented to the
DEANSHIP OF GRADUATE STUDIES

KING FAHD UNIVERSITY OF PETROLEUM & MINERALS
DHAHRAN, SAUDI ARABIA

In Partial Fulfillment of the
Requirements for the Degree of

MASTER OF SCIENCE
In
ELECTRICAL ENGINEERING

APRIL 2014

KING FAHD UNIVERSITY OF PETROLEUM & MINERALS

DHAHRAN- 31261, SAUDI ARABIA

DEANSHIP OF GRADUATE STUDIES

This thesis, written by **MOHAMMED ZIA ULLLAH KHAN** under the direction his thesis advisor and approved by his thesis committee, has been presented and accepted by the Dean of Graduate Studies, in partial fulfillment of the requirements for the degree of

MASTER OF SCIENCE IN ELECTRICAL ENGINEERING.

Dr. Mohammad A. Alsunaidi
(Advisor)

Dr. Ali Ahmad Al-Shaikhi
Department Chairman

Dr. Hussain Ali Al-Jamid
(Member)

Dr. Salam A. Zummo
Dean of Graduate Studies

Dr. Mohammad S. Sharawi
(Member)

14/5/14
Date

I dedicate this thesis to my beloved parents ***Mr. and Mrs. Mohammed Nusrath Ullah Khan*** *and my* ***Sister and Brothers*** *for their immense love, support and encouragement*

ACKNOWLEDGMENTS

All praises glory and gratitude is to Allah, the most Merciful and the most Beneficent.

I sincerely thank my advisor Dr. M. A. Alsunaidi for his teaching, guidance and encouragement during my course at KFUPM. I am grateful for all his support throughout my thesis with his patience and knowledge. I am also grateful to him for the valuable things that I have learned from him.

I would also like to thank my thesis committee members, Dr. Husain Ali Al-Jamid and Dr. Mohammad. S. Sharawi for their valuable advice, positive feedback and investing their precious time to serve as my thesis committee.

I would also like to thank Center of Research Excellence in Renewable Energy (CoRE-RE) at KFUPM for sponsoring my M. S education at KFUPM.

I thank KACST- Technology Innovation Center (TIC) on Solid State Lighting at KAUST for funding this research. I thank Dr. Boon S. Ooi, Principal Investigator of this research project at KAUST Photonics lab.

I am also grateful to my friends at KFUPM and fellow graduate students Tayyab, Waqas, Bagus, Irfan and Mohannad.

I also thank Electrical Engineering department for providing world class facilities for this research.

Finally, I owe my deepest gratitude to my parents for their love, support, encouragement and supplications, without which this thesis would not have been possible.

TABLE OF CONTENTS

LIST OF TABLES

LIST OF FIGURES

LIST OF ABBREVIATIONS

ADE : Auxiliary Differential Equation

CB : Conduction Band

DD : Drift Diffusion

DH : Double Heterojunction

EOT : Extra-ordinary Transmission

EOT : Extra-ordinary Transmission

EQE : External Quantum Efficiency

FDM : Field Dependent Models

FDTD : Finite Difference Time Domain

GaN : Gallium Nitride

LED : Light Emitting Diode

MH : Multiple Heterojunction

RM : Recombination Models

TF/SF : Total Field/Scattered Field

VB : Valence Band

ABSTRACT

Full Name : [Mohammed Zia Ullah Khan]
Thesis Title : [A Coupled Electronic-optical Simulation Model of GaN-based LEDs]
Major Field : [Electrical Engineering]
Date of Degree : [April 2014]

Solid State Lighting (SSL) technologies that utilize Light Emitting Diodes (LEDs) made from III-Nitride materials have emerged as an energy-efficient and reliable source of lighting because of unique III-Nitride material properties. Numerical modeling and simulation of such LEDs is needed to understand various physical mechanisms to enhance the performance and development of new III-Nitride devices.

In this thesis, we present a coupled carrier-photon model that accounts for the time-domain interactions between carrier transport and light emission in Gallium Nitride (GaN)-based LEDs that hasn't been reported so far. Carrier transport is modeled using the drift-diffusion formulation, whereas light emission and propagation is modeled using Maxwell's equations. The drift diffusion equation is solved self-consistently with Poisson equation. The carrier transport and photon emission are coupled by formulating an appropriate relation between radiative recombinations and dipole sources such that the strength of the dipole sources is given by the radiative recombination rates gauged to an appropriate value. This gauging factor is obtained by calibrating the External Quantum Efficiency (EQE) of homojunction GaN LED with the experimental value.

The coupled model is used to investigate homojunction and heterojunction AlGaN/ GaN LEDs. The maximum EQE of p-n and p-i-n homojunction LEDs is found to be $0.1755\ \%$ and $0.39\ \%$ respectively at a forward voltage of $4.267\ V$, whereas the AlGaN/GaN DH

LED demonstrated an EQE of $1.03\,\%$ at a forward voltage of $4.101\,V$. Utilizing this coupled model, GaN LEDs with improved recombination rates and optical power were investigated through Double Heterojunction (DH) and Multiple Heterojunction (MH) LEDs with array of metal contacts instead of single contact. The maximum EQE achieved for DH and MH LEDs with silver contact array is found to be $1.825\,\%$ and $5.295\,\%$ respectively. It is expected that this model will find applications in many device simulation cases where carrier-wave interaction is important.

ملخص الرسالة

الاسم الكامل: محمد ضياء الله خان

عنوان الرسالة: نموذج محاكاة إلكتروني-ضوئي مترابط لصمامات نتريد الجاليوم الضوئية

التخصص: الهندسة الكهربائية

تاريخ الدرجة: نيسان 2014

انتشرت تقنية الاضاءة المعتمدة على اشباه الموصلات ذات الانبعاث الضوئي خاصة تلك التي تستخدم مواد نيتريدات عناصر المجموعة الثالثة (النيتريد-3)، حيث تعتبر الآن مصدرا موثوقا للاضاءة لما لها من ميزات فريدة مثل توفير الطاقة و طول العمر الافتراضي. غير أن هناك حاجة ملحة لدراسة أداء هذه الصمامات الضوئية عن طريق المحاكاة و النمذجة باستخدام الطرق العددية من أجل فهم المبادئ الفيزيائية لها وتطوير أدائها وكفاءتها.

في هذه الأطروحة، نعرض نموذجا لعمل هذه الصمامات يعتمد على ربط حركة ناقلات الشحنة بالانبعاثات الضوئية في اطار واحد مترابط في المجال الزمني، الامر الذي لم يتطرق إليه قبل الآن. وتمت محاكات حركة ناقلات الشحنة باستخدام معادلات الانتشار و الازاحة، في حين تمت محاكاة انبعاث الضوء وانتشار الموجات الضوئية باستخدام معادلات ماكسويل. و لربط النموذجين تم اعداد طريقة جديدة للربط تعتمد على تعيين انبعاثات ضوئية قطبية ذات شدة معتمدة على معاملات التلاحم المضيء بين الالكترونات و الثقوب. و يتم تعيير هذه الشدة بالقياسات المعملية.

ولقد تم استخدام هذا النموذج المترابط في دراسة الكفاءة الضوئية لمجموعة من التركيبات للصمامات الضوئية المعتمدة على مادة نيترید الجاليوم بما في ذلك تركيبات p-n و p-i-n و P-n-N و P-p-N. تم تطبيق النموذج المترابط في دراسة حالتين لتركيبين جديدين يظهران الحاجة الى هذا النموذج: الاولى يكون فيها طبقة التوصيل الكهربائي ذات منافذ سطحية و الثانية تحتوي على تركيب P-n-N متكرر. واظهرت النتائج زيادة في الكفاءة الضوئية. ومن المتوقع أن يجد هذا النموذج مجالا واسعا في تحليل اداء التركيبات التي تكون فيها التأثيرات المزدوجة بين الموجة الضوئية وناقلات الشحنة موضع اهتمام.

CHAPTER 1

INTRODUCTION

Solid State Lighting (SSL) is expected to reduce electricity consumption for lighting by at least 50% [1]. This can be achieved through the development of light sources that consume less power or have high lumens per watt (lm/W) ratio. High power semiconductor light emitting diodes (LEDs) in the visible spectrum for SSL have been possible with the advent of direct bandgap III-Nitride semiconductor materials that have approached luminous efficiencies of ~100 lm/W [2]. Group III-Nitride semiconductor materials such as Gallium Nitride (GaN), Indium Nitride (InN) and Aluminum Gallium Nitride (AlGaN) have been used to produce high brightness LEDs for SSL applications and are the subject of current research in SSL to improve device performance and to achieve high LED efficiencies [3], [4]. Due to the unique material properties of these semiconductors, they have been demonstrating high internal quantum efficiencies (IQE) compared to the commercial Silicon carbide (SiC) LEDs.

Future development and improvements in GaN LEDs require a deeper understanding of the physical nanoscale mechanisms and internal physics of the device. The parameters needed to improve the device performance can be investigated through numerical simulations of advanced models. The challenges that occur in modeling such devices are knowledge of a large number of III-Nitride material parameters and integration of carrier transport with optical domain. Numerical simulations help in developing the link between material properties and the performance of the device. They can also help to understand the nanoscale effects influencing the LED performance that cannot be explained experimentally. Therefore, advanced numerical simulation models of such LEDs have to be developed for future advancements. In this thesis, a coupled carrier-photon simulation model for GaN based LEDs will be developed to study and analyze LED structures for SSL applications.

1.1 Highlights of GaN LED Research

The advent of semiconductor LEDs made from III-Nitride compounds helped to improve LED efficiencies compared to the conventional fluorescent and incandescent light bulbs and have attracted attention worldwide to achieve highly efficient LEDs with low power consumption. Figure 1.1 shows the improvement in LED efficiencies with time using different semiconductor materials. It can be observed that LEDs made from III-Nitride materials have been achieving higher efficiencies and hence SSL has been very efficient and environment friendly. This was possible because of the direct bandgap nature of these materials, due to which the radiative recombinations or band to band recombinations occur more efficiently compared to indirect bandgap materials such as Silicon Carbide (SiC) or Silicon (Si). GaAs and GaAsP were the first III-V materials used to produce LEDs that emit red and infrared light. Later, III-V compound materials such as AlGaAs or AlGaInP have been used to emit red, yellow and orange light. Later in the early 1990s, the achievement of p-type doped GaN material [5] and the development of high power GaN blue LEDs [6], [7] have attracted researchers worldwide to investigate III-Nitride LEDs.

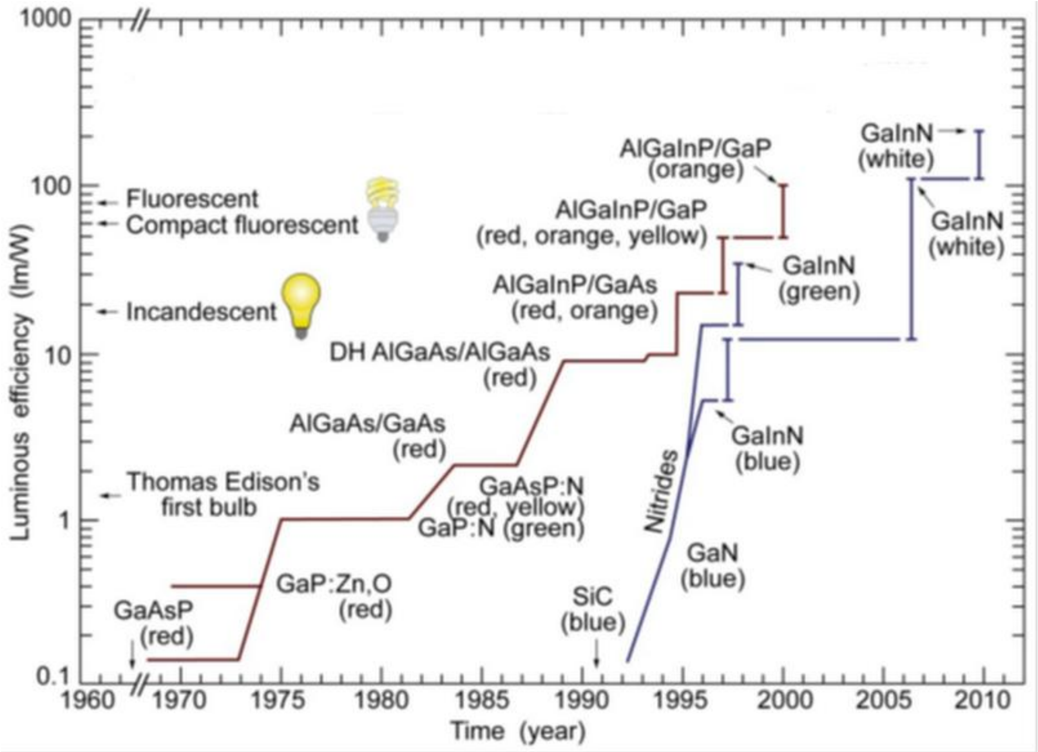

Figure 1.1 Lighting sources and their efficiencies with time (adapted from [8], [9])

Following the above developments, numerous LED structures and devices based on Nitride materials have been investigated such as GaN/AlGaN heterojunction LEDs, Quantum Well (QW) and Quantum Dot (QD) LEDs and are studied for improvements in terms of internal quantum efficiencies (IQE) and extraction efficiencies. These studies involved both experimental investigations and numerical simulations with advanced models.

1.2 GaN Material for Light Emitting Devices

GaN materials have been extensively used to produce visible and Ultra-violet (UV) LEDs because of their unique material properties. Table 1.1 illustrates the conventional and the wide bandgap material properties. The large band gap energies and high electric breakdown fields of such wide bandgap materials compared to conventional semiconductors, allow them to operate at high supply voltages and withstand high temperatures. As discussed previously, they also exhibit a direct bandgap which results in efficient light emission.

Table 1.1 Comparison of conventional and wide bandgap semiconductors at 300 K ([10], [11]), HS-Heterostructure.

Property	GaN and AlGaN/ GaN	Silicon Carbide	Diamond	Silicon	Gallium Arsenide and AlGaAs/ InGaAs
Bandgap energy, E_g (eV)	3.44	3.26	5.45	1.12	1.43
Electric breakdown field, E_c (MV/cm)	3	3	10	0.3	0.4
Saturated drift velocity, electrons,v_{sat} $(\times 10^7 cm/s)$	2.7	2.0	2.7	1.0	2.1
Electron mobility, μ_n $\left(\frac{cm^2}{V-s}\right)$	900 2000 (HS)	700	4800	1500	8500 10,000 (HS)
Thermal conductivity κ $\left(\frac{W}{cm-K}\right)$	1.3-2.1	3.7-4.5	22	15	0.5
Relative permittivity , ϵ_r	9.7	10.1	5.5	11.8	12.8

1.2.1 Light emission at specific wavelengths

The use of AlGaN/InGaN alloys as active layers with different aluminum or indium content can provide light emission at desired wavelengths. This can be explained from the bandgap properties of III-Nitride and its alloys as shown in Figure 1.2 to Figure 1.4. This emission depends on the bandgap of the material used as the active region of LED. The energy bandgap of III-Nitride materials can be varied in wide range i.e. 0.65 eV to 6.13 eV as shown in Figure 1.2. For example, the bandgap of GaN when alloyed with AlN can be varied from 3.42 eV to 6.13 eV or the emission shifts towards UV as shown in Figure 1.2 and Figure 1.3.

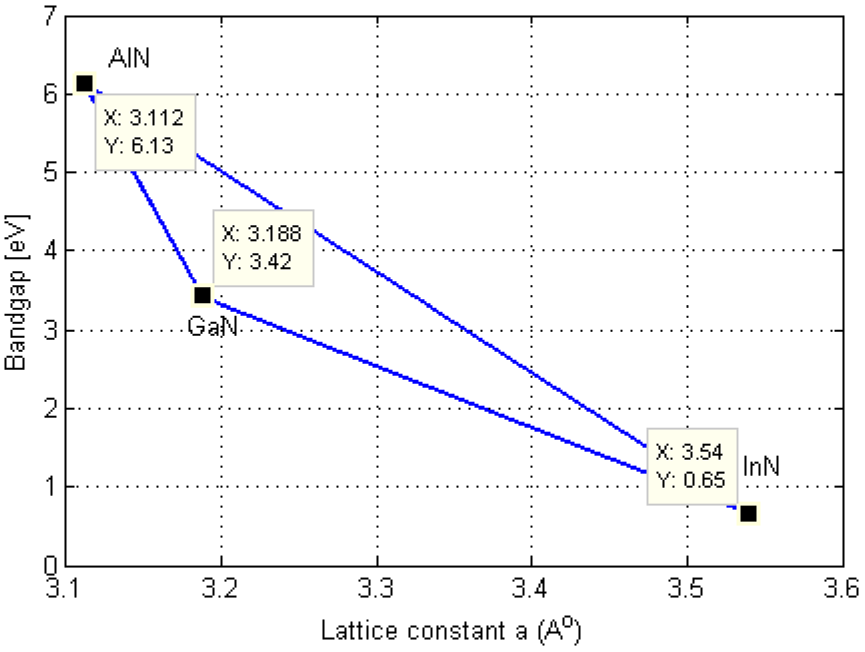

Figure 1.2 Energy bandgap versus lattice constant of III- Nitride and its alloys.

This bandgap depends on the lattice constant of the material. Therefore, the variation in the bandgap by alloying III-materials results from different lattice constants. Therefore, for GaN LEDs emitting in the UV range, alloying GaN with AlN is most suitable, whereas for LEDs emitting in red or blue, InGaN materials are preferred.

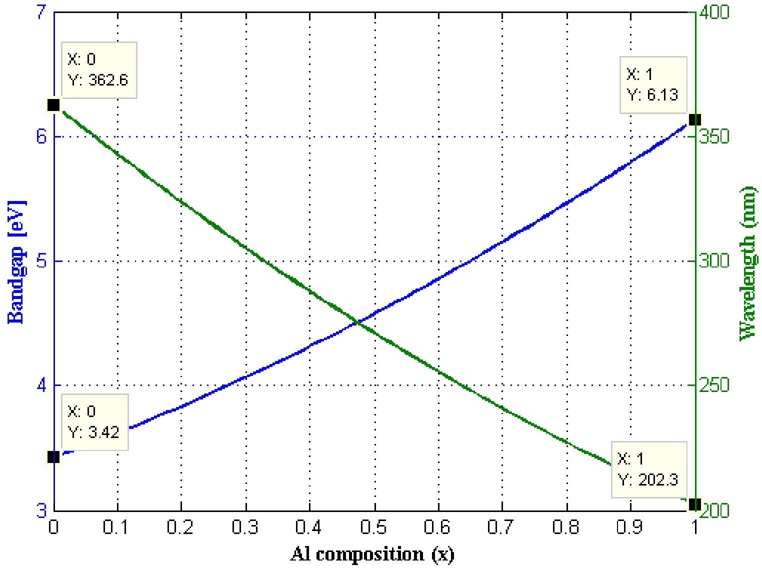

Figure 1.3 Bandgap or emission versus Aluminum (Al) composition of AlGaN alloy.

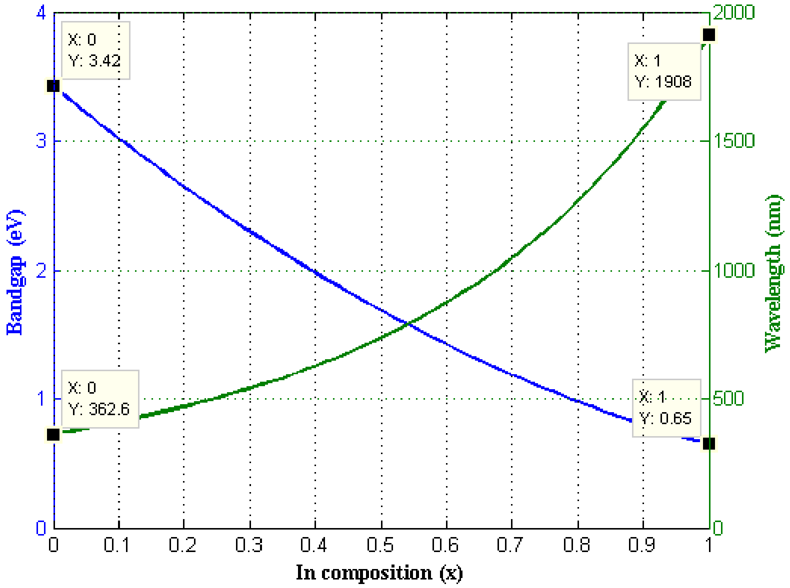

Figure 1.4 Bandgap or emission versus Indium (In) composition of InGaN alloy.

1.3 Analysis of Optoelectronic Devices

With the rapid increase in the computational tools, numerical simulation techniques are becoming more efficient and accurate in the development of optoelectronic devices. Numerical simulations help shorten the development cycle of products and also tend to reduce huge costs that incur during analysis with complicated experimental setups. The time domain analysis of optoelectronic devices can help to produce multi wavelength optical characteristics in one single run which is very important for simulating coupled electronic-photonic devices. In this work, the time domain simulation of GaN LEDs is developed using the Finite-Difference Time Domain (FDTD) numerical method that is very popular in simulation of photonic devices and their verification.

The numerical analysis of LEDs consists of a combined simulation of carrier transport that describes the behavior of carriers under the influence of external fields, and an optical model describing the photon emission and propagation in such devices. The important parameters defining the performance of GaN LEDs obtained from the numerical simulation model are as follows:

1. Internal quantum efficiency (IQE)

$$\boldsymbol{\eta}_{IQE} = \frac{\text{Photons generated inside the active region}}{\text{Total number of electrons injected into the LED}} \tag{1.1}$$

2. Optical/ Light Extraction efficiency (LEE)

$$\eta_{\mathrm{EXE}} = \frac{\text{Photons emitted outside the LED}}{\text{Photons generated inside the active region}} \tag{1.2}$$

3. External quantum efficiency (EQE)

$$\eta_{\mathrm{EQE}} = \frac{\text{Photons emitted outside the LED}}{\text{Total number of electrons injected into the LED}} = \eta_{\mathrm{EXE}} \times \eta_{\mathrm{IQE}} = \frac{\text{Output Optical Power}}{\text{Input Electrical Power}} \tag{1.3}$$

4. Radiative and non-radiative electron- hole pair recombination rates.
5. Optical carrier generation rate

$$\mathrm{G_{opt}} = \frac{\text{Power density absorbed at each point}}{\text{Photon energy}} = \frac{-\nabla.\boldsymbol{S}_{\mathbf{av}}}{\mathrm{E_{ph}}} = -\frac{1}{2}\omega|\mathbf{E}|^2\mathrm{imag}(\varepsilon) \tag{1.4}$$

where $\mathbf{S_{av}} = \frac{1}{2}\, Real\,(\boldsymbol{E} \times \boldsymbol{H})$ is the intensity distribution, $\mathrm{E_{ph}} = \frac{hc_0}{\lambda}$ is photon energy, ω and ε are frequency and dielectric constant, respectively.

6. Emission intensity and spectrum.

1.3.1 Carrier transport simulation

With a rapid decrease in the size of electronic devices and increased complexity, the device development through experimental approach may become expensive and time consuming. However, the analysis of these devices can be effective through use of numerical simulations that can help to investigate the device characteristics rigorously before fabrication. These numerical simulations require advanced models to describe transport of electrons and holes in these devices. The carrier transport or the behavior of charges under external fields can be described through a set of coupled partial differential equations that can be derived from the semi classical Boltzmann Transport Equation (BTE), that describes the carrier motion under applied fields as an accelerating (classical) and scattering (quantum) events [12] .

The development of powerful computational tools has improved the numerical device simulations from one-dimensional models to more realistic three dimensional simulations. Several approaches have been used to numerically solve the carrier transport equations: Monte-Carlo methods, finite-difference (FD) and finite-element (FE), Quasi Fermi level models and quantum transport models [12]–[14]. However, these models involve steady state analysis that solves the carrier concentrations from the Fermi levels instead of time dependent continuity equations. Therefore, to analyze the coupled electronic-optical characteristics of GaN LEDs, we formulate a time domain device model that can be coupled with time varying electric and magnetic fields.

The drift diffusion (DD) transport model for semiconductor devices is obtained from the BTE which gives the self-consistent solution of the following coupled equations [15].

1. Poisson's Equation- relating the electric field to charge distribution

$$\nabla.(\varepsilon\nabla V) = -\rho \tag{1.5}$$

where V is electrostatic potential, ε is dielectric permittivity and ρ is volume charge density, $\nabla.(.)$ is the divergence operator and $\nabla(.)$ is the gradient operator.

2. Current density equations- representing the drift and diffusion of carriers.

$$\boldsymbol{J_n} = -qn\mu_n \nabla V + qD_n \nabla n \tag{1.6}$$

$$\boldsymbol{J_p} = -qp\mu_p \nabla V - qD_p \nabla p$$

where J_n and J_p are electron and hole current densities, n and p are electron and hole densities, q electronic charge magnitude, $\mu_{n(p)}$ and $D_{n(p)}$ are carrier mobility and diffusion coefficient.

3. Continuity equations- electron and hole carrier densities.

$$\frac{\partial n}{\partial t} = G_n - R_n + \frac{1}{q}\nabla.\boldsymbol{J_n} \tag{1.7}$$

$$\frac{\partial p}{\partial t} = G_p - R_p - \frac{1}{q}\nabla.\boldsymbol{J_p}$$

where $G_{n(p)}$ and $R_{n(p)}$ are electron-hole pair generation and recombination rates respectively.

The solution of these coupled equations describes the carrier transport in any semiconductor device. For a specific semiconductor material or a structure, its properties can be incorporated in these equations to understand the electronic behavior.

1.3.2 Optical simulation

The electromagnetic phenomena in any optoelectronic device are described through Maxwell's equations.

$$\nabla \times \mathbf{H} = \mathbf{J}_{ext} + \frac{\partial \mathbf{D}}{\partial t} \tag{1.8}$$

$$\frac{\partial \boldsymbol{B}}{\partial t} = -\nabla \times \boldsymbol{E} \tag{1.9}$$

$$\nabla . \mathbf{D} = \rho_{ext} \tag{1.10}$$

$$\nabla . \mathbf{B} = 0 \tag{1.11}$$

with,

$$\boldsymbol{D} = \varepsilon \boldsymbol{E} \ and \ \boldsymbol{B} = \mu \boldsymbol{H} \tag{1.12}$$

where $\boldsymbol{D}, \boldsymbol{E}, \boldsymbol{B}, \boldsymbol{H}$ **and** $\boldsymbol{J_{ext}}$ are the electric flux density, electric field intensity, magnetic flux density, magnetic field intensity and current density vectors respectively.

Optical simulation of LEDs is required to understand the spontaneous light emission and propagation that is generated through the recombination of charge carriers in the active region. A multi wavelength simulation can be performed in one run by solving Maxwell's equations in the time domain. Optical simulations provide important parameters such as optical generation rate or absorbed power, external quantum efficiencies and emission spectrum that are needed to understand the light emission properties in GaN LED structures and to improve the performance characteristics.

The solution of Maxwell's equations can describe the optical or EM wave propagation. The coupled partial differential equations can be solved through well-known electromagnetic numerical techniques such as Beam propagation method (BPM), Finite

Difference Time Domain (FDTD), Method of Lines (MOL), Finite Element Method (FEM), Method of Moments etc. [16]. The time domain carrier-wave interactions inside GaN LEDs can be efficiently modeled using FDTD method because of several advantages over other methods shown in Table 1.2.

Table 1.2 Comparison of numerical techniques for solving coupled partial differential equations.

Numerical technique	FDTD	FEM	MOL
Method Principle	Based on finite difference approximations for spatial and temporal derivatives.	Based on variational methods that divide the domain into finite triangular sub-regions.	Based on finite difference approximations only for spatial derivatives, whereas the time derivatives are kept continuous.
Advantages	Wide range of frequency problems in one run, Can easily model linear and non-linear materials, Robust and efficient for electromagnetic	Easily handles complicated geometries, Approximation is better than FDM, Easily includes dissimilar material properties.	Simple and easy to implement, Efficiently used to solve initial value problems

	wave interactions.		
Disadvantages	Large computational time with fine meshes requires to model time source explicitly, cannot easily handle complicated geometries.	Defining absorbing boundary conditions, Choosing proper element size, Complex programming compared to FDTD method, Parallelizing FEM code is also difficult.	Curved geometries can’t be approximated efficiently, stability issues in transient problems, semi-analytical technique.
Modeling Applications	Photonic devices, Nanoplamonics, Imaging, Linear and non-linear wave propagation problems, Wireless communication devices.	Electromagnetic problems, Heat transfer and computational fluid dynamics problems.	Photonic devices, Optical waveguides, Fluid dynamic problems, Non-linear wave propagation problems.

Therefore, in this thesis, FDTD numerical technique is used to solve EM wave equations for light propagation and emission and the DD transport model for carrier transport in GaN LEDs.

1.4 Literature Review

GaN has been a very promising material for high brightness and efficient light sources such as visible and UV LEDs and Laser diodes (LDs) [17]. It was not possible until 1990's to obtain a p-n junction GaN LED due to difficulty in obtaining p-type doping in GaN. However in 1989, p-type doped GaN was achieved by doping GaN with Magnesium (Mg) using the low-energy electron-beam irradiation (LEEBI) treatment and a p-n homojunction UV LED at a peak wavelength of 375 nm and a smaller peak at 420 nm (blue) was also demonstrated [5]. In the 1990's, Nakamura *et al.* reported high power GaN blue homojunction LED where the electroluminescence of GaN p-n homojunction LED in blue spectra was improved further by increasing the p-type doping and using a GaN buffer layer [6].

Later, double heterostructure (DH) blue LEDs were presented that had a strong blue emission and high external quantum efficiencies compared to homojunction LEDs [18]. This was achieved by using low band gap material such as InGaN as active layer sandwiched between two higher bandgap materials (GaN). This increases the electron-hole pair recombinations in the active region because of the low energy bandgap of active layer compared to other layers. Following these developments, the researchers have aimed at improving internal quantum efficiencies of GaN based LEDs for emission in visible wavelengths through use of quantum structures in the active region such as single and multiple quantum wells and quantum dots [19], [20] separated by barrier layers that prevent the escape of carriers from the active region. The research in this area aims at providing high brightness and efficient visible and UV LEDs for SSL applications.

The development of numerical models is important for LED optimization and development and also to explain physical mechanisms through formulation of theoretical models that can explain these affects. Numerous simulation studies have been investigated for electronic, optical and thermal problems using commercial simulation softwares such as APSYS, COMSOL, SiLENSE etc. These simulation programs are based on the drift diffusion (DD) transport model, polarization models for heterostructure LEDs and radiative and non-radiative recombination models. These programs use approximate ray tracing models to determine the optical characteristics such as photon extraction, emission spectrum and optical power. To analyze a practical LED structure, a full-wave simulation model consisting of both the carrier transport and an appropriate optical model coupled with the carrier transport have to be investigated. In this work, we focus on developing a complete optoelectronic model that simulates electronic and optical properties of GaN LED structures in time domain and also incorporates the coupling between the optical and electronic parameters.

Thus, numerical simulations based on the DD transport model have been investigated for development and improved performance of these devices. 3D simulations of UV LEDs made from AlGaN/GaN quantum well structures were demonstrated for short range communication and SSL applications in [21]. A blue InGaN LED was studied using APSYS simulation program for optical performance and quantum efficiencies [22]. This LED had different compositions of Indium in the GaN-InGaN-GaN barrier layer and an optimum value of indium composition and number of barrier sub layers to obtain good optical performance. The studies performed using such simulation models focused on major electronic parameters i.e. recombination rates or internal quantum efficiency. Various other issues were addressed using these simulation studies such as:

1. The decrease in the internal quantum efficiencies (IQE) with the increase in the injection current termed as efficiency droop [23] .
2. The effect of joule heating or temperature reducing the LEDs IQE [24].
3. The effect of thickness of intrinsic GaN layers between multiple quantum wells (MQW) and p-GaN layer on light output powers [25]. The optimum thickness of these layers was determined to increase optical power and reduce the non radiative recombinations.
4. The effect of built-in spontaneous and piezoelectric polarizations on the luminescence [26]. These charges develop a strong built-in electric field at the junction that reduces the emission energies of QW or active layers.
5. Electron leakage effects on IQE [27]. The leakage of electrons from active layers to p-type layers captures holes in the p-type layer before these holes reach active layers. Thus, this reduces the radiative recombinations in the active region and therefore the IQE.

Simulation studies focusing on improving the optical characteristics such as light extraction efficiencies in a GaN LED structure have also been addressed. Photonic crystal LEDs i.e. periodic arrangement of materials of different refractive indices on top of LEDs that can alter the propagation of photons such that total internal reflections at air/emitter interface are reduced have been demonstrated [28]. Light extraction efficiencies were also improved by using metal gratings, surface roughening or texturing and these studies were demonstrated through FDTD simulations [29], [30]. 3D FDTD simulation studies of LED structures that can increase the light output power were investigated through patterning in sapphire substrates such that the light can be scattered or redirected inside the LED and escape from GaN layers [31].

Therefore, these studies focused on improving internal quantum efficiencies or extraction efficiencies either through electronic simulation or optical simulations but not both simultaneously. Thus, using the advanced simulation models, the issues were demonstrated and various solutions were proposed through these studies. The following deficiencies were observed in such simulation studies.

- The simulation models that link photon emission with the carrier transport describing the complete electronic and optical characteristics were missing.
- Appropriate relation between electron-hole pair recombinations and current density inputs to the optical model was absent.
- The dependence of light extraction efficiencies on electronic parameters was not demonstrated.
- The dependence of carrier mobilities and diffusion coefficients on applied bias was not classified.
- The effect of hole transport parameters on GaN LED performance was missing.

In conclusion, the following points are made from the literature

- GaN and its alloys are being extensively used for developing high brightness and efficient LEDs.
- Simulation studies have been made for GaN/AlGaN heterostructures and QWs.

- These simulation models were based on DD transport models, built- in polarization models for LED heterostructures, quantum mechanical models and ray tracing models for photon extraction.
- The major limitation and deficiency found in such simulation models is the combined carrier-wave interactions and representation of time dependent electron-hole pair recombinations to dipole sources.
- The simulation models that link electronic transport model to the optical model for LED simulation have not been reported so far.

Therefore, this work attempts to develop a coupled electronic-optical simulation model for GaN LEDs. A time domain electronic model should be formulated in order to perform simulation studies in conjunction with optical model using FDTD numerical technique.

1.5 Thesis Objectives

The main contribution of this work is to develop a coupled time domain electronic-optical simulation model of GaN based LEDs that can be used to analyze the performance of complex GaN LED structures using finite difference time domain (FDTD) simulation technique.

The specific objectives are as follows:

1. Conducting an extensive literature survey on the numerical simulation of III-Nitride light emitting diodes pointing out limitations and deficiencies.
2. The development of an electronic model representing the carrier transport using drift-diffusion current equations and field-dependent parameters.
3. The development of a coupled multi-dimensional simulator that combines both the electronic and optical models, to study and analyze electrical and optical characteristics of III-Nitride LEDs.
4. Presentation of an overall evaluation of the capabilities of the coupled model indicating its strengths and limitations.
5. Extracting important results and conclusions from the developed model.

1.6 Thesis Organization

This thesis is organized as follows.

Chapter 1 discusses the overview of GaN LED technology and the need for research on these devices. It also explains the importance of numerical modeling and simulation for development of these devices. It also describes the objectives of this thesis and literature. Chapter 2 explains the theory of numerical models that are needed to simulate carrier transport and photon emission in GaN LEDs.

Chapter 3 describes the development of the time domain FDTD algorithm for electronic and optical model that simulate GaN device characteristics.

Chapter 4 discusses the electronic carrier transport simulation results of homojunction and heterojunction GaN LED structures.

Chapter 5 discusses the optical model simulation results of homojunction and heterojunction GaN LED structures.

Chapter 6 discusses the coupling method that combines the carrier transport with photon emission. It discusses the coupled model simulation results for the LED structures discussed in Chapters 4 and 5.

In Chapter 7 the coupled model is used to investigate GaN LEDs for improved EQE by using DH LEDs with sub-wavelength metal contact array and multiple heterojunction (MH) LEDs as two applications.

Chapter 8 contains summary and conclusions. It also describes the extension of this work.

CHAPTER 2

THEORETICAL BACKGROUND

This chapter explains the basic semiconductor transport models used in electronic simulation of GaN LEDs. It includes the drift diffusion (DD) model, field dependent models, electron-hole pair recombination models and polarization models required for carrier transport simulation. This chapter also discusses the dispersive material models required for simulation of light propagation inside GaN LEDs.

2.1 Introduction

In this work, a time domain simulation model is developed to numerically analyze GaN LED structures. This consists of an electronic model representing the carrier transport and an optical model for photon emission and optical characteristics. The electronic model is based on DD transport model. The dependence of carrier transport parameters of GaN on the applied electric field is incorporated in this model. There are various analytical models that have been proposed to incorporate the electronic transport properties of III-Nitride materials in device simulation. In III-Nitride materials, the dependence of mobilities and diffusion coefficients on applied bias arises due to the electronic band structures and scattering mechanisms such as intervalley scattering, piezoelectric, phonon scattering, carrier-carrier, and plasmon scattering mechanisms [32]. For example, at low electric fields, the electron drift velocity increases linearly due to rare polar optical phonon emissions that causes weak electron effective mass and high drift velocities. At higher fields, the electrons are excited to higher valleys as they gain more energy and become heavier and the possibility of their collisions increases which slows them and reduces their steady state velocities such that a negative differential mobility region is observed.

The commonly used analytical models to describe such behavior of carrier velocities are the Canali and the transferred electron models [33]. Improved models have also been proposed that fit the available experimental data for electronic transport in III-Nitride materials. For example, the field dependent mobility models in GaN and its alloys have been proposed by using the Monte Carlo simulation techniques and the proposed models were in good agreement with the experimental data [32]–[35]. Analytical models for both low field and high field mobility in GaN have been presented in [34]. However, it is quite challenging to model the hole transport in GaN and there is no satisfactory model that includes both low field and high field transport. A simple model is used to represent the hole- velocity field characteristics that is described by standard Caughey-Thomas formula for the drift velocity is used in this work since this model fits the available experimental data for the hole velocity-field characteristics [36]. The DD simulator uses the Arora model to incorporate the effect of doping concentration and crystal temperature on the low field electron and hole mobilities [37]. The diffusion coefficient is usually deduced from Einstein’s equation. However, this is valid only at low electric fields. Thus, in this work the available Monte Carlo simulation data for electron diffusion coefficient versus applied electric field is also employed in the DD simulator [38].

2.2 Carrier transport models

The simulation of carrier transport in an electronic device can be modeled by solving the classical semiconductor equations i.e. drift diffusion (DD) equations and carrier continuity equations. These equations are obtained from the first two moments of the Boltzmann Transport equations (BTE) [15]. The BTE is a distribution function representing the electron or hole distribution or their statistical behavior under non equilibrium condition. Monte Carlo simulations and quantum mechanical numerical models have been used to investigate the non-equilibrium carrier transport in electronic devices [14]. Finite element and finite difference methods for solving the partial differential semiconductor equations have also been used for modeling of semiconductor devices [12], [13], [43].

In this work, the carrier transport in GaN LEDs is modeled using the time domain drift diffusion model discussed in the following section.

2.2.1 Drift Diffusion model

The drift diffusion model is a simplified model obtained from the moments of the BTE. It is solved in conjunction with Poisson's equations, current density equations and carrier continuity equations [15]. Thus, the basic electronic simulation of GaN LEDs is based on the following equations (equations (2.1)-(2.6)).

Poisson's equation relates the electrostatic fields with the charge distribution as

$$\nabla.(\varepsilon \nabla V) = q\left(n - p + N_A^- - N_D^+ \pm N_f\right) = -\rho \tag{2.1}$$

$$\boldsymbol{E} = -\nabla V \tag{2.2}$$

The continuity equation describes the change in electron and hole densities with time and is given by

$$\frac{\partial n}{\partial t} = G_n - R_n + \frac{1}{q}\nabla.\boldsymbol{J_n} \tag{2.3}$$

$$\frac{\partial p}{\partial t} = G_p - R_p - \frac{1}{q}\nabla.\boldsymbol{J_p} \tag{2.4}$$

The current density for electrons and holes is given by the drift diffusion (DD) equations

$$\boldsymbol{J_n} = qn\mu_n\mathbf{E} + qD_n\nabla n \tag{2.5}$$

$$\boldsymbol{J_p} = qp\mu_p\mathbf{E} - qD_p\nabla p \tag{2.6}$$

where,

V is the electrostatic potential in Volts, $\boldsymbol{E}$ is the electrostatic field in V/m

ε is the dielectric permittivity of the medium in F/m, q is the unit charge in C

n is the electron density in m^{-3}, p is the hole density in m^{-3}

N_A^- is the ionized acceptor impurity concentration in m^{-3},

N_D^+ is the ionized donor impurity concentration in m^{-3}

N_f is fixed interface charge density due to spontaneous and piezoelectric polarization in m^{-3}.

G_n and R_n are electron generation and recombination rates in $m^{-3}s^{-1}$

G_p and R_p are hole generation and recombination rates in $m^{-3}s^{-1}$

$\boldsymbol{J_n}$ and $\boldsymbol{J_p}$ are electron and hole current densities in A/m^2 .

μ_n and μ_p are the electron and hole mobilities in $m^2V^{-1}s^{-1}$

D_n and D_p are the electron and hole diffusion coefficients in m^2s^{-1}

The solution of the above equations is obtained using the FDTD algorithm that is discussed in chapter 3.

2.2.2 Field dependent models

The optimization of GaN devices through numerical simulations requires utilization of optical and electrical material properties and reliable models to describe them. The intense research on the nitride materials over the past decade has made it possible to discover a large number of material parameters. These parameters can be incorporated in numerical simulations through analytical models that fit the experimental data. This section discusses the transport parameters of electrons and holes and their analytical models that can be integrated in the DD model.

2.2.2.1 Field dependent carrier mobilities

The analytical models representing the dependence of low field and high field electron mobility on doping, temperature and electric field have been presented in [32], [33], [35], [36]. These models were fitted with the available experiment data and found to be appropriate to be used in numerical simulators.

Thus, the low field and high field electron and hole mobility models [35], [36] have been incorporated into the DD model. The doping and temperature dependent low field electron mobility of GaN is based on the Arora model [37] and is given as [35]

$$\mu_{n0}(T,N) = \mu_{min}\left(\frac{T}{300}\right)^{\beta_1} + \frac{(\mu_{max}-\mu_{min})\left(\frac{T}{300}\right)^{\beta_2}}{1+\left[\frac{N}{N_{ref}\left(\frac{T}{300}\right)^{\beta_3}}\right]^{\alpha\left(\frac{T}{300}\right)^{\beta_4}}} \tag{2.7}$$

where, μ_{n0}, T and N are low field electron mobility, temperature and doping concentration and the low field parameters are given in Table 2.1. $N_{ref} = 10^{17}$ is the fitting parameter which is valid for this model for doping concentrations of $1 \times 10^{16} - 1 \times 10^{18}\ cm^{-3}$.

Table 2.1 Low field mobility parameters of GaN [35].

Parameter	Value
$\mu_{max}\ [cm^2V^{-1}s^{-1}]$	1460.7
$\mu_{min}\ [cm^2V^{-1}s^{-1}]$	295
α	0.66
β_1	1.02
β_2	3.84
β_3	3.02
β_4	0.81
$N_{ref}\ [cm^{-3}]$	10^{17}

The high field mobility (Figure 2.1 a) is given by the following model [35]

$$\mu_n(E) = \frac{\mu_{n0}(T,N) + \vartheta^{sat}\frac{E^{n1-1}}{E_c^{n1}}}{1 + \left(\frac{E}{E_c}\right)^{n_1} + a\left(\frac{E}{E_c}\right)^{n_2}} \tag{2.8}$$

where, μ_{n0} is the low field mobility which is doping and electron temperature dependent and is obtained using equation (2.7). ϑ^{sat} is the saturation velocity, E_c is the critical field i.e the field value above which the drift velocity changes its slope from positive to negative, and a, n_1, n_2 are the fitting parameters.

Table 2.2 High field mobility parameters of GaN [35].

Parameter	Value
ϑ^{sat} $[\times 10^{7} cm/s]$	1.9064
E_c $[kV/cm]$	220.8936
n_1	7.2044
n_2	0.7857
a	6.1973

Similarly, the hole mobility models used in the simulator are given by the following expressions [36]

$$\mu_{h0} = \mu_{ho}\,(T, N_i) = \frac{\mu_d}{1+\left(\frac{N_i}{N_0}\right)^{A^*}} \;, N_i = N_a + N_d \qquad (2.9)$$

where,

$$\mu_d = A_d\left(\frac{T}{T_0}\right)^{\alpha_d}, \;\; N_0 = A_N\left(\frac{T}{T_0}\right)^{\alpha_N} \text{, and } A^* = A_a\left(\frac{T}{T_0}\right)^{\alpha_a} \qquad (2.10)$$

The parameters used are $A_d = 41.2\, cm^2V^{-1}s^{-1}$, $\alpha_d = -2.34$, $A_N = 1.97 \times 10^{19} cm^{-3}$, $\alpha_N = 0.869$, $A_a = 0.309$, $and\ \alpha_a = -2.311$.

The high field hole mobility model (Figure 2.1 b) used in the drift diffusion simulator is described by the following expression [36].

$$\mu_h(\varepsilon) = \frac{\mu_{h0}}{\left[1+\left(\frac{\mu_{h0}\varepsilon}{\vartheta_{h,sat}}\right)^{\beta}\right]^{\frac{1}{\beta}}} \qquad (2.11)$$

The parameter μ_{h0} is the low field mobility as expressed in equation (2.9), $\beta = 0.725$ and $\vartheta_{h,sat} = 1.7 \times 10^7 cm/s$.

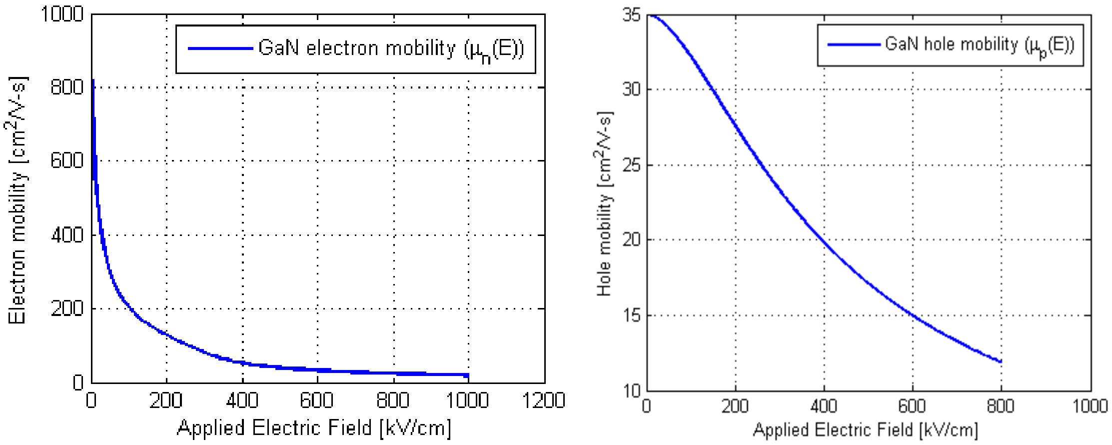

(a) **(b)**

Figure 2.1 Field dependent a) electron mobility and b) hole mobility for GaN.

2.2.2.2 Field dependent diffusion coefficient

The Monte Carlo simulation data for the electron diffusion coefficient in GaN presented in [38] is incorporated in the drift diffusion model using the following expression.

$$D_n(\varepsilon) = p_1\varepsilon^4 + p_2\varepsilon^3 + p_3\varepsilon^2 + p_4\varepsilon + p_5 , \qquad \varepsilon < 200\frac{kV}{cm} \tag{2.12}$$

$$D_n(\varepsilon) = p_6\varepsilon^5 + p_7\varepsilon^4 + p_8\varepsilon^3 + p_9\varepsilon^2 + p_{10}\varepsilon p_{11} ,$$

$$200\frac{kV}{cm} < \varepsilon < 500\frac{kV}{cm}$$

$$D_n(\varepsilon) = 5\ cm^2V^{-1}s^{-1}, \quad \varepsilon > 500\frac{kV}{cm}$$

where the fitting parameters $p_1 = 3.841 \times 10^{-8}$, $p_2 = -2.816 \times 10^{-5}$, $p_3 = 6.859 \times 10^{-3}$, $p_4 = -6.197 \times 10^{-1}$, $p_5 = 22.8$, $p_6 = -9.482 \times 10^{-10}$, $p_7 = 5.473 \times 10^{-7}$, $p_8 = -1.244 \times 10^{-4}$, $p_9 = 1.439 \times 10^{-2}$, $p_{10} = -0.833$ and $p_{11} = 23.88$. The available experimental data and the fitted expression for GaN diffusion coefficient is shown in Figure 2.2.

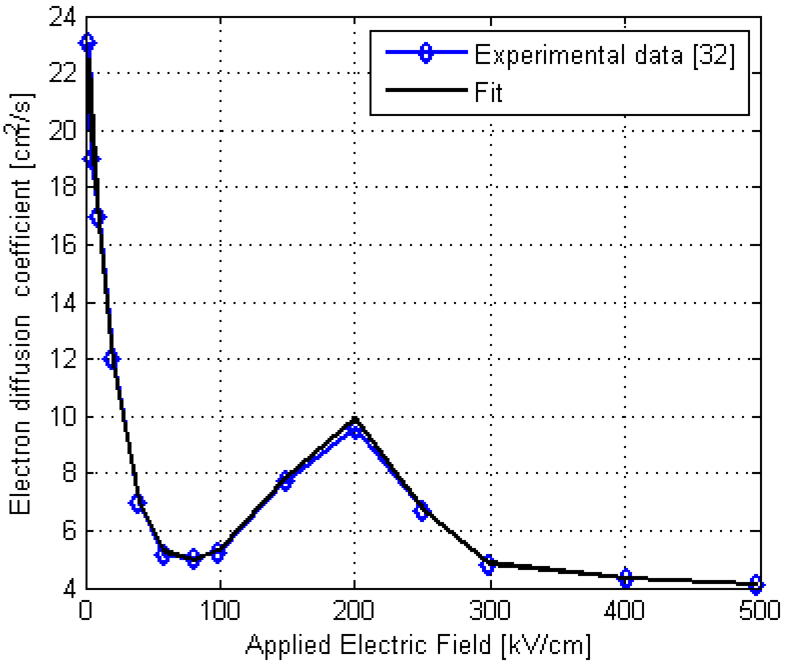

Figure 2.2 Electron Diffusion Coefficient of GaN vs. applied field.

2.2.3 Recombination models

The photon emission or absorption in GaN-based LEDs is governed by the recombination and the generation parameters that play a vital role in determining the device performance and its emission characteristics. The major quantities that are to be considered in this model are the recombination and the generation rates i.e. the rates at which the carrier density decreases or increases due to electron-hole pair recombinations or generations inside the device, respectively. The recombination mechanisms inside a GaN LED consist of both radiative and non-radiative recombinations (Figure 2.3). The radiative recombinations or band to band recombinations are the major parameters responsible for light emission. The non radiative recombinations in a GaN LED are due to both Shockley Read Hall (SRH) recombination or Auger recombination [44], [45].

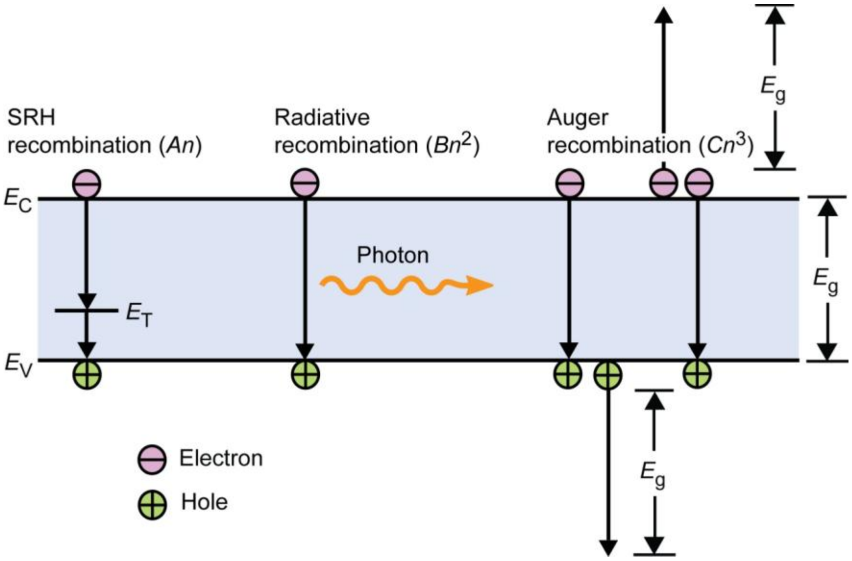

Figure 2.3 Recombination processes in a GaN-based LED (Adapted from [44]).

2.3.1.1 Radiative or Band to Band recombination

The direct bandgap nature of III-Nitride semiconductors is the important parameter that differentiates GaN LEDs with the LEDs made of indirect bandgap materials such as Silicon or SiC. Since in a direct bandgap material, the electron or hole transitions from conduction band to valence band or vice versa occur at same momentum, the recombinations are more effective than that of indirect bandgap material. For the radiative recombinations, the electrons and holes should be at the same position (momentum) in the band diagram. Thus, the radiative recombination in the GaN layers is directly proportional to the electron or hole concentration since it is related to the probability of finding electrons or holes.

$$R_{radiative} = B(np - n_i^2) \tag{2.13}$$

where B is the radiative recombination coefficient and $B \sim 10^{-11}\ to\ 10^{-8}\ cm^3/s$ for III-V semiconductors [23], [46].

2.3.1.2 Non-radiative Shockley Read Hall (SRH) recombination

The non radiative SRH recombinations in GaN are observed due to the dislocations or defects in the material that produces deep levels in the conduction and valence band. Thus, the energy from the electron-hole pair recombinations through deep levels result in the vibration of atoms called phonons instead of photons. If the deep levels are assumed to be at the intrinsic levels, the SRH recombination rate can be expressed as

$$R_{SRH} = \frac{np - n_i^2}{\tau_p^{SRH}(n + n_i) + \tau_n^{SRH}(p + n_i)} \tag{2.14}$$

where τ_p^{SRH} and τ_n^{SRH} are hole and electron SRH lifetimes.

The defects or dislocations in III-nitride materials are important terms that decide the SRH lifetimes. With more defects or dislocations, these lifetimes tend to decrease and thereby the non radiative recombinations occur at a faster rate and this is the reason for high non-radiative SRH recombinations are directly related to the defects. These lifetimes are also reduced at low carrier mobilities or diffusion coefficients.

Thus, the SRH lifetimes τ_p^{SRH} or τ_n^{SRH} can be expressed as a function of the dislocation densities and mobilities as [47]

$$\tau_{n(p)}^{SRH} = \frac{1}{4\pi D_{n(p)}\, N_d}\left[\ln\left(\frac{1}{\pi a^2 N_d}\right) - \frac{3}{2} + \frac{\left(2D_{n(p)}\right)}{aV_{n(p)}S}\right] \tag{2.15}$$

where $D_{n(p)}$ is the diffusion coefficient, N_d is the thread dislocation density (TDD),

$V_{n(p)} = \left(\frac{3kT}{m_{n(p)}^{av}}\right)^{\frac{1}{2}}$ is the thermal velocity and $S = 0.5$ for GaN (constant).

Figure 2.4 shows the dependence of the SRH lifetimes on the TDD. These are also compared with the radiative lifetime obtained from radiative recombination coefficient B. It can be observed that the non radiative lifetimes become smaller than radiative lifetimes for dislocation densities higher than $10^7\ cm^{-2}$. Therefore, the non radiative recombinations start to affect the internal quantum efficiencies from these TDDs onwards.

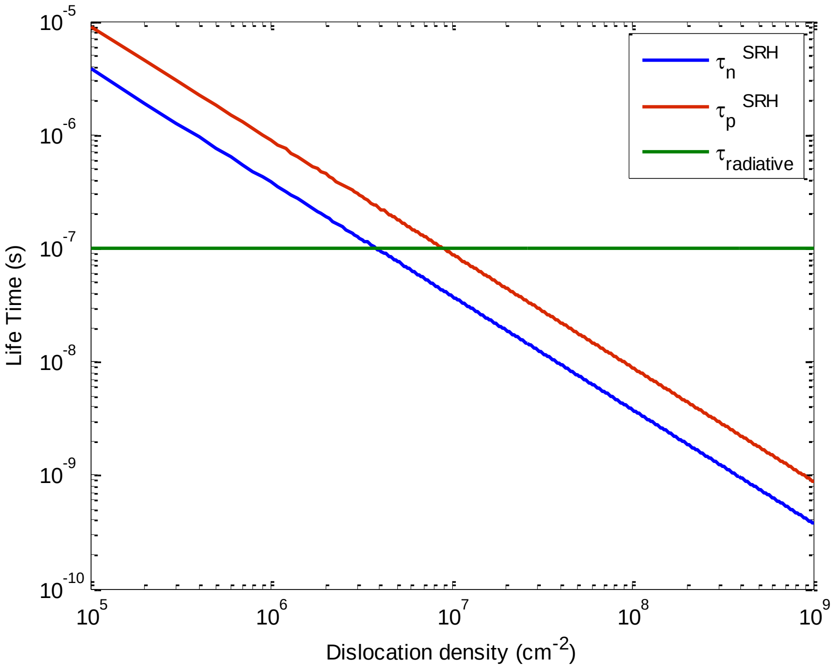

Figure 2.4 Dislocation density vs. non-radiative lifetimes (τ_p^{SRH} and τ_n^{SRH}) in III- Nitride materials.

2.3.1.3 Non-radiative Auger recombination

Auger recombination in GaN LEDs occurs at high injection levels where the electron and hole interactions result in generation of another hot carrier. Thus, there are two basic processes: a) electron-electron-hole (eeh) process where an electron-hole pair (EHP) recombination excites an electron to a higher level in the conduction band as shown in Figure 2.3, b) electron-hole-hole process in which an EHP recombination excites a hole to a lower level in the valence band. It was explained in various studies that the Auger recombination is the dominant mechanism for the decrease in the external quantum efficiencies of GaN LEDs at high current densities or efficiency droop [23], [44], [48] [49]. The auger recombination rate is given by the following equation.

$$R_{Auger} = \mathit{\Gamma}_n n(np - n_i^2) + \mathit{\Gamma}_p p(np - n_i^2) \qquad (2.16)$$

where $\mathit{\Gamma}_n$ and $\mathit{\Gamma}_p$ are electron and hole Auger recombination coefficients in $cm^{-6}s^{-1}$.

The radiative and non radiative recombination rates in equations (2.14)-(2.16) are in general simplified as ABC model (A- SRH recombination, B- Radiative recombination and C- Auger recombination) i.e. at high injection levels when n=p, these equations are simplified as

$$R_{SRH} = An, R_{radiative} = Bn^2 \text{ } and \text{ } R_{Auger} = Cn^3 \qquad (2.17)$$

where $A = \frac{1}{2\tau^{SRH}}$, $B = \frac{1}{\tau_{radiative}\,\Delta n}$ and $C = \mathit{\Gamma}$

The radiative or non radiative carrier lifetimes or the recombination coefficients A, B or C are important parameters that determine the IQE of GaN LEDs and help to understand recombination processes and to optimize LED structures. These lifetimes have been determined through the time-resolved photoluminescence (TRPL) measurements in several studies [48], [50]. A rate equation model has been proposed very recently to extract the recombination coefficients and IQE by using a transient analysis of GaN-based LEDs through numerical simulations [51]. Through such studies, researchers were able to increase the radiative recombinations inside a GaN LED. Therefore, it is important to use appropriate models and coefficients for recombination mechanisms in simulating GaN- based LED structures.

2.2.4 Polarization model for LED heterostructures

Another important material parameter of III-Nitride materials that is needed to be incorporated in the DD simulator is the built- in spontaneous and piezoelectric polarization charges. The spontaneous polarization is usually observed in ferroelectrics and pyroelectrics. In pyroelectrics such as III-Nitride semiconductors that have a hexagonal or wurtzite crystal structure, the center of electronic charges do not coincide with the nucleus position due to uneven bonding among the atoms leading to built- in electric field causing spontaneous polarization [39]. The piezoelectric polarization occurs at the hetero interfaces such as GaN/ AlGaN or GaN/ InGaN due to thermal strain, mechanical stress or lattice mismatch [40]. These polarizations play a vital role in the performance of III-Nitride optoelectronic devices based on MQWs nanostructures. The following are some effects of these polarizations in GaN devices.

1. The photoluminescence emission energies of GaN/ AlGaN heterostructures and QWs are strongly affected due to the presence of built-in polarization charges at the heterointerface. These energies vary with the well composition [41] .

2. Reduction in IQE of III-Nitride LEDs.

3. The effect on luminescence spectra of GaN/ AlGaN QWs [26] . This occurs due to red shift of the energy gap caused due to polarization charges at heterointerface and also with varying widths of QWs.

4. Reduction in the gate leakage current in the nitride heterostructure field effect transistors [42]. This effect is due to the increase in the polarization charges at heterointerface with incorporation of Indium in the active layers.

In order to incorporate the above polarizations in the simulator, the fixed interface charges at the GaN/ AlGaN heterostructures are included in the Poisson equation. These charges are computed from the difference of total polarizations at hetero interfaces

The surface charge density at AlGaN/GaN heterointerface is calculated as:

$$N_s = (P_{AlGaN}^{tot} - P_{GaN}^{tot})/\, q \tag{2.18}$$

where P_{AlGaN}^{tot} or P_{GaN}^{tot} is the sum of built-in spontaneous and piezoelectric polarizations. These fixed surface charges are therefore incorporated in Poisson's equation to model the polarization effects as shown in the following equation.

$$\nabla.(\varepsilon \nabla V) = -q(N_D^+ - N_A^- + p - n \mp N_s) \tag{2.19}$$

2.3 Dispersive material models

The propagation of light wave inside GaN LED structures described by the solution of Maxwell's equations (equations (1.8)-(1.12)) is affected by the frequency dependent parameters of the material. Therefore, to account such effects, i.e. material dispersion, appropriate models have to be used to simulate optical characteristics.

The frequency dependent optical behavior of dispersive materials can be described by the constitutive relations in frequency domain, i.e. the relation between the electric field intensity E, the electric flux density D and the polarization density P given by the following equations

$$D(\omega) = \varepsilon(\omega)E(\omega) \tag{2.20}$$

$$P(\omega) = \varepsilon_o\chi(\omega)E(\omega) \tag{2.21}$$

$$D(\omega) = \varepsilon_o E(\omega) + P(\omega) \tag{2.22}$$

where χ is the electric susceptibility that is a measure of the ability of a dielectric to polarize in the presence of an external electric field and $P(\omega)$ is the frequency dependent polarization induced by an external electric field $E(\omega)$.

Therefore, combining equations (2.20)-(2.22), we have

$$D(\omega) = \varepsilon_o E(\omega)\big(1 + \chi(\omega)\big) \tag{2.23}$$

$$\varepsilon(\omega) = \varepsilon_o\big(1 + \chi(\omega)\big)\ or\ \varepsilon_r(\omega) = \big(1 + \chi(\omega)\big) \tag{2.24}$$

where, $\varepsilon_r(\omega)$ is the frequency dependent relative permittivity of the dispersive material.

The material models describing the frequency dependent behavior of relative permittivity or electromagnetic polarization can be derived using the classical electron oscillator (CEO) model. These models deal with macroscopic polarization properties of dispersive material.

The relation between frequency dependent electromagnetic polarization $P(\omega)$ and electric field intensity $E(\omega)$ of dispersive materials used in this thesis is modeled using Drude and Lorentz models [52], [53].

2.3.1 Drude Model

The Drude model describes the transport properties of electrons in a metal. It is based on the CEO model and assumes that the electrons travel inside a metal without interacting with each other in the presence of external electric field i.e. free electrons. The motion is dampened by electron collisions with the ions. The relation between macroscopic polarization and electric field can be described by using Newton's laws of motion as

$$P(\omega) = \frac{nq^2}{m(j\Gamma\omega - \omega^2)} E(\omega) \tag{2.25}$$

where n is the electron density, q is the magnitude of electronic charge, m is the mass of electron and Γ is damping constant.

The electric susceptibility $\chi(\omega)$ can be found using equation (2.21) as

$$\chi(\omega) = \frac{P(\omega)}{\varepsilon_o E(\omega)} = \frac{nq^2}{m(j\Gamma\omega - \omega^2)} \tag{2.26}$$

Thus, the relative permittivity can be found using equation (2.24) as

$$\varepsilon_r(\omega) = 1 + \frac{nq^2}{m(j\Gamma\omega - \omega^2)} = 1 + \frac{\omega^2{}_p}{j\Gamma\omega - \omega^2} \tag{2.27}$$

ω_p is the plasma frequency of the metal that describes the rapid oscillations of the electron density in conducting materials.

2.3.2 Lorentz Model

The Lorentz model describes the electron transport properties using the CEO model for any conducting material i.e. metal or non-metal. It is analogous to the spring-mass system. The behavior of electrons in the presence of an external electric field is such that they oscillate like a mass bounded to a spring i.e. electrons are bounded to the atoms. The relation between electric field and polarization is expressed as

$$P(\omega) = \frac{ne^2}{m(\omega_o^2 + j\Gamma\omega - \omega^2)} E(\omega) \tag{2.28}$$

Where ω_o is the resonance frequency of electron density oscillations.

And the electric susceptibility $\chi(\omega)$ and $\varepsilon_r(\omega)$ are given as

$$\chi(\omega) = \frac{P(\omega)}{\varepsilon_o E(\omega)} = \frac{ne^2}{m(\omega_o^2 + j\Gamma\omega - \omega^2)} \tag{2.29}$$

$$\varepsilon_r(\omega) = 1 + \frac{ne^2}{m(\omega_o^2 + j\Gamma\omega - \omega^2)} = 1 + \frac{{\omega^2}_p}{(\omega_o^2 + j\Gamma\omega - \omega^2)} \tag{2.30}$$

In this thesis, the frequency dependent relative permittivity of GaN and AlGaN materials is modeled using the multi pole Lorentzian function given in equation (2.30) because it is applicable to any conducting material.

2.3.3 Lorentz-Drude Model

A more generalized model describing the complex permittivity of metals is described using a Lorentz-Drude model which characterizes the free electrons using the Drude model and bound electrons using the Lorentz model. Therefore, the permittivity of the Lorentz-Drude model is given as

$$\varepsilon(\omega) = \varepsilon_{free}(\omega) + \varepsilon_{bound}(\omega) \tag{2.31}$$

where, $\varepsilon_{free}(\omega)$ is described by Drude model and $\varepsilon_{bound}(\omega)$ by Lorentz model. Therefore, we have

$$\varepsilon\,(\omega) = \varepsilon_o\left(1 + \frac{\omega_p^2}{j\Gamma\omega - \omega^2} + \frac{\omega^2{}_p}{(\omega_o^2 + j\Gamma\omega - \omega^2)}\right) \tag{2.32}$$

The relative permittivity of metals used in this thesis i.e. Silver and Gold are therefore modeled using a multi-pole Lorentz-Drude model.

2.4 Summary

Carrier transport models and dispersive material models required for the simulation of GaN LEDs are presented in this chapter. Carrier transport model consists of coupled Poisson's equations, carrier continuity equations and drift diffusion current equations. The field dependent carrier transport parameters that are incorporated in the electronic transport model are also discussed. Lorentz model, Drude model and Lorentz-Drude model are presented to model the dispersive properties of any conducting material.

CHAPTER 3

FINITE DIFFERENCE TIME DOMAIN SIMULATION ALGORITHM

The time domain simulation of GaN LEDs is performed using Finite difference time domain (FDTD) numerical method which is a popular technique that has been widely used in computational electromagnetics problems. In this chapter, the FDTD algorithm for electronic-optical simulation of GaN LEDs is developed to simulate the carrier transport and photon emission. The resulting FDTD algorithm is used to model the active part of the device by solving the drift diffusion (DD) transport equations and the electromagnetic part by solving Maxwell's equations in time domain. This chapter also discusses the boundary conditions required for FDTD solution of DD and Maxwell's equations.

3.1 Overview of the FDTD Method

The finite difference time domain (FDTD) numerical technique is a very popular and well established numerical technique to solve the coupled partial differential equations in time domain. It was first introduced by Kane Yee in 1966 as a numerical algorithm to solve Maxwell's equations [54]. It uses finite difference approximations to the spatial and temporal derivatives. It improved exponentially with several advanced models and has become an efficient computational tool to model several electromagnetic problems. The research and developments on this technique have led to more stable numerical techniques to solve EM problems that can be used for a wide range of applications; few of them are listed below [55]:

1. Military defense applications: Radar technologies, development of high power microwave sources (HPM), circuits and antennas.
2. Numerical modeling of electronic, photonic and nanoplasmonic devices and components.
3. Bio electromagnetic simulations.
4. High speed communications.

The advantages and disadvantages of the FDTD method are:

A) Advantages

1. It is simple, robust and can be implemented efficiently.
2. It is a well-developed tool for the analysis of photonic devices in the industry.
3. It can be used for broad range of EM problems covering the ultra-low to ultra violet frequencies.
4. It can simulate the multi wavelength simulation in one run.
5. It has well developed absorbing boundary conditions for EM fields.

B) Disadvantages

1. The computational burden increases with finer mesh sizes.
2. The space and time steps are limited by Courant- Friedrich- Levy (CFL) stability criterion [55].
3. The curved boundaries are poorly represented.

4. The time response of the medium should be modeled explicitly.

3.2 Electronic Model FDTD DD Algorithm

The solutions of the basic DD equations (equations (2.1)-(2.6)) have been obtained in closed form for any semiconductor device. However, these types of solutions are limited in applications and accuracy for nonlinear or multi-dimensional problems. Therefore, numerical techniques can be used to investigate such problems. The finite difference numerical technique is used to solve these set of coupled nonlinear partial differential equations. FDTD solution of DD model produces the solutions for the electrostatic potential and the electron and hole densities (V, n and p). The partial derivatives are discretized by finite difference approximations.

3.2.1 FDTD solution of drift diffusion equations

The finite difference approximation of first order and second order derivatives are given as,

$$\frac{\partial}{\partial x} f(i,j) \approx \frac{f(i+1,j) - f(i,j)}{\Delta x} \tag{3.1}$$

$$\frac{\partial^2}{\partial x^2} f(i,j) \approx \frac{f(i-1,j) - 2f(i,j) + f(i+1,j)}{\Delta x^2} \tag{3.2}$$

The 2D FDTD grid arrangement is shown in Figure 3.1. With such arrangement, the finite difference approximations can be used without any inconsistency. The scalar variables such as the potential V or the electron and hole concentrations n and p, are defined at integer grid points (i,j), whereas the vector quantities current densities and electric fields are defined at grid points $\left(i+\frac{1}{2},j\right)$ for x components and $\left(i,j+\frac{1}{2}\right)$ for y components. In addition to this, the vector quantities are offset in time by half time step for the temporal derivatives to be consistent i.e. the scalar quantities are calculated at time step k, vector quantities are calculated at time step $k + 1/2$.

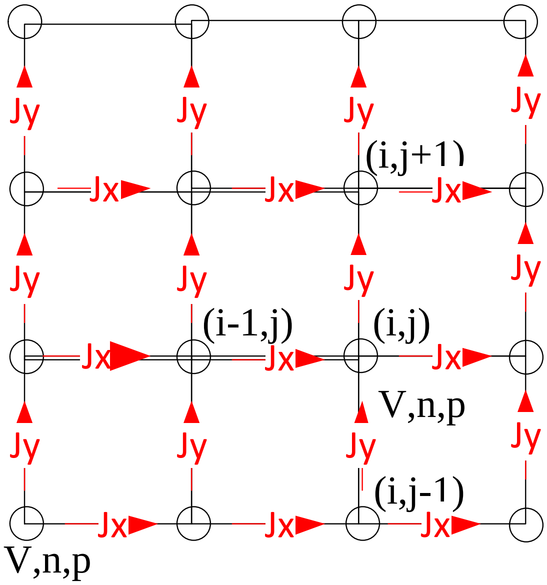

Figure 3.1 2D FDTD grid arrangement to solve DD equations.

For a homogeneous medium, Poisson's equation is given as

$$\frac{\partial^2 V}{\partial x^2} + \frac{\partial^2 V}{\partial y^2} = -\frac{\rho}{\varepsilon} \tag{3.3}$$

The finite difference discretization of equation (3.3) at time t= $k\Delta t$ is obtained as

$$\frac{V^k\,(i+1,j) + V^k\,\,(i-1,j) - 2V^k(i,j)}{\Delta x^2} + \frac{V^k(i,j+1) + V^k(i,j-1) - 2V^k(i,j)}{\Delta y^2} = -\frac{\rho^k(i,j)}{\varepsilon} \tag{3.4}$$

Equation (3.4) can be rewritten (for $\Delta x = \Delta y$) to solve for the electrostatic potential $V(i,j)$ for a homogeneous medium, as

$$V^{k}\,(i,j)=\frac{1}{4}\Bigg[V^{k}\,(i+1,j)+V^{k}(i-1,j)+V^{k}\,(i,j+1)+V^{k}\,(i,j-1)+\left(\frac{\Delta x^{2}}{\varepsilon}\right)\rho^{k}\,(i,j)\Bigg] \tag{3.5}$$

It can be observed from equation (3.5) that the potential at grid point (i,j) depends on potential at four neighboring grid points. This requires solving potential at these grid points simultaneously i.e. systematic algorithms are required to solve Poisson's equation. There are both direct and iterative methods to solve the discretized Poisson's equation (Equation (3.5)). The direct methods such as Gauss elimination method and LU decomposition method are based on triangularization techniques that eliminate the unknowns in a systematic way [56]. The iterative methods include the mesh relaxation methods and the matrix methods such as the Jacobi, Gauss-Siedel, Successive over-relaxation (SOR), Alternating directions implicit (ADI), Sparse matrix, and Conjugate gradient methods. The iterative methods start with a first approximation which is improved successively by repeating the algorithm until an accurate solution is achieved. The SOR iterative method converges faster as compared to other iterative methods [56], [57]. The direct methods require a lot of computational effort with increase in the size of the simulation domain since they require solving a system of linear equations and matrix inversions at each time step. Thus to overcome this difficulty, a simple and explicit iterative method such as SOR can be used to obtain solution of Poisson's equation.

Thus, a Poisson equation solver based on SOR technique is developed to solve for electrostatic potential V. In this method, first, the residue is calculated at each grid point and iteration given by equation (3.6)

$$R\ (i,j) = \frac{1}{4}\left[V\ (i+1,j) + V\ (i-1,j) + V\ (i,j+1) + V\ (i,j-1) - 4V(i,j) + \left(\frac{\Delta x^2}{\varepsilon}\right)\rho\ (i,j)\right] \tag{3.6}$$

Next, we add a correction factor to potential $V\ (i,j)$ at each iteration given by equation (3.7).

$$V^m(i,j) = V^{m-1}(i,j) + R^{m-1}(i,j) \tag{3.7}$$

The SOR method uses a convergence factor ω to increase the convergence of the iterations in the equation (3.7) as

$$V^m(i,j) = V^{m-1}(i,j) + \omega R^{m-1}(i,j) \tag{3.8}$$

ω is given as

$$\omega = 2\left[\cos\left(\frac{\pi}{i_e}\right) + \cos\left(\frac{\pi}{j_e}\right)\right]\ , and\ 0 < \omega < 2 \tag{3.9}$$

where i_e and j_e are the number of grid points in x and y directions, respectively.

For non-homogeneous medium, the Poisson solver equations (equations (3.3)-(3.9)) are given as

$$\frac{\partial}{\partial x}\left(\varepsilon\frac{\partial V}{\partial x}\right) + \frac{\partial}{\partial y}\left(\varepsilon\frac{\partial V}{\partial y}\right) = -\rho \tag{3.10}$$

$$a(i,j)V^k(i+1,j) + b(i,j)V^k(i-1,j) + c(i,j)V^k(i,j+1) + d(i,j)V^k(i,j-1) + e(i,j)V(i,j) = f(i,j) \tag{3.11}$$

$$R\ (i,j) = \frac{\left[\begin{matrix} a(i,j)V\ (i+1,j) + b(i,j)V\ (i-1,j) + c(i,j)V\ (i,j+1) + d(i,j)V\ (i,j-1) \\ +e(i,j)V(i,j) - f(i,j)\end{matrix}\right]}{e(i,j)} \tag{3.12}$$

and,

$$V^m(i,j) = V^{m-1}(i,j) - \omega R^{m-1}(i,j) \tag{3.13}$$

The coefficients a, b, c, d, e and f are given by the following expressions

$$\begin{gathered} a(i,j) = \epsilon(i,j), \\ b(i,j) = \epsilon(i-1,j), \\ c(i,j) = r\epsilon(i,j), \\ d(i,j) = r\epsilon(i,j-1)\ , \\ e(i,j) = (-1-r)\epsilon(i,j) - \epsilon(i-1,j) - r\epsilon(i,j-1)\ , \\ f(i,j) = q\Delta x^2(n - N_D^+ - p + N_A^-) \\ r = \frac{\Delta x^2}{\Delta y^2} \end{gathered} \tag{3.14}$$

The problem with SOR is that the convergence is affected for regions with multiple dielectrics. It converges slowly with the increase in the dielectric constant. The convergence rate decreases linearly with the maximum dielectric constant in the simulated domain. In such situations, when the solution does not converge to accurate solution, advanced numerical techniques should be introduced to solve Poisson's equation. Thus the update equation to solve for electrostatic potential in time domain using FDTD technique is given by equations (3.8)-(3.13).

The update equation for the static electric field is obtained using equation (2.2) as

$$E_x^{k+\frac{1}{2}}(i,j) = -\left(\frac{V^k(i+1,j) - V^k(i,j)}{\Delta x}\right) \tag{3.15}$$

$$E_y^{k+\frac{1}{2}}(i,j) = -\left(\frac{V^k(i,j+1) - V^k(i,j)}{\Delta y}\right) \tag{3.16}$$

Similarly, the finite difference approximations of current density equations (equations (2.5)-(2.6) for a 2D simulation domain are given as

$$J_{n,x}^{k+\frac{1}{2}}\left(i+\frac{1}{2},j\right) = -q\left\{\frac{\mu_n(i+1,j)+\mu_n(i,j)}{2}\right\}\left\{\frac{n^k(i+1,j)+n^k(i,j)}{2}\right\}\left\{\frac{V^k(i+1,j)-V^k(i,j)}{\Delta x}\right\} + q\left\{\frac{D_n(i+1,j)+D_n(i,j)}{2}\right\}\left\{\frac{n^k(i+1,j)-n^k(i,j)}{\Delta x}\right\} \tag{3.17}$$

$$J_{n,y}^{k+\frac{1}{2}}\left(i,j+\frac{1}{2}\right) = -q\left\{\frac{\mu_n(i,j+1)+\mu_n(i,j)}{2}\right\}\left\{\frac{n^k(i,j+1)+n^k(i,j)}{2}\right\}\left\{\frac{V^k(i,j+1)-V^k(i,j)}{\Delta y}\right\} + q\left\{\frac{D_n(i,j+1)+D_n(i,j)}{2}\right\}\left\{\frac{n^k(i,j+1)-n^k(i,j)}{\Delta y}\right\} \tag{3.18}$$

$$J_{p,x}^{k+\frac{1}{2}}\left(i+\frac{1}{2},j\right) = -q\left\{\frac{\mu_p(i+1,j)+\mu_p(i,j)}{2}\right\}\left\{\frac{p^k(i+1,j)+p^k(i,j)}{2}\right\}\left\{\frac{V^k(i+1,j)-V^k(i,j)}{\Delta x}\right\} - q\left\{\frac{D_p(i+1,j)+D_p(i,j)}{2}\right\}\left\{\frac{p^k(i+1,j)-p^k(i,j)}{\Delta x}\right\} \tag{3.19}$$

$$J_{p,y}^{k+\frac{1}{2}}\left(i,j+\frac{1}{2}\right) = -q\left\{\frac{\mu_p(i,j+1)+\mu_p(i,j)}{2}\right\}\left\{\frac{p^k(i,j+1)+p^k(i,j)}{2}\right\}\left\{\frac{V^k(i,j+1)-V^k(i,j)}{\Delta y}\right\} - q\left\{\frac{D_p(i,j+1)+D_p(i,j)}{2}\right\}\left\{\frac{p^k(i,j+1)-p^k(i,j)}{\Delta y}\right\} \tag{3.20}$$

The scalar terms n, p, μ_n, μ_p, D_n and D_p are averaged for consistency.

The electron and hole continuity equations (equation (2.3)-(2.4)) are discretized both in space and time as

$$n^{k+1}(i,j) = n^k(i,j) + \frac{\Delta t}{q}\left\{\frac{J_{n,x}^{k+\frac{1}{2}}\left(i+\frac{1}{2},j\right) - J_{n,x}^{k+\frac{1}{2}}\left(i-\frac{1}{2},j\right)}{\Delta x} + \frac{J_{n,y}^{k+\frac{1}{2}}\left(i,j+\frac{1}{2}\right) - J_{n,y}^{k+\frac{1}{2}}\left(i,j-\frac{1}{2}\right)}{\Delta y}\right\} + \Delta t\left(G_n^k(i,j) - R_n^k(i,j)\right) \tag{3.21}$$

$$p^{k+1}(i,j) = p^k(i,j) - \frac{\Delta t}{q}\left\{\frac{J_{p,x}^{k+\frac{1}{2}}\left(i+\frac{1}{2},j\right) - J_{p,x}^{k+\frac{1}{2}}\left(i-\frac{1}{2},j\right)}{\Delta x} + \frac{J_{p,y}^{k+\frac{1}{2}}\left(i,j+\frac{1}{2}\right) - J_{p,y}^{k+\frac{1}{2}}\left(i,j-\frac{1}{2}\right)}{\Delta y}\right\} + \Delta t\ \left(G_p^k(i,j) - R_p^k(i,j)\right) \tag{3.22}$$

Therefore, at each time step, the new values of $\boldsymbol{J}$ are calculated using the previous values of V, n and p and are stored for next time step. Similarly, the new values of n and p are calculated using the previous values of n, p, R and G and the new values of $\boldsymbol{J}$. Thus, the update equations (3.13)-(3.22) develop the basic FDTD algorithm for studying electronic carrier transport in any semiconductor device. These basic semiconductor equations are solved with suitable boundary conditions i.e. Dirchilet and Neumann boundary conditions [15] for electrostatic potential and carrier densities that are discussed in detail in section 3.2.1.

3.2.2 Calculation of Spontaneous and Piezoelectric Polarization Charges

The built-in polarization charges ($\nabla . \boldsymbol{P^{tot}}$) incorporated in Poisson's equation (equation (3.23)) are calculated from the spontaneous and piezoelectric polarizations of the materials used in the simulation.

$$\nabla.(\varepsilon\nabla V) = -q(N_D^+ - N_A^- + p - n) + \nabla.\boldsymbol{P^{tot}} = -\rho + \nabla.\boldsymbol{P^{tot}} \tag{3.23}$$

Considering the material growth in y-direction i.e. the heterointerface is in y direction, the interface charges are given by the term $\nabla.P^{tot}$ that can be discretized using finite difference approximation as:

$$\nabla.\boldsymbol{P^{tot}} = \frac{P^{tot}(i,j+1) - P^{tot}(i,j)}{\Delta y} = \frac{qN_s(i,j)}{\Delta y} \tag{3.24}$$

Therefore, the coefficient $f(i,j)$ (equation (3.14)) of the discretized Poisson equation for heterojunction case now becomes,

$$f(i,j) = q\Delta x^2(n - N_D^+ - p + N_A^-) + q\Delta x^2\frac{P^{tot}(i,j) - P^{tot}(i,j-1)}{\Delta y} \tag{3.25}$$

The total polarization is the sum of both spontaneous and piezoelectric polarizations. The values of these polarizations for AlGaN/ GaN and InGaN/ GaN heterointerface are calculated using the following equations (equations (3.26)-(3.30)) [39]. The parameters used in the calculation of these charges are given in Table 3.1.

Table 3.1 Spontaneous polarization values of III- Nitride materials [39], [40]

Material Parameters	GaN	AlN	InN
$P^{sp}\ \left(\frac{c}{m^2}\right)$	-0.034	-0.090	-0.0413
$a_0(A)$	3.189	3.112	3.540

AlGaN/ GaN heterointerface

$$P^{tot}\ (Al_xGa_{1-x}N) = \ P^{sp}\ (Al_xGa_{1-x}N) + P^{pz}\ (Al_xGa_{1-x}N) \tag{3.26}$$

$$P^{sp}\ (Al_xGa_{1-x}N) = \ -0.090x - 0.034(1-x) + 0.019x(1-x) \tag{3.27}$$

$$P^{pz}\ (Al_xGa_{1-x}N) = \ xP^{pz}\ (AlN)\varepsilon + (1-x)P^{pz}\ (GaN) \tag{3.28}$$

$$P^{pz}\ (GaN) = \ -0.918\varepsilon + 9.541\varepsilon^2 C/m^2 \tag{3.29}$$

$$P^{pz}\ (AlN) = \ -1.808\varepsilon - 7.888\varepsilon^2 C/m^2 \tag{3.30}$$

Where ε is the strain component obtained from the equilibrium lattice constant of GaN and AlGaN given as

$$\varepsilon = \frac{a^{GaN} - a(x)}{a(x\,)},\ a(x) = x(a^{AlN}) + (1-x)(a^{GaN}) \tag{3.31}$$

Therefore, the sheet charge density N_s at AlGaN/ GaN heterointerface calculated using equation (2.18) is shown in Figure 3.2 as a function of Al mole fraction.

InGaN/ GaN heterointerface

$$P^{tot}\ (In_xGa_{1-x}N) = \ P^{sp}\ (In_xGa_{1-x}N) + P^{pz}\ (In_xGa_{1-x}N) \tag{3.32}$$

$$P^{sp}\ (In_xGa_{1-x}N) = \ -0.042x - 0.034(1-x) + 0.038x(1-x) \tag{3.33}$$

$$P^{sp}\ (In_xGa_{1-x}N) = \ -0.042x - 0.034(1-x) + 0.038x(1-x) \tag{3.34}$$

$$P^{pz}\ (In_xGa_{1-x}N) = \ xP^{pz}\ (InN)\varepsilon + (1-x)P^{pz}\ (GaN) \tag{3.35}$$

$$P^{pz}\ (InN) = \ -1.373\varepsilon + 7.559\varepsilon^2 C/m^2 \tag{3.36}$$

$$P^{pz}\ (GaN) = \ -0.918\varepsilon + 9.541\varepsilon^2 C/m^2 \tag{3.37}$$

The strain component ε is calculated as

$$\varepsilon = \frac{a^{GaN} - a(x)}{a(x\,)},\; a(x) = x(a^{InN}) + (1-x)(a^{GaN}) \tag{3.38}$$

The calculated sheet charge density N_s at InGaN/ GaN heterointerface is shown in Figure 3.3 as a function of In mole fraction.

The values of N_s obtained experimentally are usually smaller than the calculated values using the above model. This is due to the charge screening resulting from dislocations or defects. The screening percentages for an AlGaN/ GaN heterointerface are nearly 90 % whereas for an InGaN/ GaN system is 20- 80%. Therefore, to account for this effect, only 10% of calculated values are taken in simulation model for an AlGaN/ GaN heterojunction.

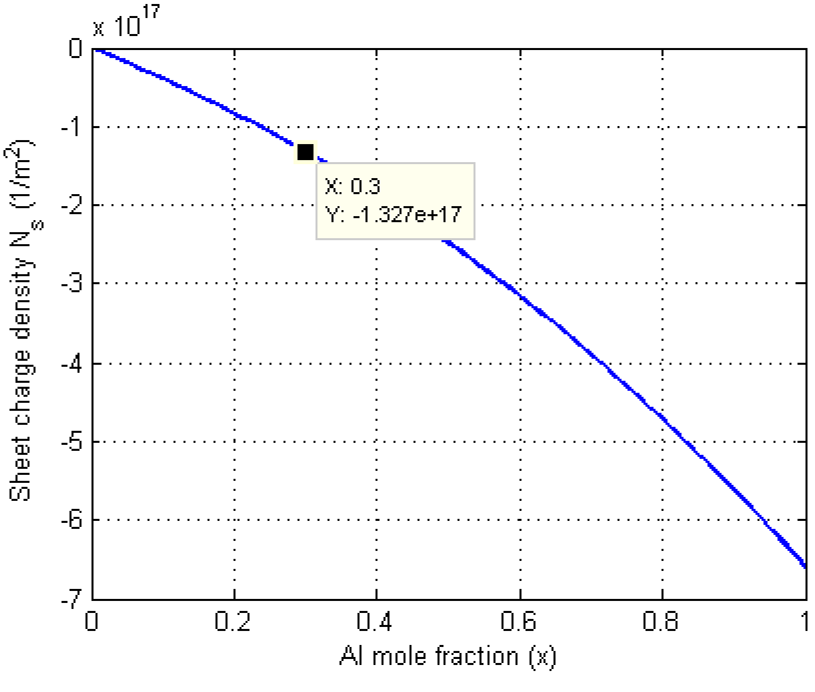

Figure 3.2 Calculated sheet charge density at AlGaN/ GaN heterointerface.

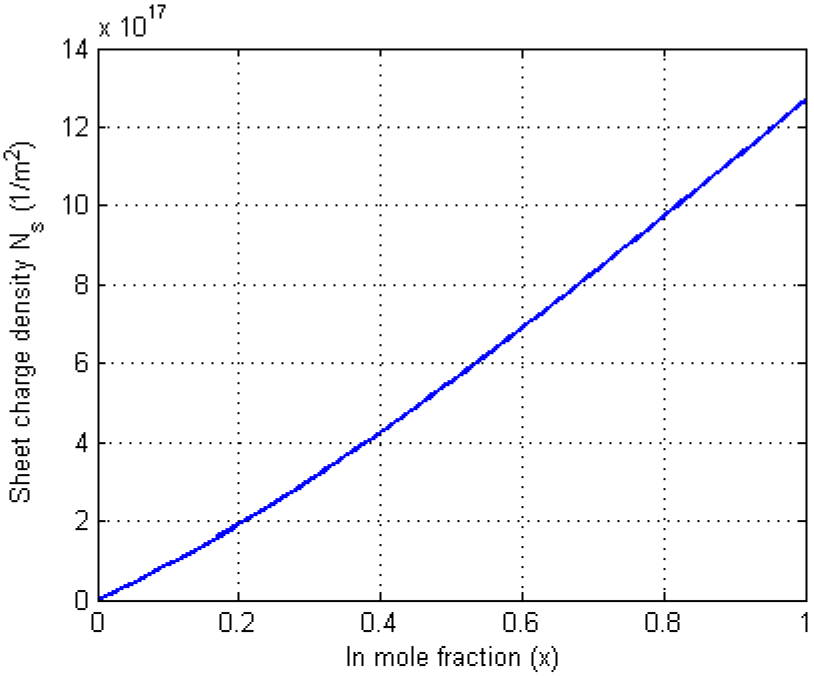

Figure 3.3 Calculated sheet charge density at InGaN/ GaN heterointerface.

3.2.3 Boundary conditions

The metal contacts are considered to be ohmic contacts i.e. the electrostatic potential V and carrier concentrations n and p will have Dirchilet boundary conditions at these contacts. A Dirchilet boundary condition assigns the thermal equilibrium values to the potential and concentrations as shown in Table 3.2. The free surfaces or non-contacts uses the Neumann boundary condition. A Neumann boundary condition is used for continuity of potential and concentrations at these surfaces. Therefore, the gradient of the normal component of potential or concentrations at these surfaces is zero and it is given by Neumann boundary condition as shown in Table 3.2. V_p is the potential at p-contact, V_n is the potential at n-contact, $V_{applied}$ is the applied voltage and V_{bi} is the zero bias built in potential.

Table 3.2 Boundary conditions for electrostatic potential and carrier concentrations.

Parameter	Contacts (Dirchilet BC)	Free Surfaces or Non Contacts (Neumann BC)
Potential V	$V_p = (V_{applied} - V_{bi})$ $V_n = 0$	$\nabla_{\perp}V = 0$
Concentrations n and p	$\mathrm{n} = \mathrm{n}_0 , p = p_0$	$\nabla_{\perp}n = 0 , \nabla_{\perp}p = 0$

.Figure 3.4 shows the flowchart for solving the time domain drift diffusion equations. The flow of calculations in time loop to solve the three basic semiconductor coupled equations i.e. Poisson’s equation, current density equation and the carrier continuity equation ((3.13)-(3.22)) are also shown in this figure.

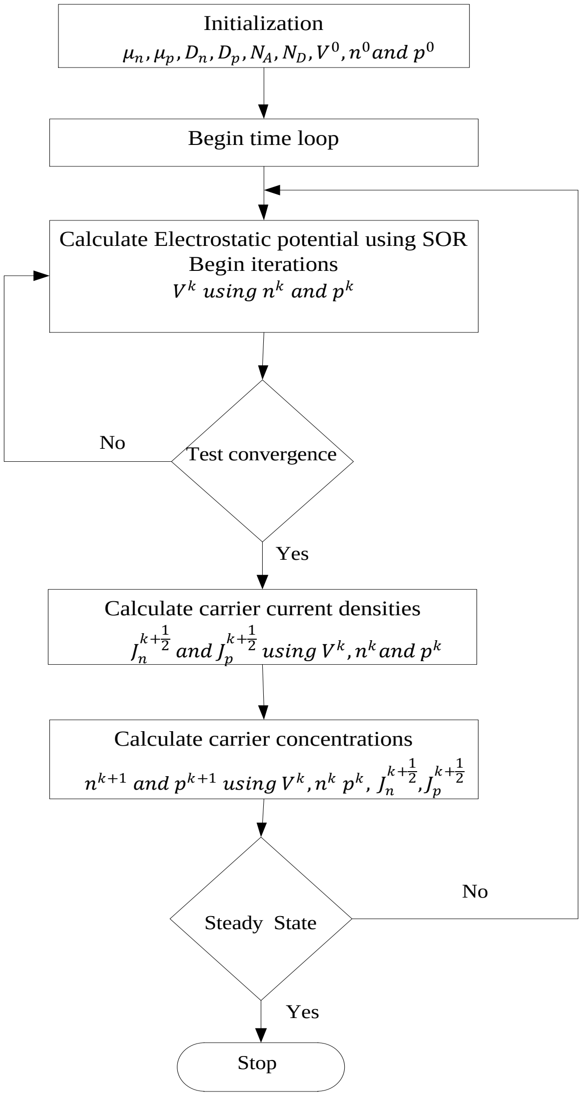

Figure 3.4 Flowchart (Electronic Model).

3.3 Optical Model FDTD Algorithm

The electromagnetic light wave propagation in GaN LEDs is described by the solution of the coupled partial differential equations representing the four Maxwell's equations. Several computational methods have been used to obtain the numerical solution of Maxwell's equations. FDTD method provides direct solution of these equations by discretizing the partial differential equations in space and time. In this work, we use generalized Auxiliary Differential Equation (ADE)- FDTD algorithm that incorporates the optical properties of dispersive materials to solve the electromagnetic part of GaN LEDs [52].

3.3.1 FDTD Solution Method

3.3.1.1 Yee's mesh

The discretization of coupled partial differential Maxwell's equations in space and time is based on Yee's mesh that provides an appropriate arrangement of electric and magnetic fields to provide consistency both in space and time [54].

Yee's mesh positions electric (E) and magnetic field (H) components at the centers of the grid lines and surfaces such that each E field component is surrounded by four H components and vice versa in a 3D grid as shown in Figure 3.5. This type of arrangement also links the fields to Ampere's and Faraday's laws.

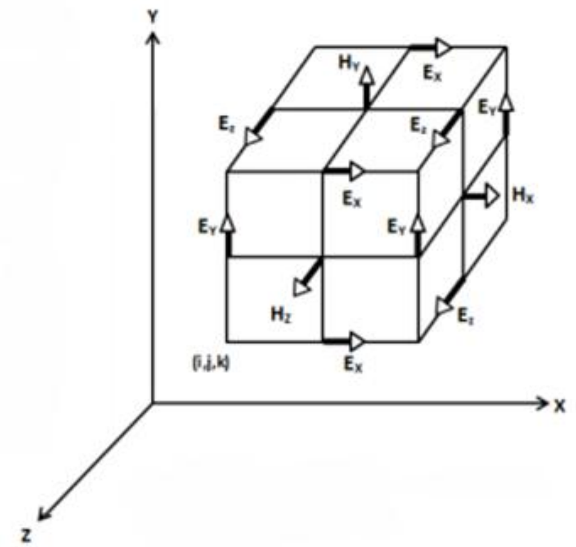

Figure 3.5 Yee's spatial grid for 3D FDTD problems.

Maxwell’s equations for a linear, non-dispersive isotropic and source free medium are given as

$$\frac{\partial \mathrm{H}}{\partial t} = -\frac{1}{\mu}\nabla \times \mathrm{E} \tag{3.39}$$

$$\frac{\partial \mathrm{E}}{\partial t} = \frac{1}{\varepsilon}\nabla \times \mathrm{H} \tag{3.40}$$

Expressing the equations (3.39)-(3.40) in scalar form gives the following six coupled differential equations

$$\frac{\partial E_z}{\partial y} - \frac{\partial E_y}{\partial z} = -\frac{\partial H_x}{\partial t} \tag{3.41}$$

$$\frac{\partial E_x}{\partial z} - \frac{\partial E_z}{\partial x} = -\frac{\partial H_y}{\partial t} \tag{3.42}$$

$$\frac{\partial E_y}{\partial x} - \frac{\partial E_x}{\partial y} = -\frac{\partial H_z}{\partial t} \tag{3.43}$$

$$\frac{\partial H_z}{\partial y} - \frac{\partial H_y}{\partial z} = \frac{\partial E_x}{\partial t} \tag{3.44}$$

$$\frac{\partial H_x}{\partial z} - \frac{\partial H_z}{\partial x} = \frac{\partial E_y}{\partial t} \tag{3.45}$$

$$\frac{\partial H_y}{\partial x} - \frac{\partial H_x}{\partial y} = \frac{\partial E_z}{\partial t} \tag{3.46}$$

For a 2D simulation in x-y domain, where there is no variation along z axis, we have

$$\frac{\partial H_y}{\partial z} = 0, \frac{\partial H_x}{\partial z} = 0, \frac{\partial E_y}{\partial z} = 0, \frac{\partial E_x}{\partial z} = 0 \tag{3.47}$$

In this thesis, Maxwell’s equations are solved in 2D considering TM polarization only. This is due to the polar property of III-Nitride materials that reduces TE polarizations and

TM polarizations are the dominant ones. The intrinsic polar property or built-in polarizations arises because of the asymmetry in the bonding between atoms and strain effects when the materials are grown on different layers as discussed in chapter 2. Thus, the set of equations (3.41)-(3.46) for TM case simplifies to

$$\frac{\partial E_x}{\partial t} = \frac{1}{\varepsilon}\frac{\partial H_z}{\partial y} \tag{3.48}$$

$$\frac{\partial E_y}{\partial t} = -\frac{1}{\varepsilon}\frac{\partial H_z}{\partial x} \tag{3.49}$$

$$\frac{\partial H_z}{\partial t} = \frac{1}{\mu}\left(\frac{\partial E_x}{\partial y} - \frac{\partial E_y}{\partial x}\right) \tag{3.50}$$

The spatial derivatives in equations (3.48)-(3.50) are discretized using central difference approximations utilizing Yee's spatial gridding scheme as follows

$$\frac{\partial E_x}{\partial t} = \frac{1}{\varepsilon}\,\frac{\big(H_z(i,j) - H_z(i,j-1)\big)}{\Delta y} \tag{3.51}$$

$$\frac{\partial E_y}{\partial t} = -\frac{1}{\varepsilon}\,\frac{\big(H_z(i,j) - H_z(i-1,j)\big)}{\Delta x} \tag{3.52}$$

$$\frac{\partial H_z}{\partial t} = \frac{1}{\mu}\left(\frac{\big(E_x(i,j+1) - E_x(i,j)\big)}{\Delta y} - \frac{\big(E_y(i+1,j) - E_y(i,j)\big)}{\Delta x}\right) \tag{3.53}$$

The central difference approximation of the time derivatives in equations (3.51)-(3.53) are again found using the Yee's algorithm and by using a leapfrog scheme shown in Figure 3.6. In this method, the H and E fields are off-set in time by half time step i.e. they are computed at time step $k + 1/2$ and k respectively to provide consistency in time.

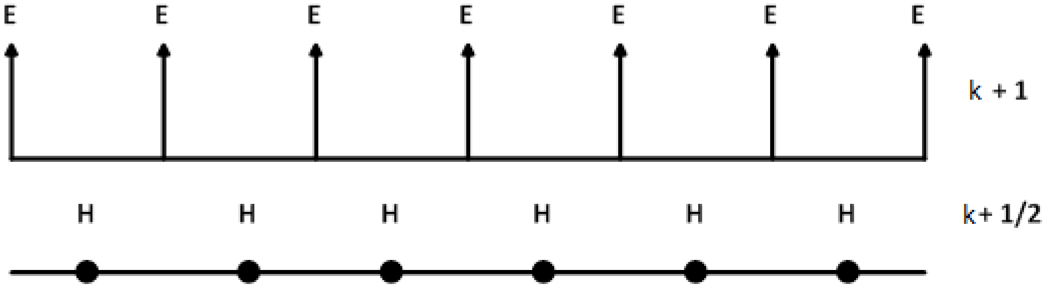

Figure 3.6 Time domain representation of Yee's algorithm (Leap frog scheme).

Therefore, the central differencing of equations (3.51)-(3.53) in time using this method gives the following update equations for solving E and H fields.

$$\frac{E_x^{k+1}\left(i+\frac{1}{2},j\right)-E_x^{k}\left(i+\frac{1}{2},j\right)}{\Delta \mathrm{t}} = -\frac{1}{\varepsilon}\,\frac{H_z^{k+\frac{1}{2}}\left(i+\frac{1}{2},j+\frac{1}{2}\right)-H_z^{k+\frac{1}{2}}\left(i+\frac{1}{2},j-\frac{1}{2}\right)}{\Delta \mathrm{y}} \tag{3.54}$$

$$\frac{E_y^{k+1}\left(i,j+\frac{1}{2}\right)-E_y^{k}\left(i,j+\frac{1}{2}\right)}{\Delta \mathrm{t}} = -\frac{1}{\varepsilon}\,\frac{H_z^{k+\frac{1}{2}}\left(i+\frac{1}{2},j+\frac{1}{2}\right)-H_z^{k+\frac{1}{2}}\left(i-\frac{1}{2},j+\frac{1}{2}\right)}{\Delta \mathrm{x}} \tag{3.55}$$

$$\frac{H_z^{k+\frac{1}{2}}\left(i+\frac{1}{2},j+\frac{1}{2}\right)-H_z^{k-\frac{1}{2}}\left(i+\frac{1}{2},j+\frac{1}{2}\right)}{\Delta \mathrm{t}} = \frac{1}{\mu}\left(\frac{E_x^{k}\left(i+\frac{1}{2},j+1\right)-E_x^{k}\left(i+\frac{1}{2},j\right)}{\Delta \mathrm{y}} - \frac{E_y^{k}\left(i+1,j+\frac{1}{2}\right)-E_y^{k}\left(i,j+\frac{1}{2}\right)}{\Delta \mathrm{x}}\right) \tag{3.56}$$

At each time step the new values of E at all grid points are calculated using the previous values of E and the new values of H and are stored for next time step. Similarly, at each time step, the new values of H field are computed using the previous values of H and the new values of E.

For GaN LED simulation, the equations (3.54)-(3.55) with external current density sources J are modified as

$$\frac{E_x^{k+1}\left(i+\frac{1}{2},j\right)-E_x^{k}\left(i+\frac{1}{2},j\right)}{\Delta \mathrm{t}} = -\frac{1}{\varepsilon}\,\frac{H_z^{k+\frac{1}{2}}\left(i+\frac{1}{2},j+\frac{1}{2}\right)-H_z^{k+\frac{1}{2}}\left(i+\frac{1}{2},j-\frac{1}{2}\right)}{\Delta \mathrm{y}} - \frac{1}{\varepsilon}\left(J_x^{k+\frac{1}{2}}\left(i+\frac{1}{2},j\right)\right) \tag{3.57}$$

$$\frac{E_y^{k+1}\left(i,j+\frac{1}{2}\right)-E_y^{k}\left(i,j+\frac{1}{2}\right)}{\Delta \mathrm{t}} = -\frac{1}{\varepsilon}\,\frac{H_z^{k+\frac{1}{2}}\left(i+\frac{1}{2},j+\frac{1}{2}\right)-H_z^{k+\frac{1}{2}}\left(i-\frac{1}{2},j+\frac{1}{2}\right)}{\Delta \mathrm{x}} - \frac{1}{\varepsilon}\left(J_y^{k+\frac{1}{2}}\left(i,j+\frac{1}{2}\right)\right) \tag{3.58}$$

There is an upper limit on the time step of optical model Δt for stability of the discretization in time using Yee's FDTD algorithm in accordance with spatial increment Δx and Δy. This is given by the Courant-Friedrich-Levy (CFL) stability condition [55]. For the two dimension case, it is given as

$$(\Delta t)_{optical} \leq (\Delta t)_{max} = \frac{1}{c\sqrt{\left(\frac{1}{\Delta x^2}+\frac{1}{\Delta y^2}\right)}} \tag{3.59}$$

where c is the velocity of light in the medium.

3.3.2 Auxiliary Differential Equation (ADE)-FDTD

The representation of FDTD algorithm that takes into account the dispersive material properties is formulated using an ADE-FDTD algorithm [53]. In this method, the frequency dependent polarization is converted into time domain using inverse Fourier transform. A more generalized algorithm that includes the most general form of dispersion is represented by a general ADE-FDTD algorithm [52] that can include a multi-pole Lorentz-Drude or Lorentz model. Thus, to model dispersive materials using FDTD, the frequency dependent polarization is converted into time domain polarization using inverse Fourier transform of the constitutive relation using the following procedure.

The polarization using a Lorentzian function (equation (2.30)) for a single pole is given as

$$P(\omega) = \frac{a}{b + jc\omega - d\omega^2} E(\omega) \tag{3.60}$$

Taking the inverse Fourier transform of equation (3.60) and rearranging the terms, it simplifies to

$$bP(t) + cP'(t) + dP''(t) = aE(t) \tag{3.61}$$

The first and second order discretization of equation (3.61) gives the following equation

$$bP^k + c\frac{P^{k+1} - P^{k-1}}{2\Delta t} + d\frac{P^{k+1} - 2P^k + P^{k-1}}{\Delta t^2} = aE^k \tag{3.62}$$

Therefore, the update equation for time domain polarization after rearranging the terms in equation (3.62) is obtained as

$$P^{k+1} = C_1 P^k + C_2 P^{k-1} + C_3 E^k \tag{3.63}$$

where, $C_1 = \frac{4d-2b\Delta t^2}{2d+c\Delta t}, C_2 = \frac{-2d+c\Delta t}{2d+c\Delta t}, C_3 = \frac{2a\Delta t^2}{2d+c\Delta t}$.

Now, the update equation for the electric field using equation (2.22) becomes

$$E^{k+1} = \frac{D^{k+1} - P^{k+1}}{\varepsilon_0 \varepsilon_\infty} \tag{3.64}$$

Since the dispersive materials used in this thesis are modeled using the multi-pole Lorentz-Drude model, the above formulation for calculating the time domain polarization can be modified as

$$P_i^{k+1} = C_{1i} P_i^k + C_{2i} P_i^{k-1} + C_{3i} E_i^k \tag{3.65}$$

$$with\ C_{1i} = \frac{4d_i - 2b_i \Delta t^2}{2d_i + c_i \Delta t}, C_{2i} = \frac{-2d_i + c_i \Delta t}{2d_i + c_i \Delta t}, C_{3i} = \frac{2a_i \Delta t^2}{2d_i + c_i \Delta t} \tag{3.66}$$

where, $i = 1,2,3 \ldots, N$

Therefore equation (3.64) for a multi-pole case becomes

$$E^{k+1} = \frac{\left(D^{k+1} - \sum_i^N P_i^{k+1}\right)}{\varepsilon_0 \varepsilon_\infty} \tag{3.67}$$

Figure 3.7 shows the FDTD algorithm for modeling the electromagnetic part of the device. It describes the flow of calculations of EM fields inside the time loop using the generalized polarization algorithm.

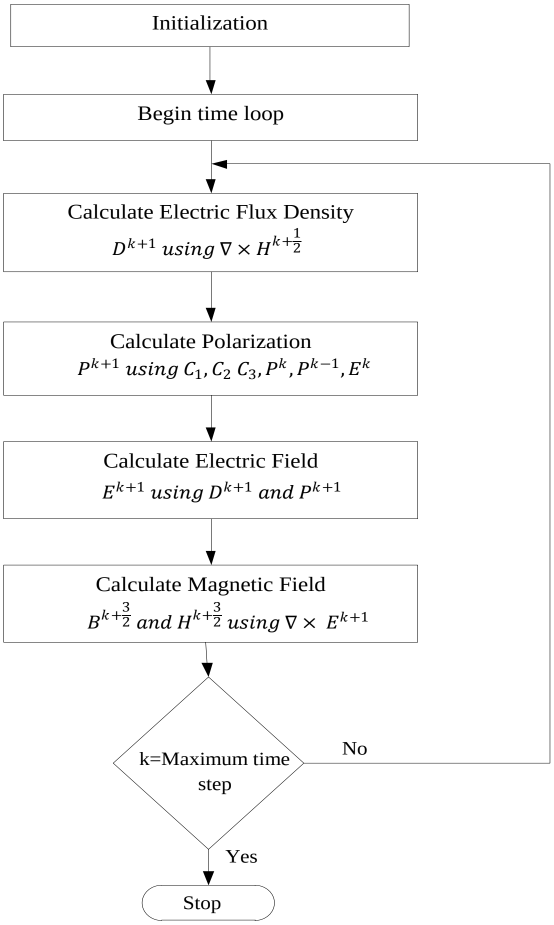

Figure 3.7 Flowchart of general ADE-FDTD algorithm (Optical model).

3.3.3 Absorbing boundary conditions to solve EM fields

Appropriate boundary conditions must be used to absorb the EM waves at the boundaries. Perfectly matched layer (PML) is used as an absorbing boundary conditions in an FDTD computational domain [58]. It uses a specific condition on electric and magnetic conductivity values to absorb the EM wave at the boundary or across a vacuum-medium interface with no reflections. In this thesis, we use a more generalized PML i.e. Material Independent PML (MIPML) which can be used as absorbing boundary conditions for any type of FDTD simulation boundaries [59]. For TM case, the equations (3.48)-(3.50) with electric and magnetic conductivity terms are modified as

$$\frac{\partial D_x}{\partial t} + \sigma_y^D D_x = \frac{\partial H_z}{\partial y} \tag{3.68}$$

$$\frac{\partial D_y}{\partial t} + \sigma_x^D D_y = -\frac{\partial H_z}{\partial x} \tag{3.69}$$

$$\frac{\partial B_{zx}}{\partial t} + \sigma_x^B B_{zx} = -\frac{\partial E_y}{\partial x} \tag{3.70}$$

$$\frac{\partial B_{zy}}{\partial t} + \sigma_y^B B_{zy} = -\frac{\partial E_x}{\partial y} \tag{3.71}$$

In this technique, the EM waves are transmitted at the vacuum-medium interface with no reflections at boundaries by using the following condition on the electric and magnetic conductivities $\sigma^D$and σ^B respectively.

$${\sigma_{x(y)}}^D = \sigma_{x(y)}^B \tag{3.72}$$

Where D and B correspond to electric and magnetic fields respectively, σ^D and σ^B are calculated as

$$\sigma^{D(B)}(\rho) = \sigma_{max}^{D(B)} \left(\frac{\rho}{\delta}\right)^n, \tag{3.73}$$
$$\sigma_{max}^{D(B)} = -\frac{(n+1)c \log R_0}{2\delta}$$

Where,$\rho = x \; or \; y, \delta = npml \times \Delta x \; or \; npml \times \Delta y$, $npml$ is the number of PML cells.

c is the velocity of light inside the medium, $n = 3$ and $R_0 = 10^{-6}$ are constant.

3.3.4 Total Field/ Scattered Field (TFSF) boundary conditions for scattering characteristics

The scattering properties of materials can be studied by determining the scattered EM fields using TF/ SF theory. In this formulation, the total field is split into two components

$$E_{total} = E_{inc} + E_{scat} \qquad H_{total} = H_{inc} + H_{scat} \tag{3.74}$$

To determine the scattered fields, the simulation domain is divided in TF and SF regions (Figure 3.8 TF/ SF domain). In a TF region, the EM fields are the sum of both incident and scattered fields, whereas in SF region, the EM fields are purely scattered fields with no incident fields. TF/SF boundary conditions are therefore used to realize a plane wave source that corresponds to total fields in Region 1 and scattered fields in Region 2.

The incident plane wave source at the TF/SF boundary is generated by simulating a pulse on an auxiliary 1-D grid at the source point and mapping it into two dimensional grid. In region 1, the solution of Maxwell's equation yields total fields, whereas in region 2, it gives scattered fields. However, when the fields are solved using Yee's mesh, an inconsistency arises at the TF/ SF boundary.

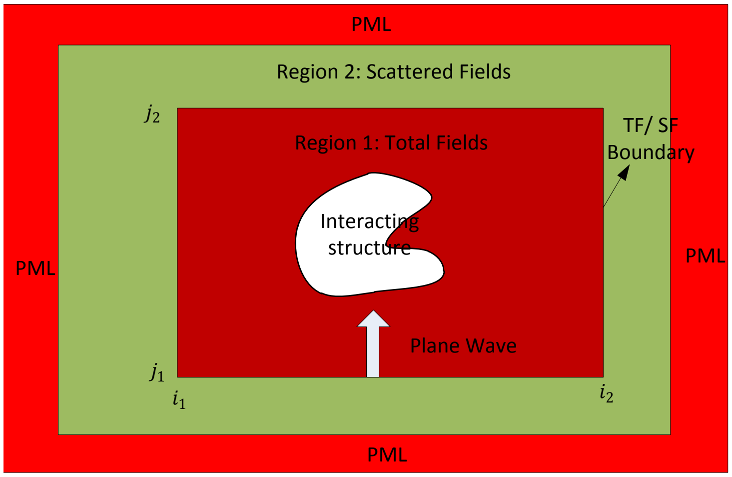

Figure 3.8 TF/ SF domain.

For example, the solution of E_x in Region 1 and Region 2 given by equation (3.54) can be written as

Region 1 (Total Field Region):

$$E_{x,total}^{k+1}\left(i+\frac{1}{2},j\right)= \tag{3.75}$$

$$E_{x,total}^{k}\left(i+\frac{1}{2},j\right)-\frac{\Delta\mathrm{t}}{\varepsilon\Delta\mathrm{y}}\left(H_{z,total}^{k+\frac{1}{2}}\left(i+\frac{1}{2},j+\frac{1}{2}\right)-H_{z,total}^{k+\frac{1}{2}}\left(i+\frac{1}{2},j-\frac{1}{2}\right)\right)$$

Region 2 (Scattered Field Region):

$$E_{x,scat}^{k+1}\left(i+\frac{1}{2},j\right)= \tag{3.76}$$

$$E_{x,scat}^{k}\left(i+\frac{1}{2},j\right)-\frac{\Delta\mathrm{t}}{\varepsilon\Delta\mathrm{y}}\left(H_{z,scat}^{k+\frac{1}{2}}\left(i+\frac{1}{2},j+\frac{1}{2}\right)-H_{z,scat}^{k+\frac{1}{2}}\left(i+\frac{1}{2},j-\frac{1}{2}\right)\right)$$

At the TF/ SF boundary ($i_1\ to\ i_2, j_1$), the solution would become (if boundary is assumed to be total field region)

$$E_{x,total}^{k+1}\left(i+\frac{1}{2},j_1\right)= \tag{3.77}$$

$$E_{x,total}^{k}\left(i+\frac{1}{2},j_1\right)-\frac{\Delta \mathrm{t}}{\varepsilon\Delta \mathrm{y}}\left(H_{z,total}^{k+\frac{1}{2}}\left(i+\frac{1}{2},j_1+\frac{1}{2}\right)-H_{z,scat}^{k+\frac{1}{2}}\left(i+\frac{1}{2},j_1-\frac{1}{2}\right)\right)$$

The inconsistency in the fields in equation (3.77) can be removed by using equation (3.74) for $H_{z,scat}$ i.e.

$$E_{x,total}^{k+1}\left(i+\frac{1}{2},j_1\right)= \tag{3.78}$$

$$E_{x,total}^{k}\left(i+\frac{1}{2},j_1\right)-\frac{\Delta \mathrm{t}}{\varepsilon\Delta \mathrm{y}}\left(H_{z,total}^{k+\frac{1}{2}}\left(i+\frac{1}{2},j_1+\frac{1}{2}\right)-H_{z,total}^{k+\frac{1}{2}}\left(i+\frac{1}{2},j_1-\frac{1}{2}\right)\right)+$$
$$\frac{\Delta \mathrm{t}}{\varepsilon\Delta \mathrm{y}}H_{z,inc}^{k+1/2}\left(i+\frac{1}{2},j_1-\frac{1}{2}\right)$$

Equation (3.78) can be simplified as

$$E_{x,total}^{k+1}\left(i+\frac{1}{2},j_1\right)=E_{x,total}^{k+1}\left(i+\frac{1}{2},j_1\right)\ +\ \frac{\Delta \mathrm{t}}{\varepsilon\Delta \mathrm{y}}H_{z,inc}^{k+1/2}\left(i+\frac{1}{2},j_1-\frac{1}{2}\right) \tag{3.79}$$

Similarly, corrections to the electric and magnetic fields are applied on remaining TFSF boundaries. The scattering properties are obtained by taking Fourier transform of the time samples of the fields stored at each time step.

The incident electric and magnetic fields: $H_{z,inc}$, $E_{x,inc}$ and $E_{y,inc}$ are calculated using FDTD on Maxwell's equations in 1-D auxiliary computational domain as shown below

$$E_{1D,inc}^{k+1}(m)=\ E_{1D,inc}^{k}(m)+\frac{\Delta t}{\varepsilon\Delta x}\left(H_{1D,inc}^{k+\frac{1}{2}}(m-1/2)-H_{1D,inc}^{k+\frac{1}{2}}(m+1/2)\right) \tag{3.80}$$

$$H_{1D,inc}^{k+\frac{1}{2}}\left(m+\frac{1}{2}\right)$$
$$=H_{1D,inc}^{k-\frac{1}{2}}\left(m+\frac{1}{2}\right)+\frac{\Delta t}{\mu_o\Delta x}\left(E_{1D,inc}^{k}(m)-E_{1D,inc}^{k}(m+1)\right) \tag{3.81}$$

3.4 Summary

The formulation of Finite-Difference Time Domain (FDTD) algorithm to solve active part and the electromagnetic part of GaN LEDs is elucidated in this chapter. The solution of coupled partial differential equations in time domain is given by the update equations that give the values of different parameters i.e. electrostatic potential, carrier concentrations, EM fields at each time step and at each grid point in the simulation domain. The boundary conditions used to solve these update equations are also discussed. It also explains the TF/SF theory for determining scattering characteristics.

CHAPTER 4

CARRIER TRANSPORT SIMULATION OF GaN LEDs

4.1 Introduction

The carrier transport simulation of GaN LEDs based on FDTD DD model is investigated in this chapter. The numerical simulations are performed to understand the physics involved in the operation of III-Nitride LEDs. The detailed electronic characteristics starting from the band diagrams till the electron-hole pair recombinations of a semiconductor LED using the formulated model will be discussed. The initial verification of the DD model is performed by simulating a simple p-n junction in 1D and comparing the results with the analytical values. The overall verification of the simulation model for LED is done in chapter 6 by comparing emission of homojunction GaN LED obtained from coupled model with that of the experimental data in [5].

4.2 Verification of Drift Diffusion Transport Model

The verification is done on a GaN p-n junction in 1D. The p-n junction is simulated at zero applied potential (thermal equilibrium) and the analytical and simulated values of built-in potential, depletion widths, peak electric field at the p-n junction and volume charge density are compared.

The analytical expressions of peak electric field, built-in potential, depletion widths and volume charge density for any p-n junction are given by the following equations [15]:

$$E_{peak} = -\frac{qN_a}{\epsilon_s}\left(x_p\right) = -\frac{qN_d}{\epsilon_s}(x_n) \tag{4.1}$$

$$V_{bi} = \frac{k_B T}{q}\ln\left(\frac{N_a N_d}{n_i^2}\right) \tag{4.2}$$

$$x_n = \left\{\frac{2\epsilon_s V_{bi}}{q}\left[\frac{N_a}{N_d}\right]\left[\frac{1}{N_a + N_d}\right]\right\}^{\frac{1}{2}}, x_p = \left\{\frac{2\epsilon_s V_{bi}}{q}\left[\frac{N_d}{N_a}\right]\left[\frac{1}{N_a + N_d}\right]\right\}^{\frac{1}{2}}, \\ w = x_n + x_p \tag{4.3}$$

$$\rho(x) = -qN_a, -x_p < x < 0 \\ \rho(x) = qN_d, 0 < x < x_n \tag{4.4}$$

4.2.1 Simulation of GaN p-n junction in 1D

In this test, a GaN p-n junction in 1D is simulated using FDTD DD model with the parameters given in Table 4.1. The simulated and analytical distributions of electric field, electrostatic potential and volume charge densities under thermal equilibrium or zero applied bias are shown in Figure 4.1 to Figure 4.3. The high value of built-in voltage compared to Si p-n junction is due to very low intrinsic concentration of GaN layers. The simulated volume charge density in the p-side or the n-side depletion region shown in Figure 4.3 is almost same as the analytical values obtained using (4.4).

Table 4.1 Parameter values used in simulation of 1-D GaN p-n junction

Parameter	Value
Carrier concentration of n and p layers, $N_a\ and\ N_d\ [cm^{-3}]$	10^{17}
Intrinsic carrier concentration of GaN $n_i [cm^{-3}]$.	$3.567\ \times 10^{-11}$
Thickness of p and n layers $[\mu m]$	1.0
Static dielectric constant of GaN ϵ_s	9.7
Spatial Step $\Delta x\ [nm]$	10
Temporal step $\Delta t\ [fs]$	0.5

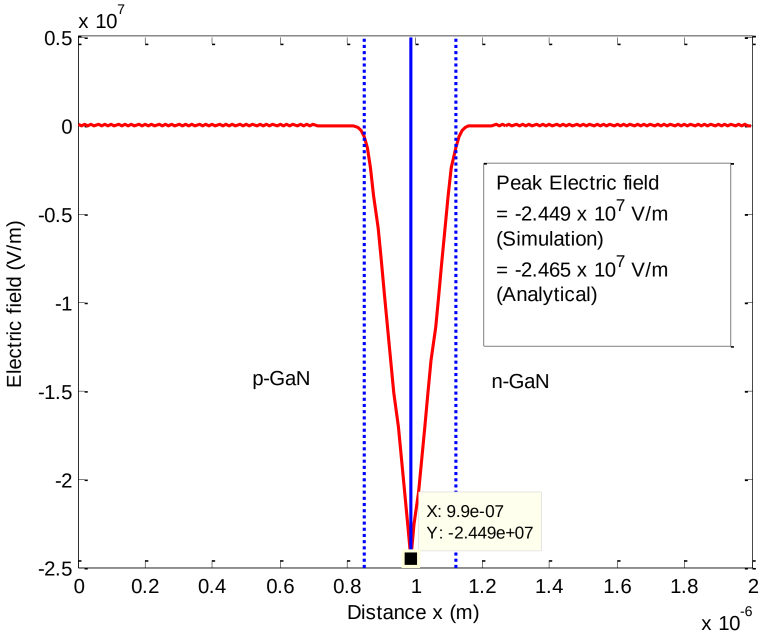

Figure 4.1 Simulated Electric Field distribution (1D GaN p-n junction) at zero applied potential.

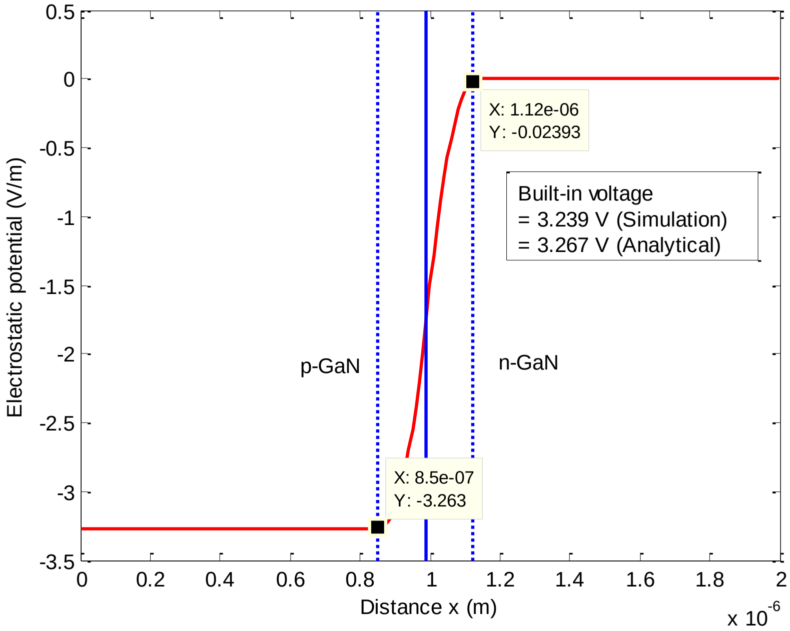

Figure 4.2 Simulated Electrostatic potential distribution (1D GaN p-n junction) at zero applied potential.

Thus, the simulated parameters are in good agreement with the calculated analytical values using equations (4.1)-(4.4).

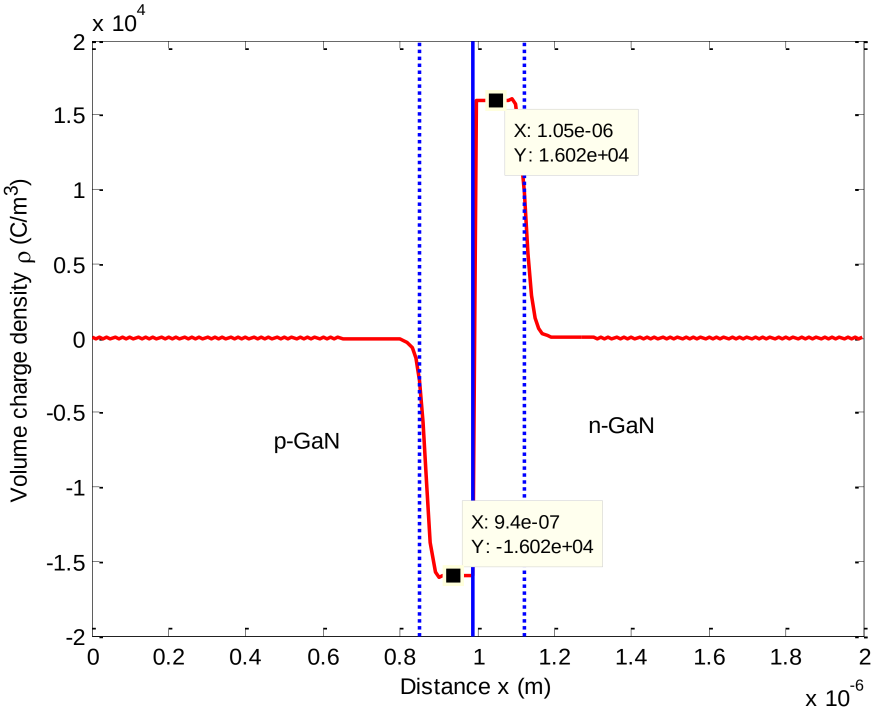

Figure 4.3 Simulated volume charge density (1D GaN p-n junction) at zero applied potential.

4.3 Analysis of a basic p-GaN/n-GaN homojunction LED

The first LED structure to be analyzed using the FDTD DD electronic simulation model is a basic 2D p-GaN/ n- GaN homojunction UV LED with an emission wavelength at 365 nm. The carrier transport is studied through the formulated simulation model. The simulated structure shown in Figure 4.4 consists of a $300\ nm$ p-GaN layer with a doping of $10^{17} cm^{-3}$, $1\ \mu m$ n-GaN layer doped at $10^{17} cm^{-3}$, $100\ nm$ intrinsic GaN buffer layer and a $1\ \mu m$ sapphire substrate layer. The LED structure is biased to $V_p = V_{applied} - V_{bi}$ (p-contact) and $V_n = 0$ (n-contact). The FDTD simulation domain is $100\ \times 341$ grid points with $\Delta x = \Delta y = 10\ nm$ and $\Delta t = 0.5\ fs$. The parameters used in simulation of homojunction LED are given in Table 4.2. The simulations are run until the solutions of the electronic model reaches steady state.

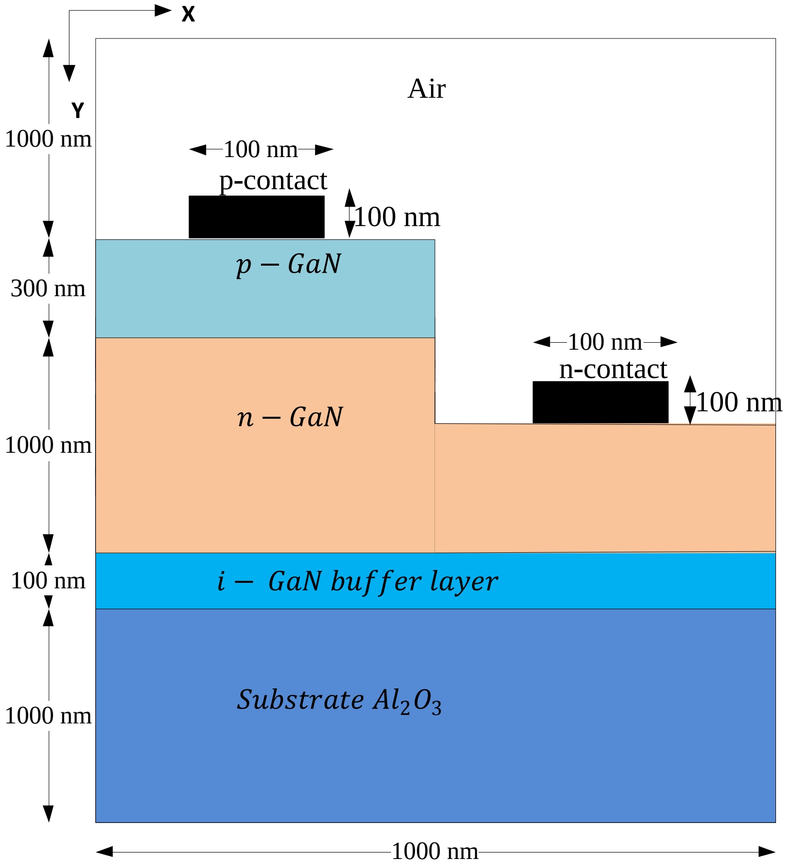

Figure 4.4 Schematic of a basic p-GaN/ n- GaN homojunction LED.

4.3.1 Energy Bands, Carrier Concentrations, Recombination Rates and Injection currents

The energy band diagrams representing the conduction band, valence band, electron and hole Fermi levels are obtained from the electrostatic potential and carrier densities that are solved using the formulated model. The energy levels are given by the following equations,

$$E_c = k_B T \ log\left(\frac{N_c}{n_i}\right) - qV \tag{4.5}$$

$$E_i = E_c - E_g/2 \tag{4.6}$$

$$E_v = E_c - E_g \tag{4.7}$$

$$E_{fn} = E_i + k_B T \ log\left(\frac{n}{n_i}\right) \tag{4.8}$$

$$E_{fp} = E_i - k_B T \ log\left(\frac{p}{n_i}\right) \tag{4.9}$$

Table 4.2 Parameter values used in simulation ([34], [36], [47], [60]).

Parameter	**Value**
Carrier concentration in p-layers N_a (cm^{-3})	10^{17}
Carrier concentration in n-layers N_d (cm^{-3})	10^{17}
Static Dielectric constant ε_r (GaN)	9.7
Band gap E_g (eV) (GaN)	3.4
Low field electron mobility $\mu_{no}(cm^{-2}V^{-1}s^{-1})$	880
Low field hole mobility $\mu_{po}(cm^{-2}V^{-1}s^{-1})$	35
Effective density of states (electrons) N_c (cm^{-3})	2.23×10^{18}
Effective density of states (holes) N_v (cm^{-3})	4.624×10^{19}
Dielectric constant ε_r (Al_2O_3)	3.218
SRH recombination coefficient A (s^{-1})	1×10^5
Radiative recombination coefficient B $(cm^{-3}s^{-1})$	1×10^{-8}
Auger recombination coefficient C $(cm^{-6}s^{-1})$	1×10^{-30}

The energy band diagrams at zero applied potential and in forward bias are shown in Figure 4.5 and Figure 4.6 respectively. It can be observed that the energy barrier in the depletion region is reduced with the increase in the applied potential. Thus, the electrons and holes can easily move into p and n layers respectively under forward bias.

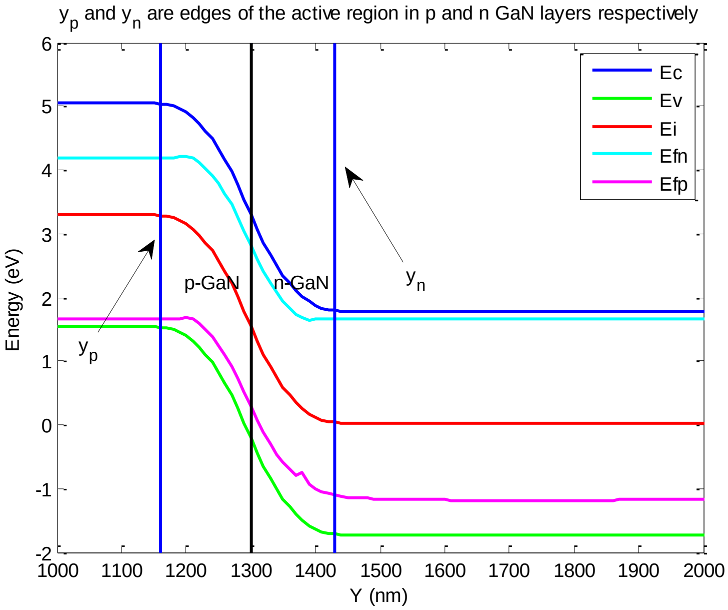

Figure 4.5 Energy band diagram of p-n homojunction GaN LED at zero applied voltage.

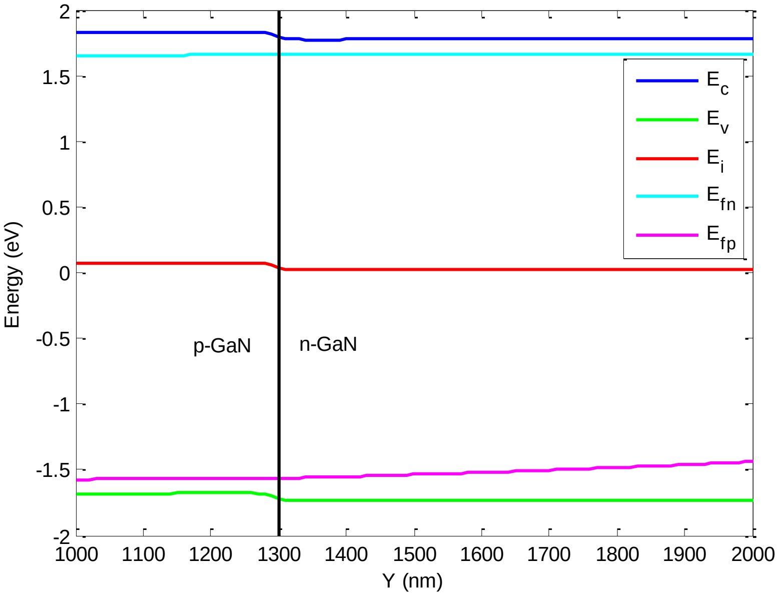

Figure 4.6 Energy band diagram of p-n homojunction GaN LED in forward bias.

E_c and E_v are conduction and valence bands respectively, E_{fn} and E_{fp} are electron and hole Fermi levels respectively, and E_i is the intrinsic Fermi level.

The UV LED structure in Figure 4.4 is investigated for the electronic distributions and the most important parameter, the electron-hole pair recombination rates that decide the output light intensity and external quantum efficiencies of GaN LED structures. The simulated steady state electronic distributions solved using the time domain DD transport model are shown in Figure 4.7 to Figure 4.12. It can be seen in Figure 4.7 and Figure 4.8 that the potential starts from a high value at the p-contact and reaches low values as we go towards the side n-contact at forward bias conditions. As soon as the potential distribution is found, the electron and hole currents can be computed using the current density equations.

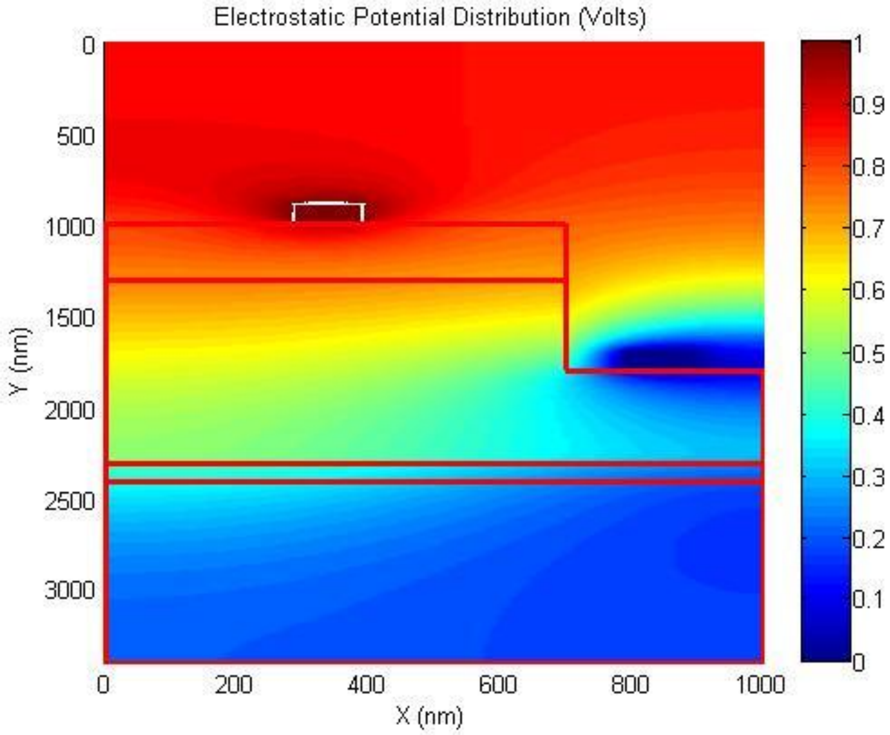

Figure 4.7 Simulated Electrostatic potential distribution of p-n homojunction GaN LED ($V_{applied}$=4.267 V).

The current spreading mechanism associated with such configuration of the LED structure from p-contact to n- contact can also be seen in Figure 4.9. It can also be observed that the electron current flowing from p-contact to n-contact is high near the contacts because of non-uniform potential distribution between these contacts.

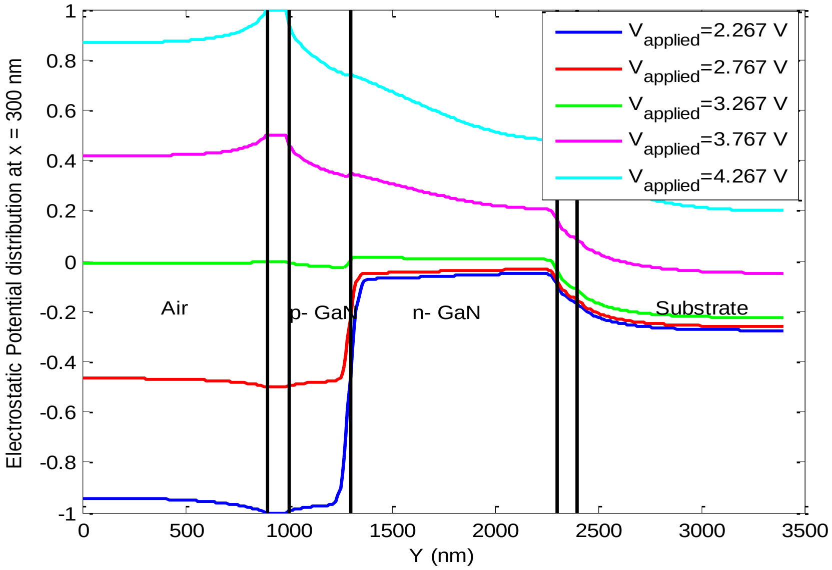

Figure 4.8 Electrostatic potential distribution for different bias (p-n homojunction GaN LED).

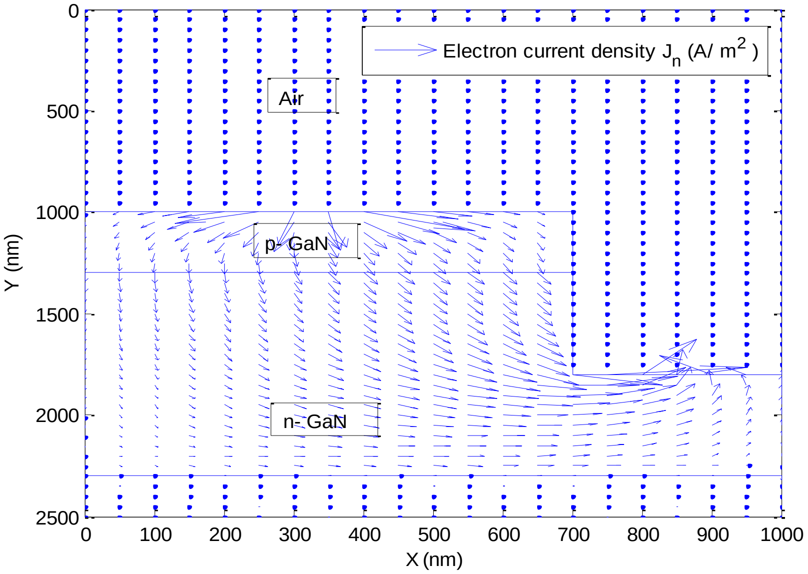

Figure 4.9 Electron current density distribution of p-n homojunction GaN LED ($V_{applied}$=4.267 V).

Thus, with the potential and the current density distributions obtained, the electron and hole concentrations are found using the carrier continuity equations. The distribution of electron and holes along the device is shown in Figure 4.10. The increase in the forward voltage results in an increase in the charge carriers on either side of the p-n junction.

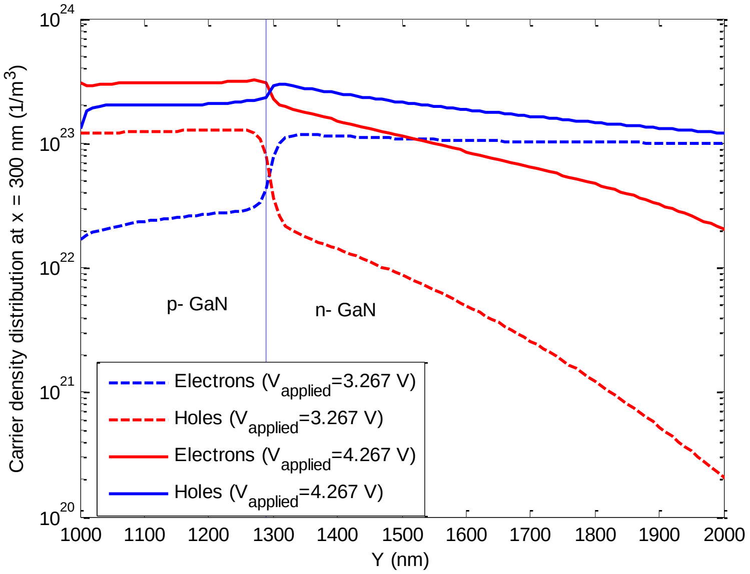

Figure 4.10 Comparison of carrier density distribution of p-n homojunction GaN LED at different applied voltages.

The electron concentration in the p-region decreases at a slower rate as compared to the hole concentration in the n-region because of high electron mobility of GaN than the hole mobility. The recombination rates computed from the electron and hole distributions using the recombination models are shown in Figure 4.11.

It can be seen that the radiative recombinations are stronger than the non- radiative recombinations for the recombination coefficients given in Table 4.2. It is also clear that the recombination rates are high at the junction resulting from the large number of electron-hole pairs at the junction. At high injection currents i.e. at high applied voltages as seen in Figure 4.13, the electron-hole pairs increase that lead to high recombination rates as it can be seen in Figure 4.12. Figure 4.14 shows the current- voltage (I-V) characteristics of a p-n homojunction GaN LED. The LED forward voltage V_r is 3.267 V at 14.06 A/m injection current as shown in Figure 4.14.

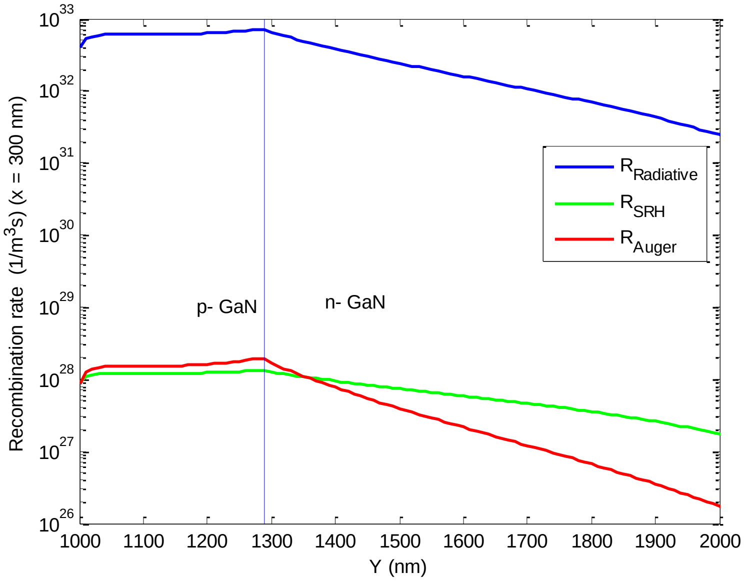

Figure 4.11 Electron hole pair recombination distribution- radiative and non-radiative ($V_{applied}$=4.267 V).

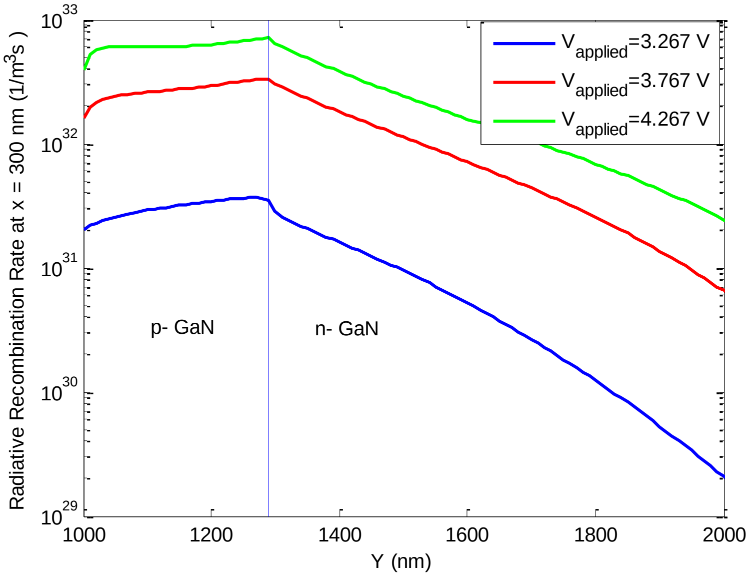

Figure 4.12 Radiative recombination rate of p-n homojunction GaN LED at different applied voltages.

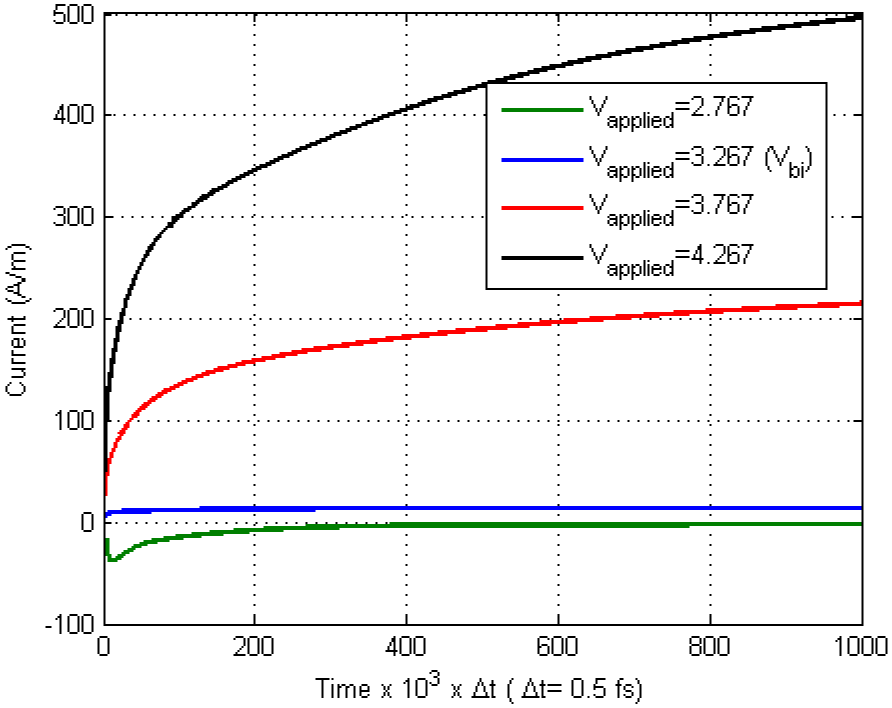

Figure 4.13 Injection current as a function of time (p-n homojunction GaN LED).

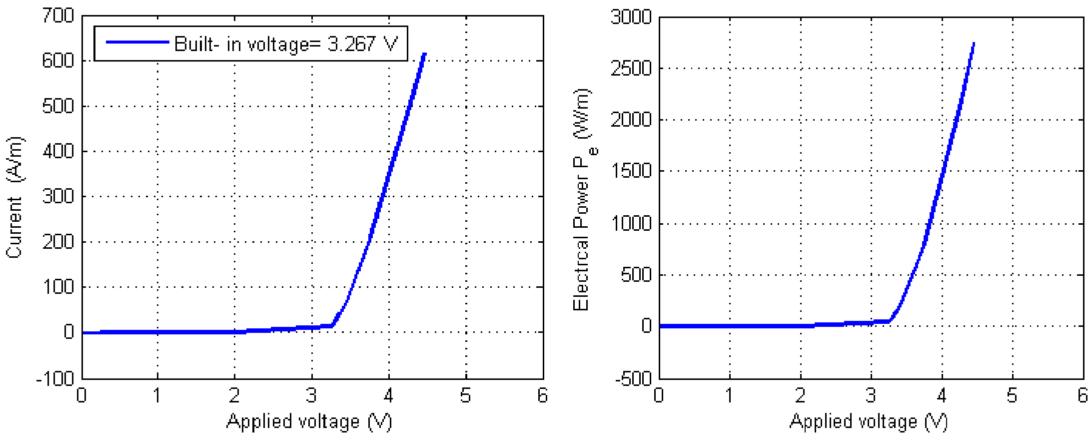

(a) **(b)**

Figure 4.14 a) Current- voltage ($I - V$) and b) Electrical Power-voltage (P_e -V) characteristics of p-n homojunction GaN LED.

4.3.2 Effect of Field dependent models (FDM) and recombination models (RM)

The effect of field dependent transport parameters of GaN material discussed in chapter 2 is investigated for the LED structure. The current-voltage characteristics with and without the FDM and RM are shown in Figure 4.15. It can be seen that the injection currents decrease in the presence of these models and this decrease is higher at high forward voltages. This decrease results from the low mobility and diffusion coefficients and strong recombination rates at high forward voltages as seen in Figure 2.1, Figure 2.2 and Figure 4.12.

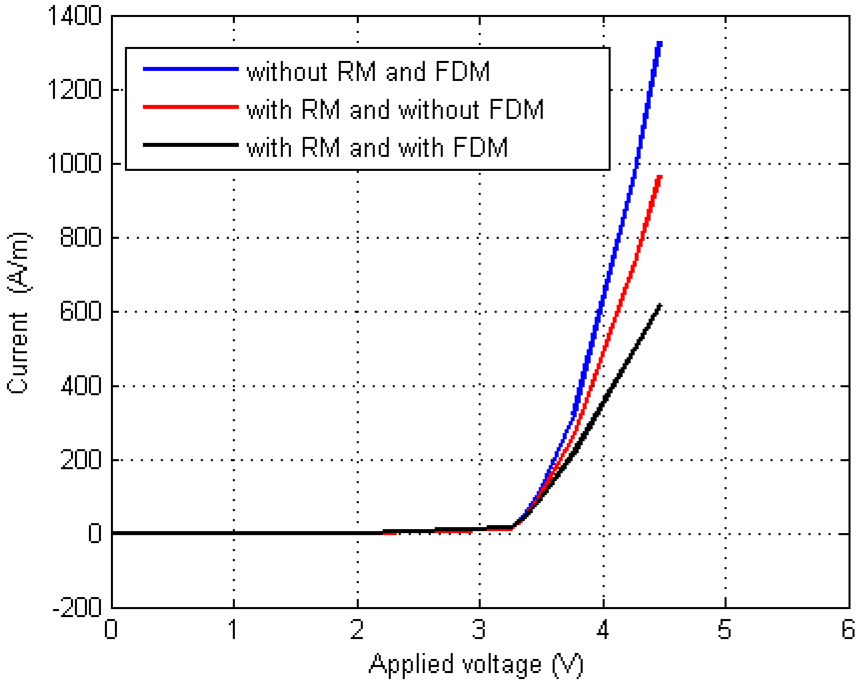

Figure 4.15 Effect of field dependent and recombination models on I-V characteristics.

4.4 Analysis of a basic p-GaN/ i- GaN/ n-GaN homojunction LED

The second LED structure that is analyzed numerically is a p-GaN/ i (intrinsic) - GaN/ n-GaN UV LED shown in Figure 4.16. An addition of intrinsic GaN layer increases the active region that leads to high electron-hole pair recombinations as compared to that of p-n GaN LED. The structure is obtained from the p-n GaN LED by removing part of p-

GaN layer and adding an intrinsic GaN layer. It consists of a $200\ nm$ p-GaN layer doped at $10^{17}\ cm^{-3}$, $100\ nm$ intrinsic GaN layer with a doping of $10^{15}\ cm^{-3}$, $1\ \mu m$ n- GaN layer doped at $10^{17}\ cm^{-3}$, $100\ nm$ intrinsic GaN buffer layer, $1\ \mu m\ Al_2O_3$ substrate layer and $100\ nm\ \times 100\ nm$ Au contacts. The device dimensions are$1\ \mu m\ \times 3.4\ \mu m$. The parameter values used in simulation are same as that of p-n GaN LED given in Table 4.2. The device is biased to $V_p = V_{applied} - V_{bi}$ (p-contact) and $V_n = 0$ (n-contact).

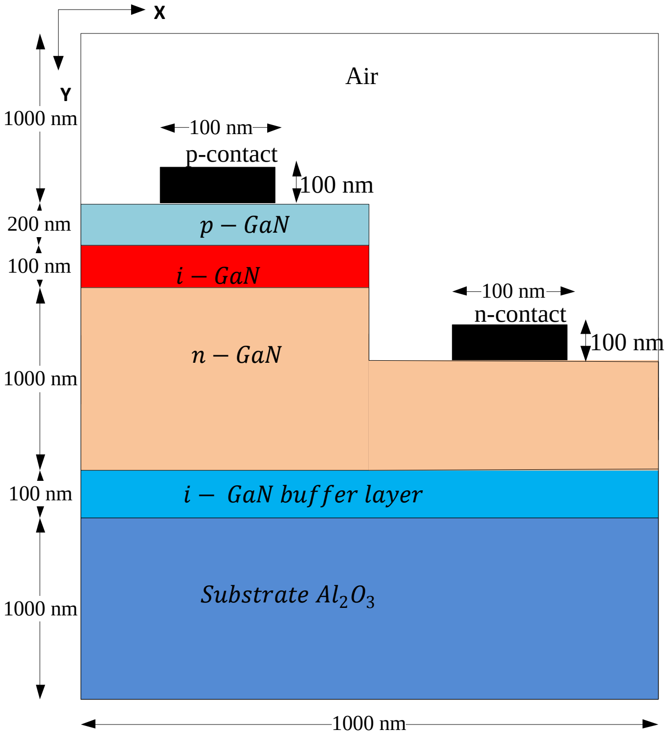

Figure 4.16 Schematic of p-GaN/ i- GaN/ n-GaN LED.

4.4.1 Energy Bands, Recombination Rates and Injection currents

The energy band diagrams at equilibrium and at forward bias for the LED structure with intrinsic GaN layer sandwiched between p and n GaN layers are shown in Figure 4.17

and Figure 4.18. A linear potential distribution in the intrinsic region can be observed in Figure 4.17.

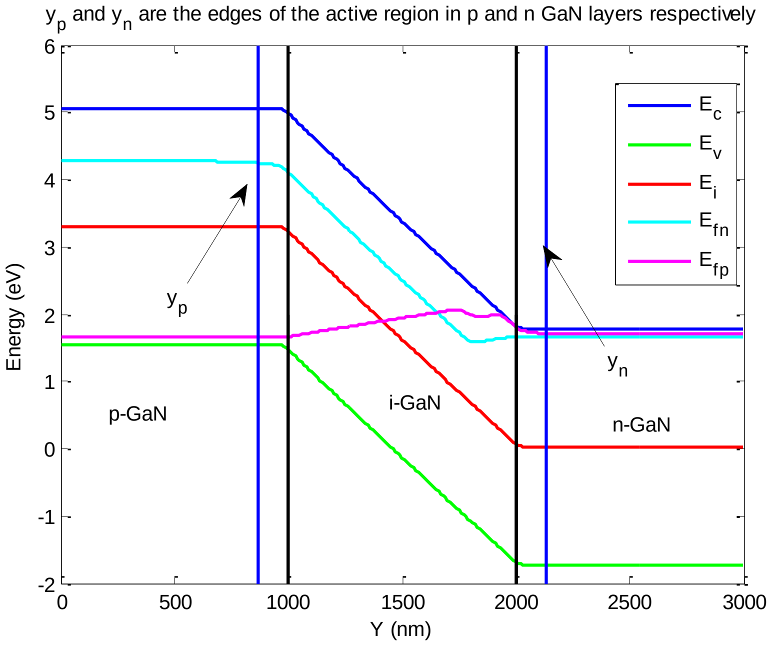

Figure 4.17 Energy band diagram of p-i-n GaN LED at zero applied voltage.

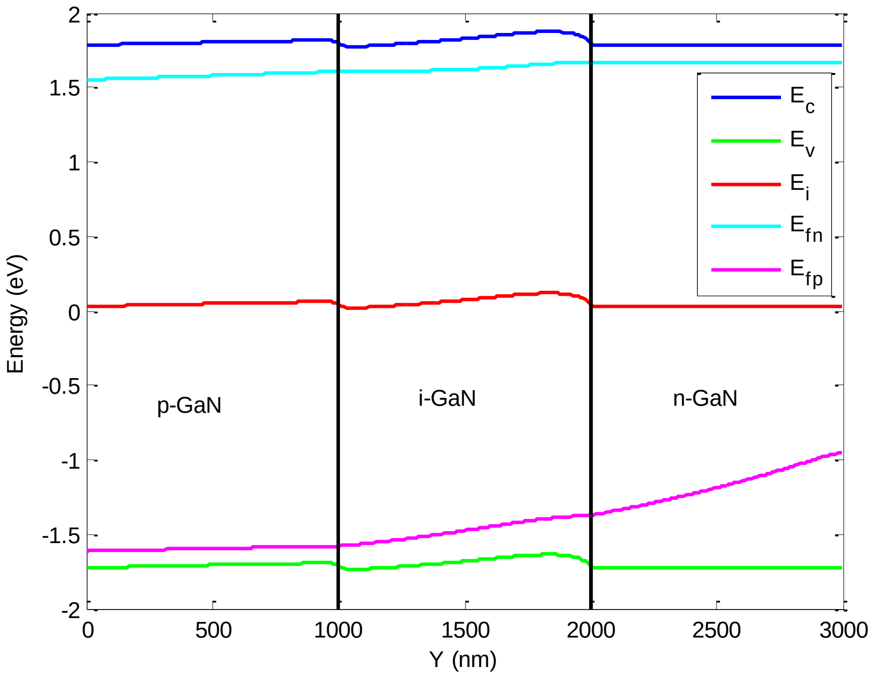

Figure 4.18 Energy band diagram of p-i-n GaN LED at forward bias.

The probability of electrons or holes to recombine in this region increases with such potential barrier that also increases the width of active region. A similar barrier in the conduction band and valence band energies can be seen in Figure 4.18 that leads to increase in the recombination area. The intrinsic layer increases the energies in the active region (Figure 4.18) as compared to that of energies inside the p-n LED (Figure 4.6) because of linear potential distribution that accumulates the carrier across that region.

The steady state dc distributions obtained by solving the FDTD DD equations are compared with the p-n GaN LED. Figure 4.19 shows the electrostatic potential along the width of the device and at $x = 300\, nm$ for different applied voltages. The difference in the potential distributions and recombination rates can be seen in the intrinsic region due to the difference in the energy band gaps of the two LEDs as shown in Figure 4.19 and Figure 4.20. The solid lines correspond to the p-n GaN LED and the dashed lines correspond to the p-i-n GaN LED. The area under the radiative recombination rate curve

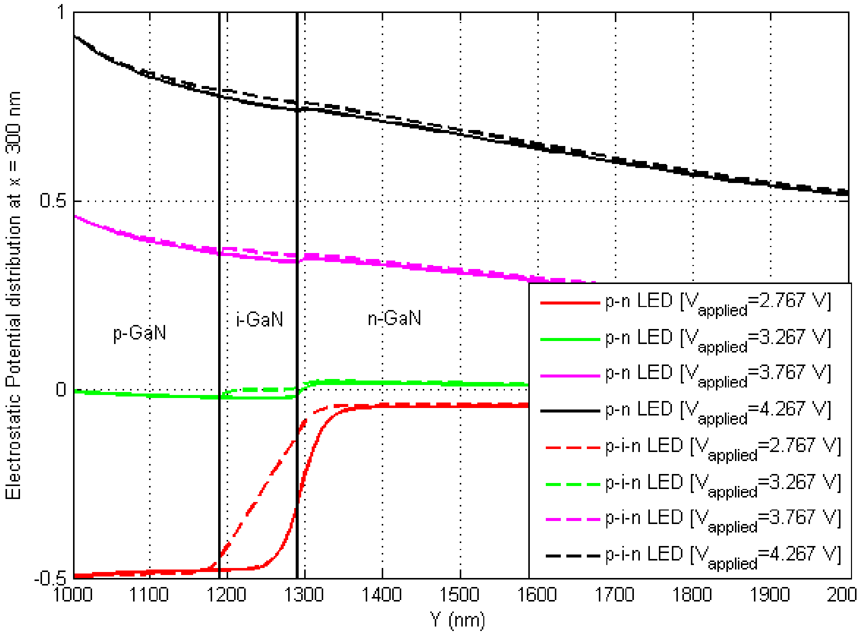

Figure 4.19 Electrostatic potential distribution at x= 300 nm (p-n vs. p-i-n GaN LEDs).

for p-i-n LED is higher than that of p-n LED because of increase in the carrier density, active region and high carrier injection at high applied voltage. Figure 4.21 shows the simulated injection current- time curve of p-i-n GaN LED. As the voltage is increased from 3.267 V to 4.467 V, it increases exponentially from 14 A/m to 607A/m .

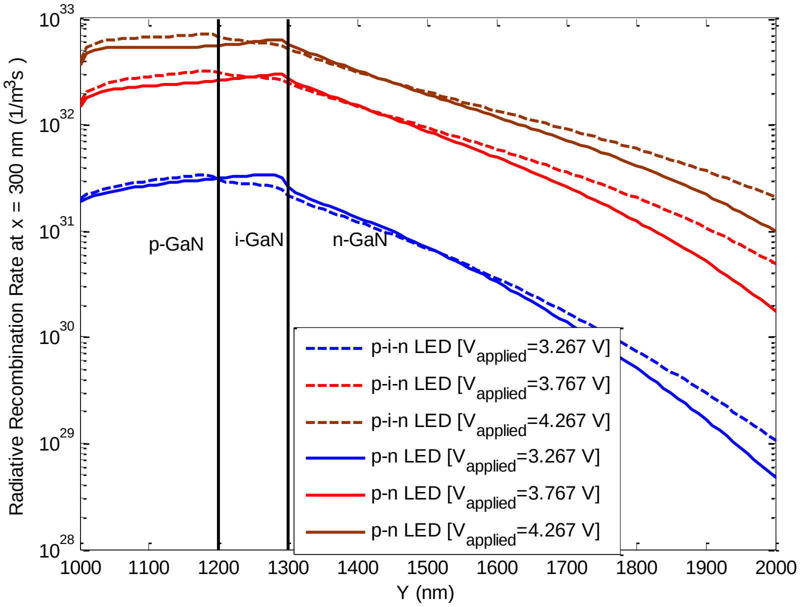

Figure 4.20 Radiative recombination rate at different applied voltages (p-n vs p-i-n GaN LEDs).

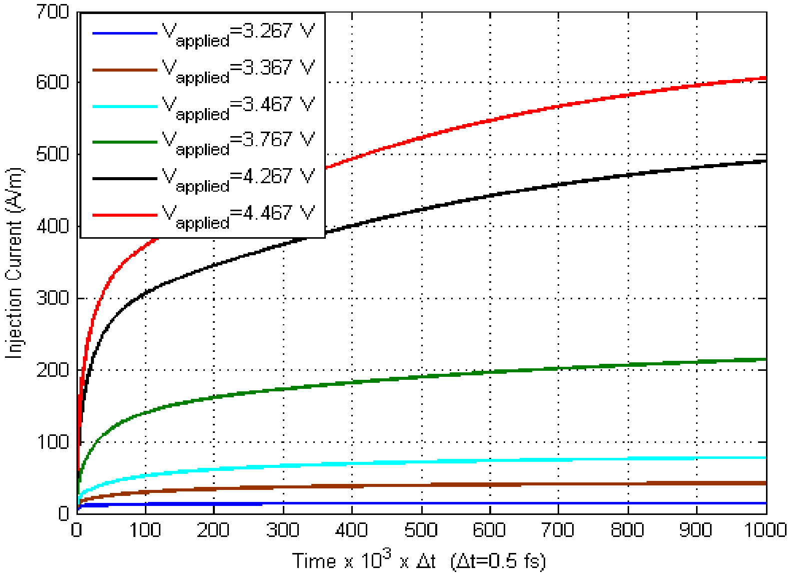

Figure 4.21 Injection current as a function of time (p-i-n GaN LED).

The current-voltage (I-V) characteristics curve of this LED structure is obtained from the steady state values of injection current- time curve and is shown in Figure 4.22.

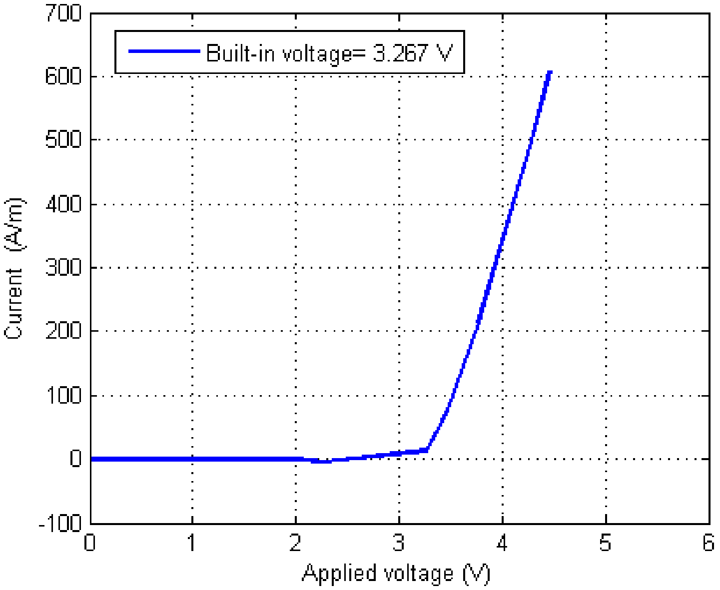

Figure 4.22 Current- voltage (I-V) characteristics of p-i-n GaN LED.

4.5 Analysis of a basic P-AlGaN/ n-GaN/ N-AlGaN Double Heterojunction (DH) LED

As seen from the p-i-n LED, the active region where there are strong recombinations is increased with the addition of an intrinsic layer. With the same idea, the LED device performance can be further improved by increasing the active region and confining the carriers inside the active region. This can be achieved by using heterojunctions i.e. materials with different energy bandgaps. The carrier confinement inside the LED active region can be enhanced with the introduction of a narrow bandgap material between two wide bandgap materials. Therefore, we numerically analyze a P-AlGaN/n-GaN/N-AlGaN DH LED structure that consists of a 100 nm $n-GaN$ narrow bandgap layer doped at

$10^{17} cm^{-3}$ sandwiched between $200\, nm$ thick $P-Al_{0.3}Ga_{0.7}N$ and $1\mu m$ thick $N-Al_{0.3}Ga_{0.7}N$ wide bandgap layers doped at $10^{17}\, cm^{-3}$ as shown in Figure 4.23. The parameter values used in simulation are given in Table 4.2 and Table 4.3.

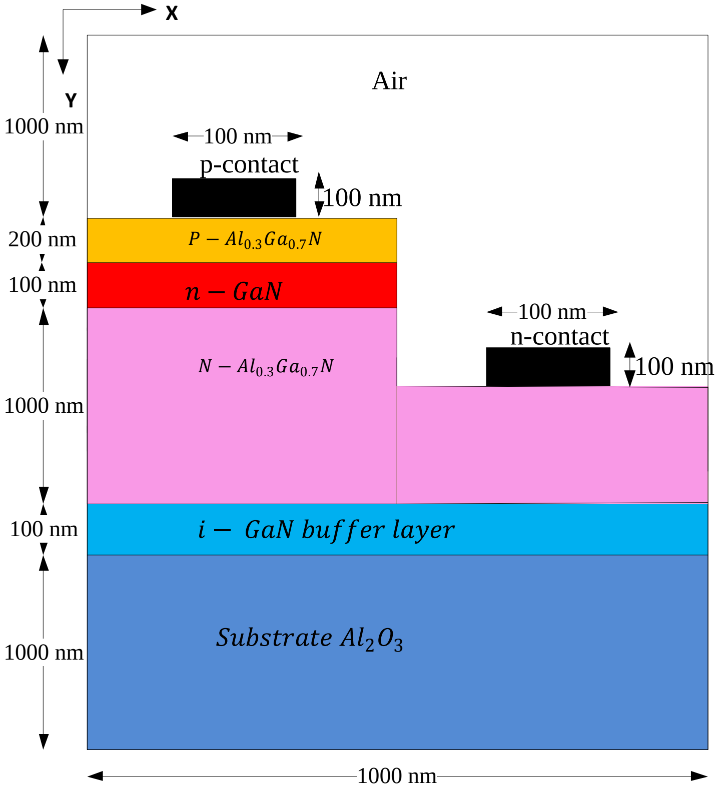

Figure 4.23 Schematic of P-AlGaN/ n- GaN/ N-AlGaN DH LED.

4.5.1 Energy Bands, Recombination Rates and Injection currents

The conduction band and valence band edges of two different bandgap materials are at different energy levels. The conduction band edge and valence band edge alignment of a double heterojunction structure i.e. $P-Al_{0.3}Ga_{0.7}N/n-\ GaN$ heterojunction and $n-GaN/\ N-Al_{0.3}Ga_{0.7}N$ is decided by the electron affinity rule. According to the electron affinity rule, the conduction band offset ΔE_c at the heterojunction interface is given by

$$\Delta E_c = q(\chi_1 - \chi_2) \tag{4.10}$$

$$\Delta E_v = E_{g1} - E_{g2} - \Delta E_c = \Delta E_g - \Delta E_c \tag{4.11}$$

Table 4.3 Parameter values used in the simulation of AlGaN/ GaN DH LED ([36], [39], [60], [61]).

Parameter	**Value**
Energy Bandgap of $Al_{0.3}Ga_{0.7}N$ $E_g[eV]$	4.06
Low field electron mobility of $Al_{0.3}Ga_{0.7}N$ at $N = 10^{17} cm^{-3}$ $\mu_{no}[cm^{-2}V^{-1}s^{-1}]$	843
Dielectric constant of $Al_{0.3}Ga_{0.7}N$ (ε_r)	9.61
Conduction band offset between $Al_{0.3}Ga_{0.7}N$ and GaN heterojunction ΔE_c $[eV]$	0.36
Richardson coefficient (electrons) A_n^* $[Acm^{-2}K^{-2}]$	24
Richardson coefficient (holes) A_p^* $[Acm^{-2}K^{-2}]$	132
Sheet charge density at ($Al_{0.3}Ga_{0.7}N/GaN$ heterointerface) N_s $[cm^{-2}]$	1.327×10^{16}
Electron Affinity of GaN $q\chi$ [eV]	3.5
Electron Affinity of $Al_{0.3}Ga_{0.7}N$ $q\chi$ [eV]	3.14
Electron Effective mass of $Al_{0.3}Ga_{0.7}N/$ GaN m_n^*/m_0	0.20
Hole Effective mass of $Al_{0.3}Ga_{0.7}N/$ GaN m_p^*/m_0	1.1

The LED structure has two heterojunction interfaces i.e. a P-n heterojunction and an n-N heterojunction. The bandgap energies and electron affinities of P-n-N DH LED structure are shown in Figure 4.24. The built in voltage V_{bi} and depletion width edges y_p and y_n for P-n and n-N heterojunction are given by the following equations

$\boldsymbol{P - Al_{0.3}Ga_{0.7}N/n - GaN}$ Heterojunction

$$qV_{bi} = E_{g1} - \Delta E_c + k_B T ln\left(\frac{N_a N_d}{N_{c2} N_{v1}}\right) \tag{4.12}$$

$$y_p = \left[\frac{2}{q}\varepsilon_2\varepsilon_1 \frac{N_d}{N_a}\frac{V_{bi}}{(\varepsilon_1 N_a + \varepsilon_2 N_d)}\right]^{\frac{1}{2}} \tag{4.13}$$

$$y_n = \left[\frac{2}{q}\varepsilon_2\varepsilon_1 \frac{N_a}{N_d}\frac{V_{bi}}{(\varepsilon_1 N_a + \varepsilon_2 N_d)}\right]^{\frac{1}{2}} \tag{4.14}$$

where N_c and N_v are electrons and holes effective densities of states ($1 = P - Al_{0.3}Ga_{0.7}N$ and $2 = n - GaN$)

$\boldsymbol{n - GaN/N - Al_{0.3}Ga_{0.7}N}$ Heterojunction

$$qV_{bi} = \Delta E_c + k_B T ln\left(\frac{N_{d2} N_{c1}}{N_{d1} N_{c2}}\right) \tag{4.15}$$

$$y_n = \left[\frac{2}{q}\varepsilon_2\varepsilon_1 \frac{V_{bi}}{(\varepsilon_1 N_{d2} + \varepsilon_2 N_{d1})}\right]^{\frac{1}{2}} \tag{4.16}$$

($1 = n - GaN, 2 = N - Al_{0.3}Ga_{0.7}N$)

The energy band diagram for the DH LEDs is obtained from the electrostatic potential distribution, carrier concentrations n and p obtained by solving the drift diffusion equations with thermionic boundary conditions and are calculated using the following equations.

$$E_c = k_B T \ log\left(\frac{N_c}{n_i}\right) - qV - \chi \tag{4.17}$$

$$E_i = E_c - \frac{E_g}{2} \tag{4.18}$$

where the bandgap distribution and the electron affinity distribution χ along the device is given by Figure 4.24.

$$E_v = E_c - E_g \tag{4.19}$$

$$E_{fn} = E_i + k_B T \, log\left(\frac{n}{n_i}\right) \tag{4.20}$$

$$E_{fp} = E_i - k_B T \, log\left(\frac{p}{n_i}\right) \tag{4.21}$$

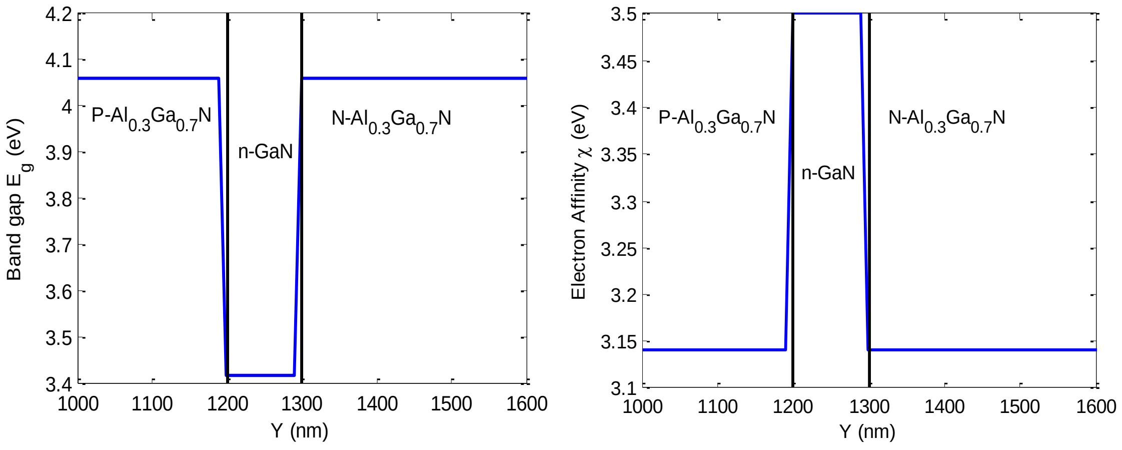

(a) **(b)**

Figure 4.24 (a) Bandgap energies, (b) Electron affinities of P-n-N DH GaN LED.

The carrier transport simulation of heterojunction LEDs requires incorporating the $Al_{0.3}Ga_{0.7}N/\,GaN$ material properties i.e. the band discontinuity at the heterointerface through the thermionic boundary conditions, the field dependent mobilities of $Al_{0.3}Ga_{0.7}N$, the fixed polarization charges at the heterointerface through polarization model discussed in chapter 2.

The Fermi levels at the heterojunction interface are discontinuous due to the conduction band offset between the two materials that lead to discontinuity in electron and hole currents. However, the drift diffusion model solves the current continuity equations assuming the continuity of Fermi levels at the junction. Therefore, appropriate changes have to be made for current to be continuous at the heterojunction. This can be achieved by using thermionic boundary conditions on current densities at the heterointerface [62], [63] . Therefore, the carrier transport in heterojunction LEDs is described by the drift diffusion model solved in the bulk regions and thermionic boundary conditions at the heterointerface.

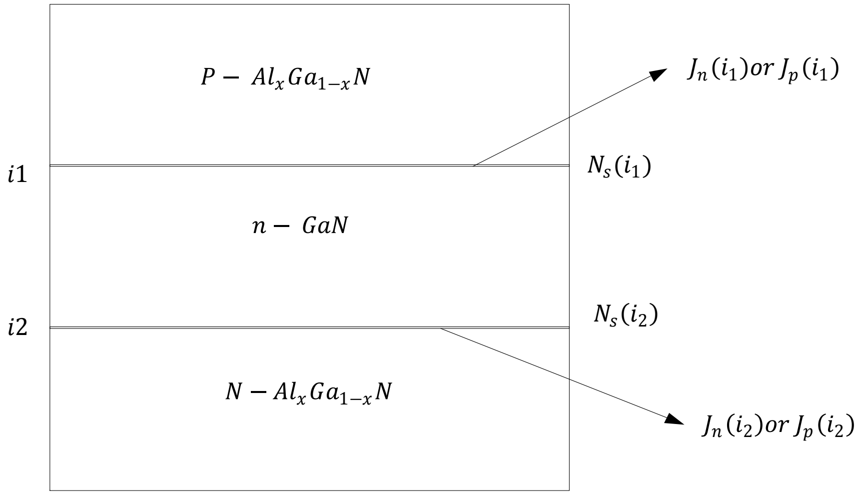

Figure 4.25 A simple P-n and n-N heterointerface, i_1 and i_2 are heterointerfaces.

The polarization surface charge density at the two heterointerfaces is calculated using the polarization model and is included in Poisson’s equation to incorporate the effect of built-in polarization charges at AlGaN/ GaN heterointerface as discussed in chapter 2.

Therefore, the surface charges densities $N_s(i_1)$, $N_s(i_2)$ and thermionic boundary conditions on electron and hole current densities $J_{n/p}(i_1)$ and $J_{n/p}(i_2)$ at $P-$

$Al_{0.3}Ga_{0.7}N/\ n-GaN$ and $n-GaN/\ N-Al_{0.3}Ga_{0.7}N$ heterointerfaces used in the simulation are calculated using the following expressions [39], [61]–[63]

$$N_s(i_1)=\frac{P^{total}_{Al_{0.3}Ga_{0.7}N}-P^{total}_{GaN}}{q}\times 10\%=-1.327\ \times 10^{16}\ cm^{-2} \tag{4.22}$$

$$N_s(i_2)=\frac{P^{total}_{GaN}-P^{total}_{Al_{0.3}Ga_{0.7}N}}{q}\times 10\%=+1.327\ \times 10^{16}\ cm^{-2} \tag{4.23}$$

$$J_n(i_1)=q\eta\vartheta_{nR}\left(n(i1-1)-\theta n(i1+1)\,exp\left(-\frac{\Delta E_c}{k_BT}\right)\right) \tag{4.24}$$

$$J_p(i_1)=q\eta\vartheta_{pR}\left(p(i1-1)-\theta p(i1+1)\,exp\left(-\frac{\Delta E_c}{k_BT}\right)\right) \tag{4.25}$$

$$J_n(i_2)=q\eta\vartheta_{nR}\left(n(i2+1)-\theta n(i2-1)\,exp\left(-\frac{\Delta E_c}{k_BT}\right)\right) \tag{4.26}$$

$$J_p(i_2)=q\eta\vartheta_{pR}\left(p(i2+1)-\theta p(i2-1)\,exp\left(-\frac{\Delta E_c}{k_BT}\right)\right) \tag{4.27}$$

where, $\vartheta_{nR}=A^*_nT^2/qN_c$ and $\vartheta_{pR}=A^*_pT^2/qN_v$ are electron and hole recombination velocities, A^*_n and A^*_p are electron and hole Richardson coefficients, respectively given in Table 4.3.η and θ are coefficients representing the effect of different effective masses and quantum mechanical transmission and reflections at the heterointerface. The case of η =θ=1 is for same effective mass of GaN and $Al_{0.3}Ga_{0.7}N$. ΔE_c is the conduction band offset between AlGaN/ GaN layers, n and p are electron and hole concentrations, respectively.

The discontinuity in the conduction band and valence band energies can be seen in Figure 4.26 and Figure 4.27 at the two heterointerfaces. It can be observed in Figure 4.27 that the carriers inside the GaN layer are at low energy levels compared to that of $AlGaN$ layers. Therefore, with such band alignment, we can confine the carriers inside the active region of GaN LED.

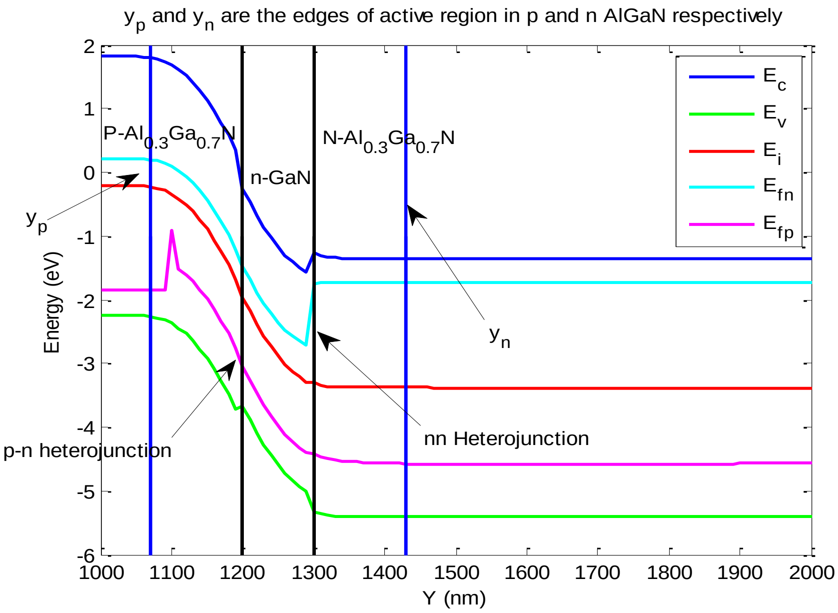

Figure 4.26 Energy band diagram of P-n-N DH GaN LED at zero applied voltage.

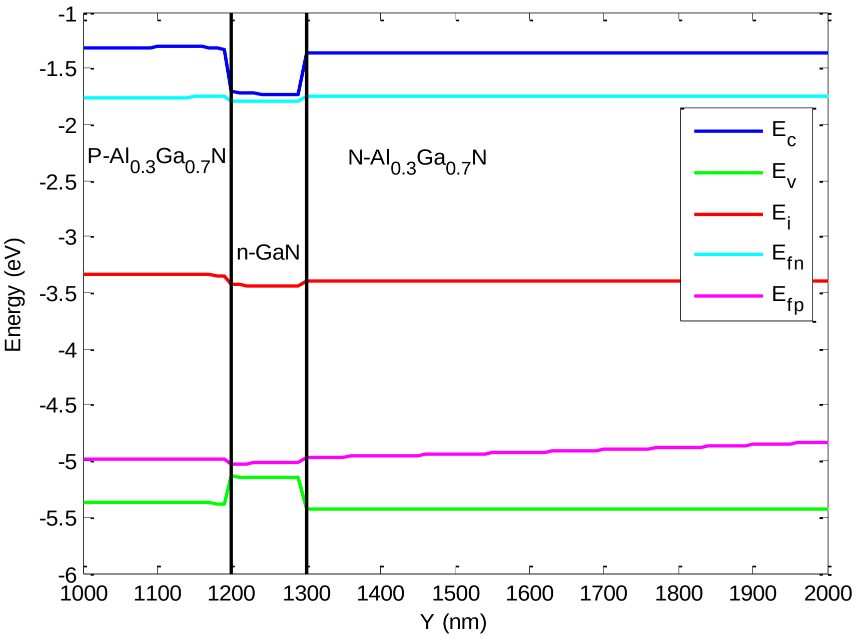

Figure 4.27 Energy band diagram of P-n-N DH GaN LED in forward bias.

The injected current- time curve at different bias and at different band offsets ΔE_c is shown in Figure 4.28 and Figure 4.29. The effect of ΔE_c is demonstrated on injection currents in Figure 4.29. The increase in the injection currents with increasing ΔE_c is observed due to the fact that the net built-in voltage across the DH LED decreases with increasing ΔE_c.

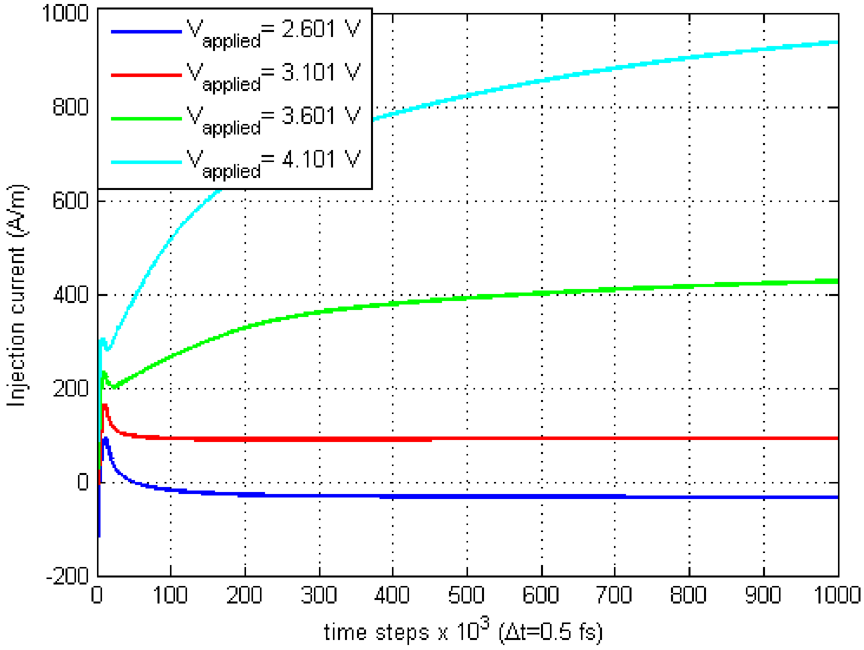

Figure 4.28 Injection current as a function of time (AlGaN/ GaN DH LED).

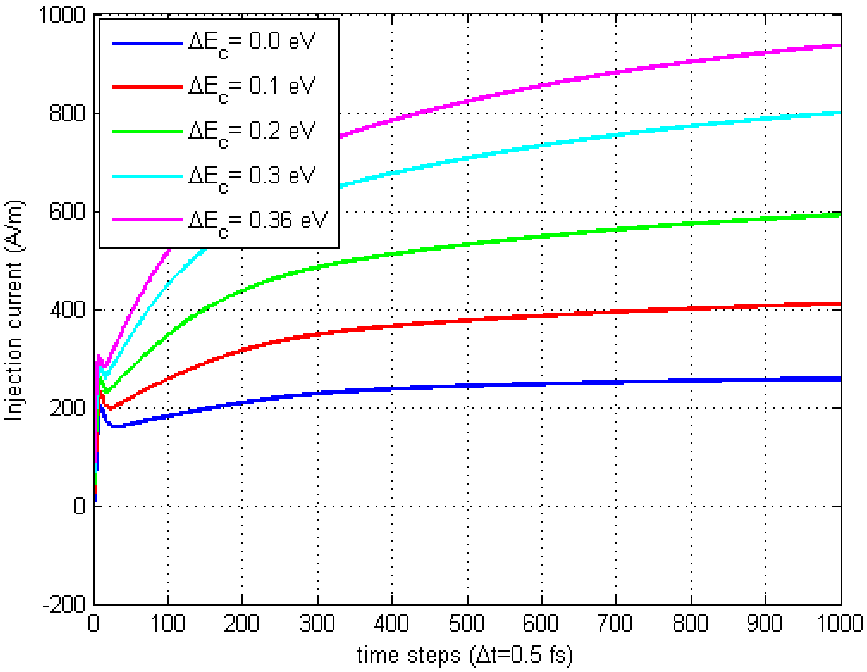

Figure 4.29 Injection current of AlGaN/ GaN DH LED at different band offsets ΔE_c.

The effect of bandgap offset ΔE_c is also seen on the radiative recombination rates shown in Figure 4.30. High values of band offset imply a high difference in the bandgap at the heterojunction that leads to more carrier confinement in the lower bandgap material. Therefore, the recombination rates increase at high values of ΔE_c. The effect of polarization charges at the heterointerface can also be seen in Figure 4.30. It tends to reduce the radiative recombinations at the heterointerface because of charge screening at the heterointerface due to presence of the built- in polarization fields.

The radiative recombination rates of a DH LED are also compared with that of homojunction LEDs as shown in Figure 4.31. It is evident that the effective area of the recombination rates is high for a DH LED than homojunction LED at same applied potential because of the carrier confinement with such band alignment in the CB and VB (Figure 4.27).

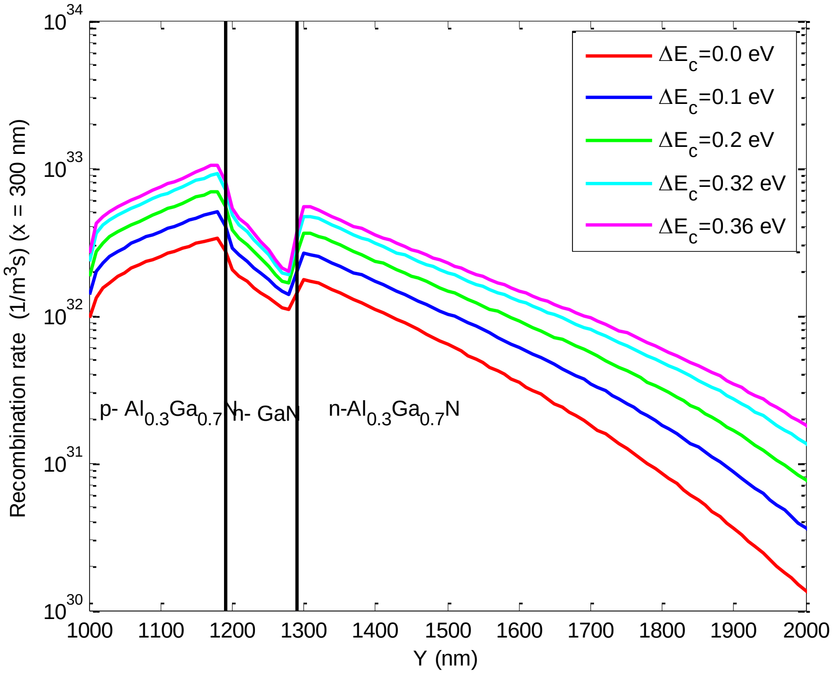

Figure 4.30 Radiative recombination rates of P-n-N DH GaN LED at different band offsets ΔE_c($V_{applied}$=4.101V).

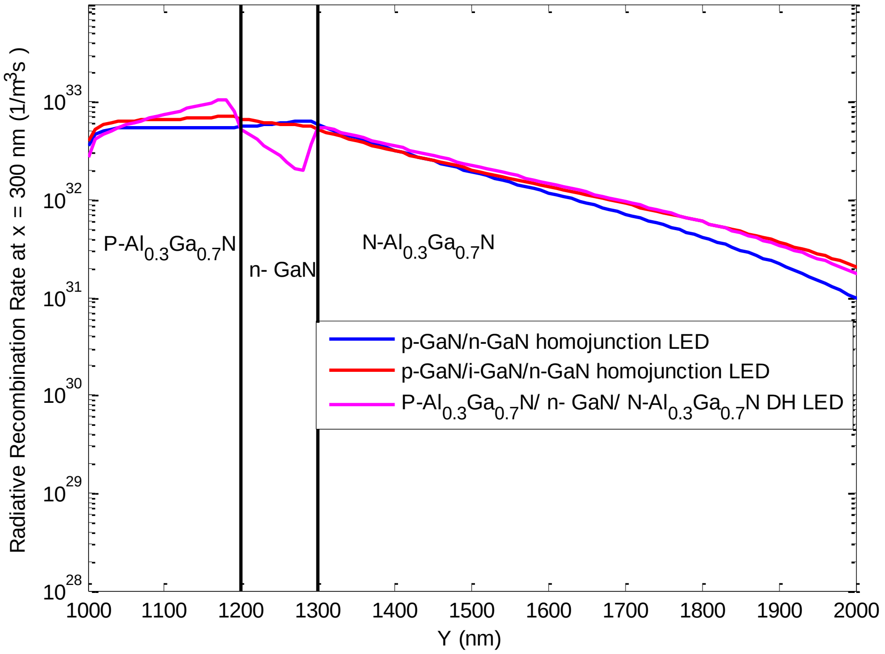

Figure 4.31 Radiative recombination rates: DH GaN LED vs. Homojunction GaN LEDs.

The current-voltage (I-V) characteristics of P-n-N DH GaN LED are shown in Figure 4.32 and are compared with that of a p-i-n GaN LED. The LED forward voltage is V_r is

$3.101\,V$ at an injection current of $91.1\,A/m$. The difference in the output currents between the three LEDs results from the differences in the radiative recombination rates. For example, the high radiative recombinations in the p-i-n LED decreases the output current as compared to p-n LED at same applied potential.

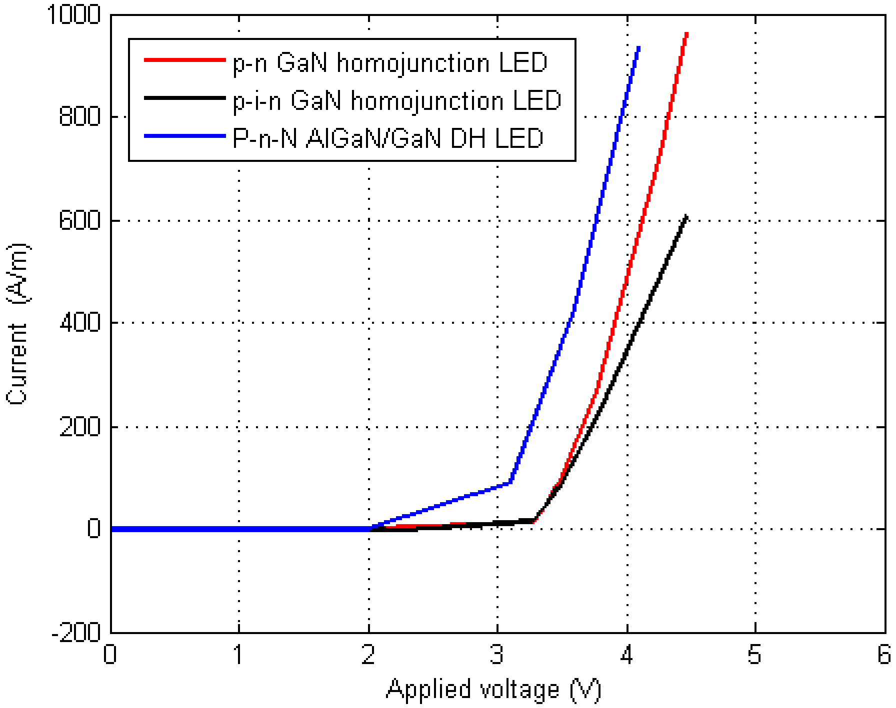

Figure 4.32 Current- voltage (I-V) characteristics P-n-N DH GaN LED vs. homojunction GaN LEDs.

4.5.2 Effect of dislocation densities on recombination rates and injection currents

The dislocations in III-Nitride materials that occur during material growth are due to the lattice mismatch or defects between the layers. The strength of the non-radiative recombinations is directly proportional to these dislocations. This can be elucidated from Figure 4.33 that shows the non-radiative lifetimes with dislocations. With high dislocations, the non-radiative lifetimes tend to decrease i.e. the non-radiative SRH recombinations are faster. Therefore, this effect of dislocations is demonstrated in Figure 4.34 and Figure 4.35 on recombination rates and injection currents respectively. The non-radiative SRH recombinations increase with dislocation densities whereas, the radiative recombinations decrease at a slow rate compared to SRH recombinations.

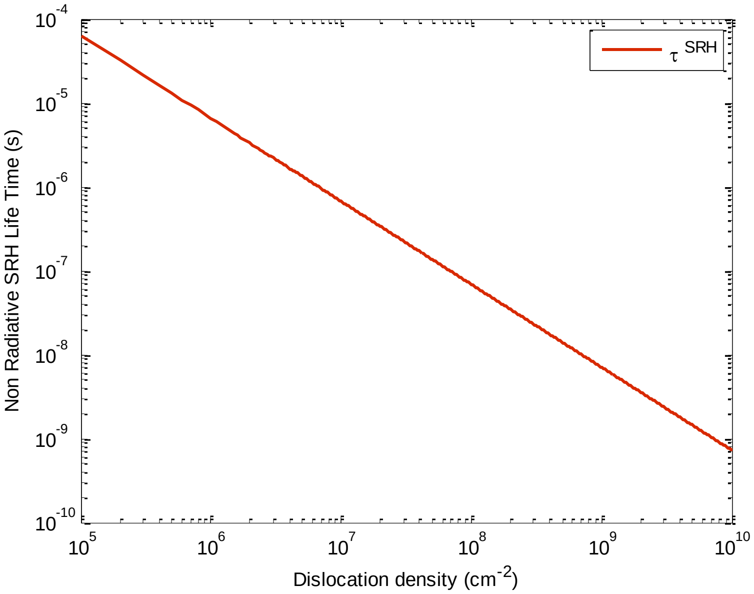

Figure 4.33 Non- radiative lifetime dependence on dislocation density ($N_{dislocation}$).

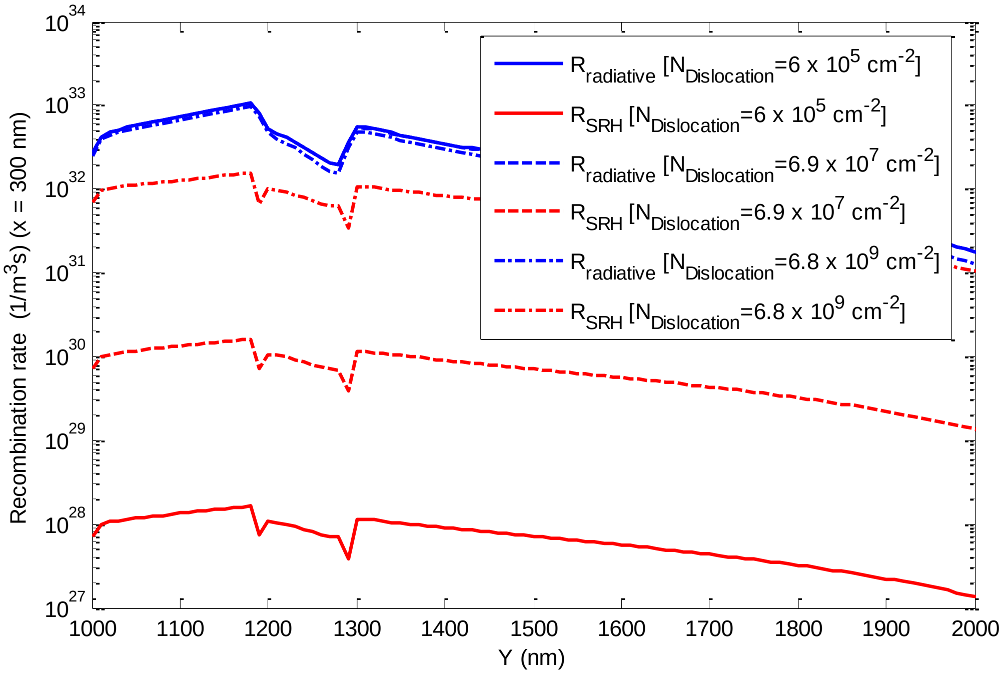

Figure 4.34 Effect of dislocations on Radiative and non-radiative recombination rates in GaN DH LED.

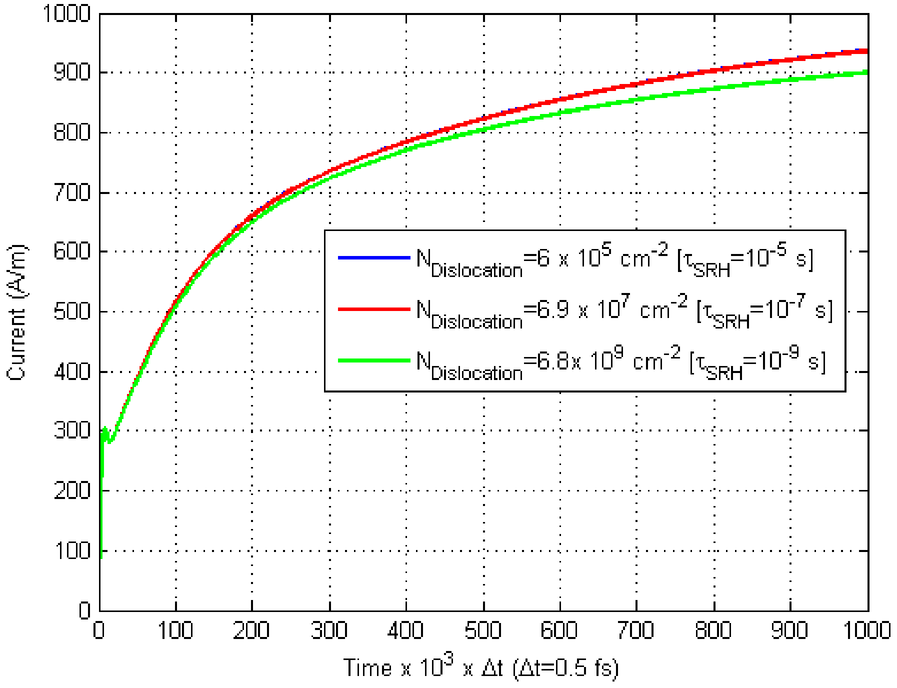

Figure 4.35 Effect of dislocations on Injection currents in GaN DH LED.

4.5.3 Effect of radiative recombination coefficient $B_{radiative}$ on electron-hole pair recombinations

Similar tests are carried with varying radiative recombination coefficient B or radiative lifetimes. A high value of coefficient B corresponds to low radiative lifetimes. Therefore, with decreasing B, the radiative lifetimes increases and hence the radiative recombinations occur at a slower rate. This can be seen from Figure 4.36, where the radiative recombination rates decrease with decreasing values of B. On the other hand, the injection currents increase at high values of B as shown in Figure 4.37 because of large number of carriers resulting from low recombinations at high B.

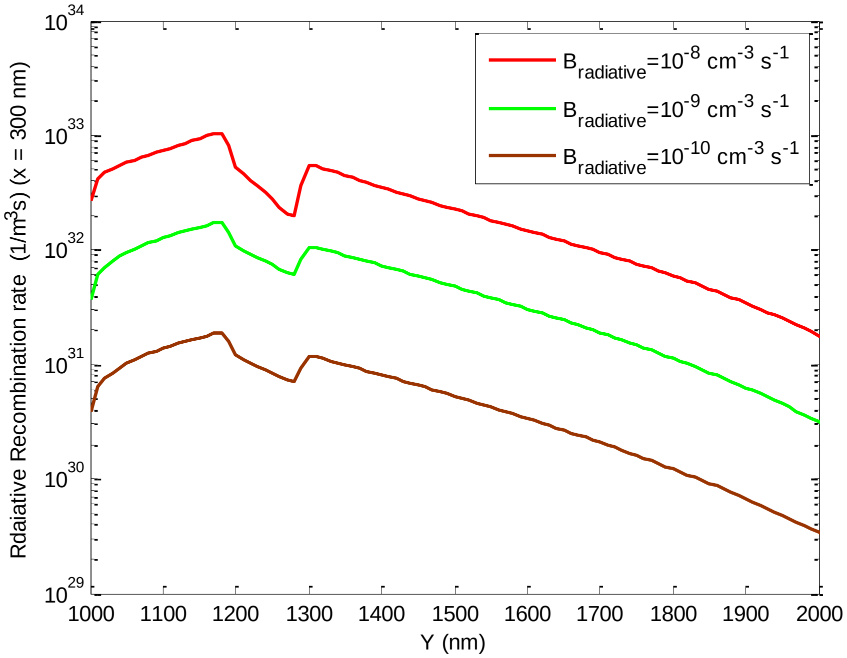

Figure 4.36 Radiative recombination rate with $B_{radiative}$ in GaN DH LED.

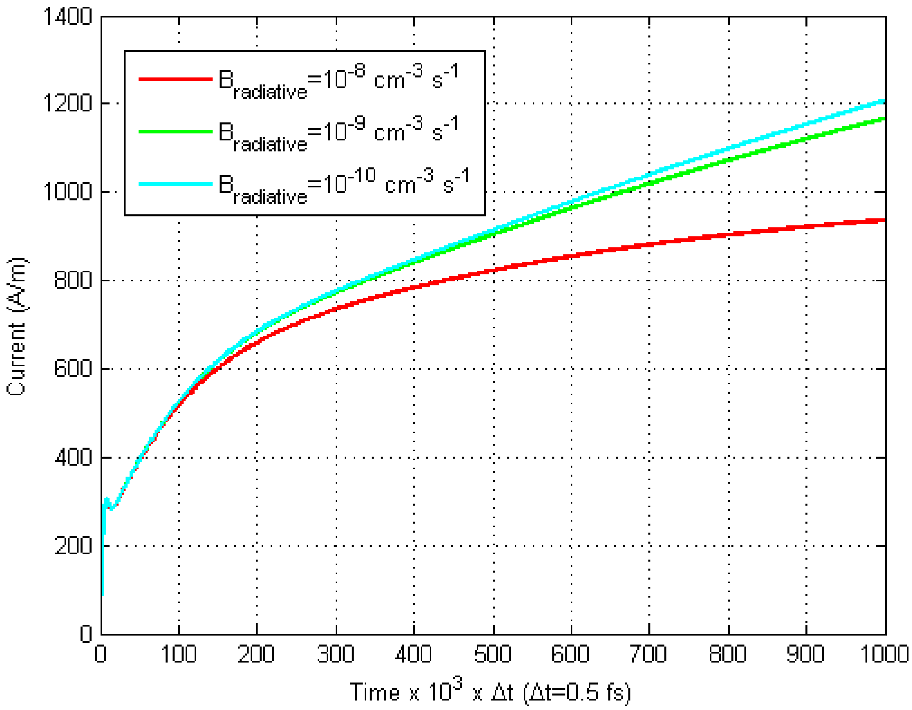

Figure 4.37 Injection current with $B_{radiative}$ in GaN DH LED.

4.6 P-AlGaN/ n-GaN/ N-AlGaN vs. P-AlGaN/ p-GaN/ N-AlGaN DH LED

The carrier transport in P-p-N DH LED is studied and compared with that of P-n-N DH LED. P-p-N DH LED is obtained by replacing the n-type active GaN layer with a p-type doped active GaN layer of same thickness. The difference in the radiative recombinations is due the shift in the p-n junction as shown in Figure 4.38. However, since the effective recombination area in the active region is approximately same, the injection currents for the two LEDs are equal as shown in Figure 4.39.

Next, asymmetric AlGaN/GaN DH LEDs i.e. AlGaN layers of different bandgaps on either side of GaN layer are tested to see the effect of asymmetry on the carrier transport.

The parameter values used in simulation of asymmetric DH LEDs are given in Table 4.2 and Table 4.4.

Table 4.4 Parameter values used in simulation of asymmetric AlGaN/ GaN DH LEDs ([32], [35], [56], [57])

Parameter	Value
Energy band gap of $Al_{0.4}Ga_{0.6}N/\ GaN\ E_g$ [eV]	4.312
Electron affinity of $Al_{0.4}Ga_{0.6}N\ \chi$ [eV]	3.01
Dielectric constant of $Al_{0.4}Ga_{0.6}N\ \varepsilon_r$	9.58
Conduction band offset at $Al_{0.4}Ga_{0.6}N/\ GaN$ interface ΔE_c [eV]	0.49
Valence band offset at $Al_{0.4}Ga_{0.6}N/\ GaN$ interface ΔE_v [eV]	0.40

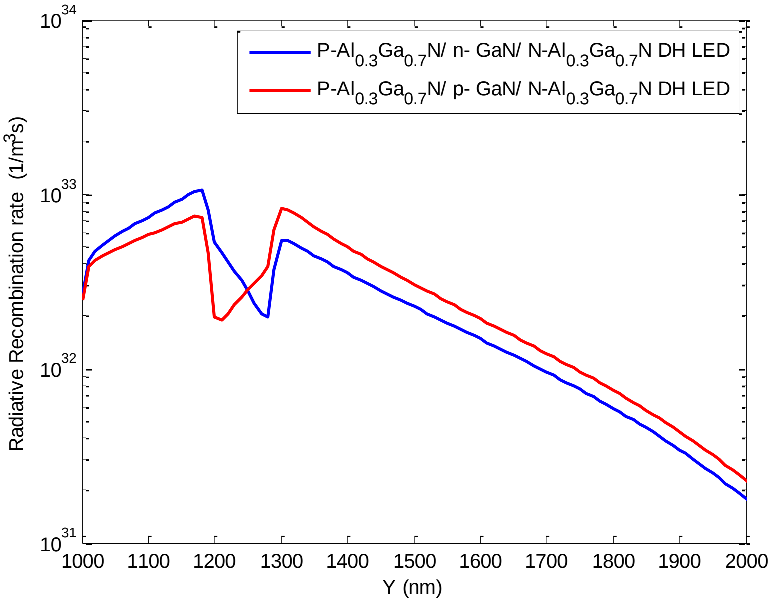

Figure 4.38 Radiative recombination rates: P-n-N vs. P-p-N AlGaN/ GaN DH LED.

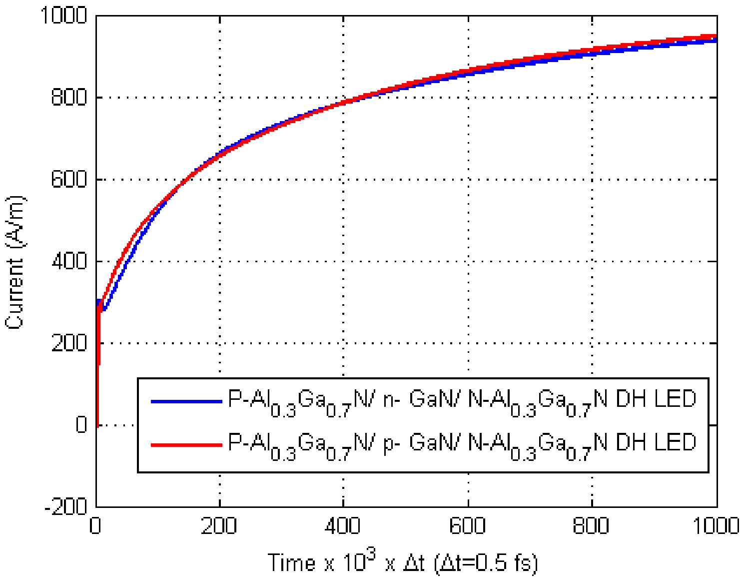

Figure 4.39 Injection currents: P-n-N vs. P-p-N AlGaN/ GaN DH LED.

The asymmetry in the conduction band and valence band offsets can be seen from energy band diagrams shown in Figure 4.40 and Figure 4.41. This asymmetry arises due to the difference in the energy bandgaps and electron affinities of AlGaN layers present on the either side of GaN layer.

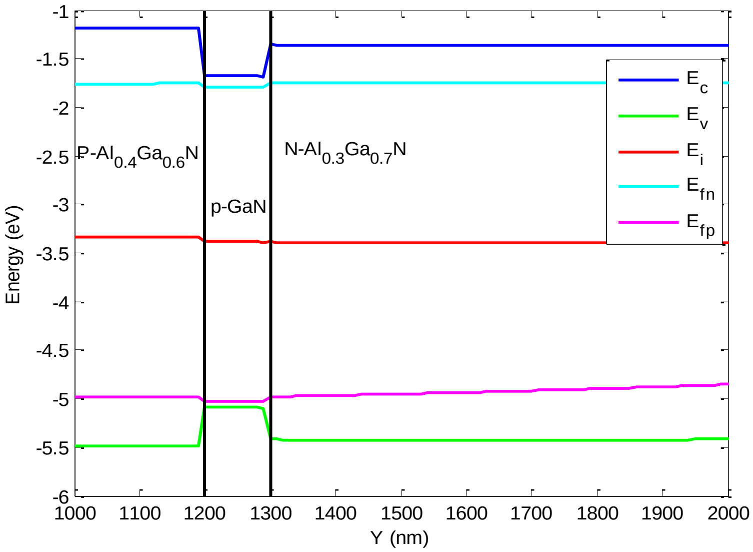

Figure 4.40 Energy band diagram of P-$Al_{0.4}Ga_{0.6}$N/p-GaN/N-$Al_{0.3}Ga_{0.7}$N DH LED at forward bias.

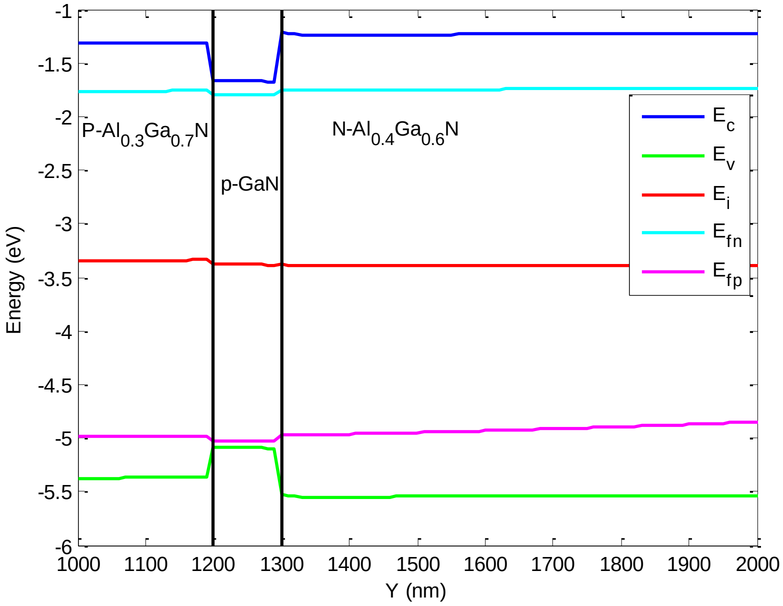

Figure 4.41 Energy band diagram of P-$Al_{0.3}Ga_{0.7}N$/p-GaN/N-$Al_{0.4}Ga_{0.6}N$ DH LED at forward bias.

The radiative recombination rates and injection currents are compared at same applied potential for the symmetric and asymmetric cases. It can be seen that the radiative recombinations and injection currents increases for the case where conduction band offset at P-p heterojunction is increased or is decreased at p-N heterojunction and vice versa. This increase with high band offset at P-p heterojunction i.e. $P - Al_{0.4}Ga_{0.6}N/\, p - GaN$ is due to the high probability of minority carriers in the active region as compared to that of $P - Al_{0.3}Ga_{0.7}N/\, p - GaN$ heterojunction.

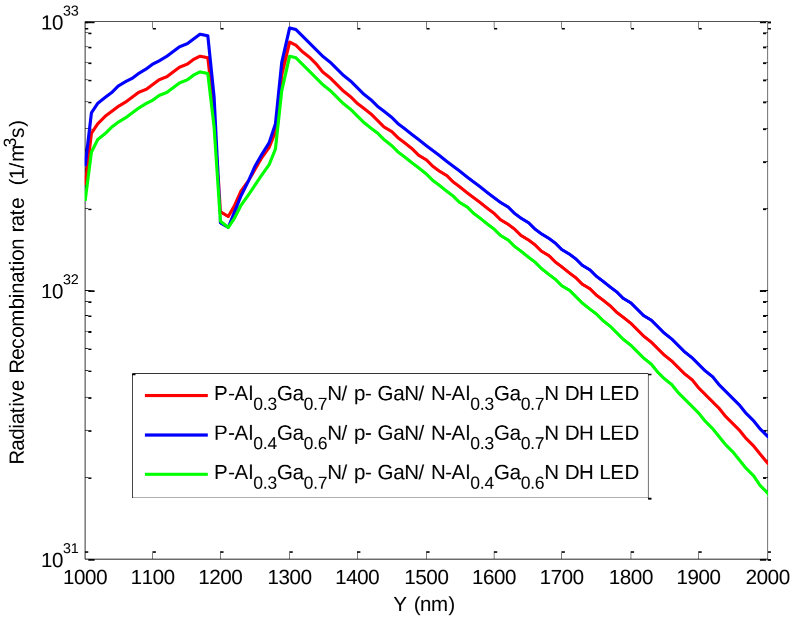

Figure 4.42 Radiative recombination rates: Symmetric and asymmetric P-p-n DH GaN LEDs.

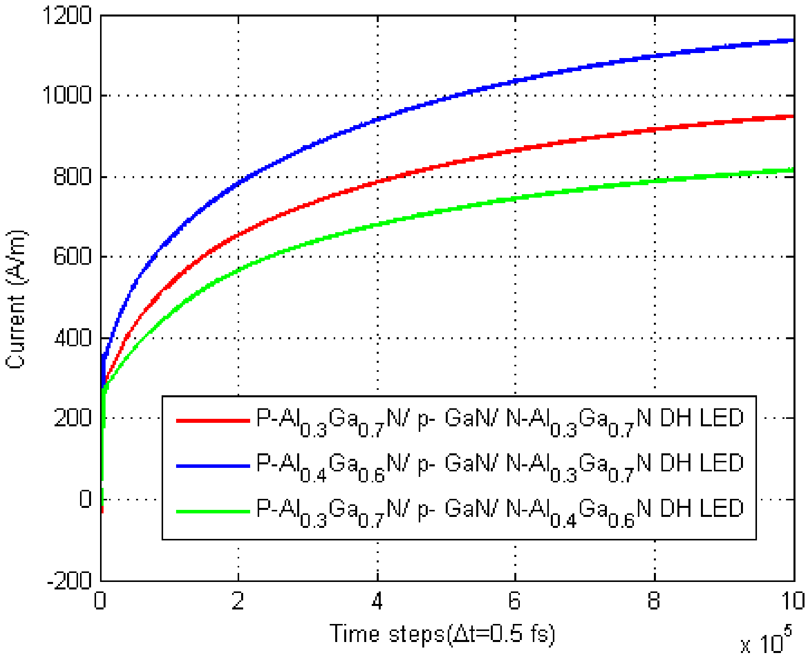

Figure 4.43 Injection currents: Symmetric and asymmetric P-p-n DH GaN LEDs.

4.7 Summary and Discussion

Homojunction and heterojunction GaN LEDs have been analyzed using the time domain FDTD-DD algorithm for carrier transport. The following observations were made:

- Injection currents decrease in the presence of FDM and RM.
- It is seen that the radiative recombination rates and injection currents for all the three LED structures considered increases with the applied voltage.
- DH LEDs demonstrated high recombination rates as compared to p-i-n and p-n homojunction GaN LED. This increase in the recombination rates of DH LED depend on the conduction band offset or band alignment of the materials. Radiative recombination rates of DH LED are almost doubled as compared to homojunction LEDs.
- The non-radiative recombinations were found to increase with increasing defects or dislocations, whereas the radiative recombinations increase with the increase in the radiative recombination coefficient.
- Symmetric and asymmetric P-p-N DH LEDs were also demonstrated and have been compared with P-n-N DH LED. The radiative recombination rates and injection currents of asymmetric DH LEDs either increases or decreases as compared to symmetric DH LEDs depending on asymmetry on P or N side respectively.

CHAPTER 5

OPTICAL SIMULATION OF GaN LEDs

5.1 Introduction

This chapter investigates the light propagation in GaN LED structures discussed in chapter 4 using the formulated optical model. The optical model based on Maxwell's equations is developed using the ADE-FDTD algorithm. The frequency dependent optical properties of dispersive materials used in these simulations i.e. GaN, AlGaN, silver, gold and aluminum are modeled using Lorentzian function and are incorporated in the ADE-FDTD algorithm.

5.2 Lorentzian fitting for dispersive materials

The optical properties of dispersive materials used in this thesis are modeled by a Lorentzian function that describes the relative permittivity in frequency domain. The general form of Lorentzian function is given as

$$\varepsilon(\omega) = \varepsilon_0\left(\varepsilon_\infty + \frac{\omega_p^2}{\omega_o^2 + j\Gamma\omega - \omega^2}\right) \tag{5.1}$$

The complex permittivity data of GaN and $Al_{0.3}Ga_{0.7}N$ have been fitted into a 5-pole Lorentz model as shown in Figure 5.1 and Figure 5.2. The Lorentzian function (equation (5.1)) for a multi- pole case can be re- written as

$$\varepsilon(\omega) = \varepsilon_0\left(\varepsilon_\infty + \sum_{i=1}^{N} \frac{a_i}{b_i + jc_i\omega - d_i\omega^2}\right), \tag{5.2}$$

$$\varepsilon\,(\omega) = \varepsilon_0(\varepsilon_{real}(\omega) - j\varepsilon_{imaginary}(\omega))$$

where, a_i, b_i, c_i, and d_i are fitting parameters.

Therefore, the real and imaginary values of complex permittivity are fitted in equations **(**5.3)-**(**5.4). The fitting parameters for both GaN and $Al_{0.3}Ga_{0.7}N$ are shown in Table 5.1 and Table 5.2.

$$\varepsilon_{real}(\omega) = \left(\varepsilon_\infty + \sum_{i=1}^{N} \frac{a_i(b_i - d_i\omega^2)}{(b_i - d_i\omega^2)^2 + (c_i\omega)^2}\right) \tag{5.3}$$

$$\varepsilon_{imaginary}(\omega) = \sum_{i=1}^{N} \frac{a_i c_i \omega}{(b_i - d_i\omega^2)^2 + (c_i\omega)^2} \tag{5.4}$$

The optical properties of gold and silver are modeled using a 6- pole Lorentz- Drude model. The frequency dependent relative permittivity of gold and silver are shown in Figure 5.4 and Figure 5.5, respectively. On the other hand, the optical properties of aluminum are modeled using 5-pole Lorentz-Drude model.

5.2.1 Gallium Nitride (GaN) complex permittivity

The complex permittivity data of GaN [41] is fit into 5- pole Lorentzian function as shown in Figure 5.1. The fitting parameters a, b, c and d are provided in Table 5.1.

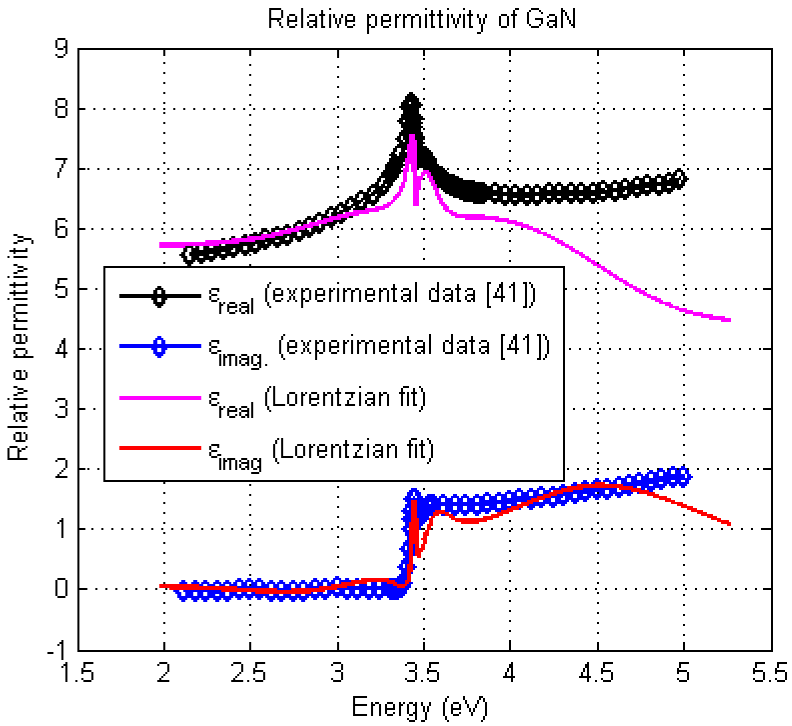

Figure 5.1 Relative permittivity of GaN (Lorentz fit (5 poles) and experimental data [41]).

Table 5.1 Fitting parameters for GaN relative permittivity (5-pole Lorentzian function).

Pole (i)	a	b	c	d
1	0.2×10^{30}	27.35×10^{30}	0.03×10^{15}	1.0
2	2.2×10^{30}	29.16×10^{30}	0.4×10^{15}	1.0
3	37×10^{30}	49×10^{30}	3×10^{15}	1.0
4	-4×10^{30}	20.25×10^{30}	2×10^{15}	1.0
5	-2×10^{30}	27.24×10^{30}	0.4×10^{15}	1.0

5.2.2 Aluminum Gallium Nitride ($Al_{0.3}$ $Ga_{0.7}N$) complex permittivity

Similarly, $Al_{0.3}$ $Ga_{0.7}N$ complex permittivity data [64] is fitted into 5-pole Lorentzian equation as shown in Figure 5.2. The fitting parameters a, b, c and d are listed in Table 5.2.

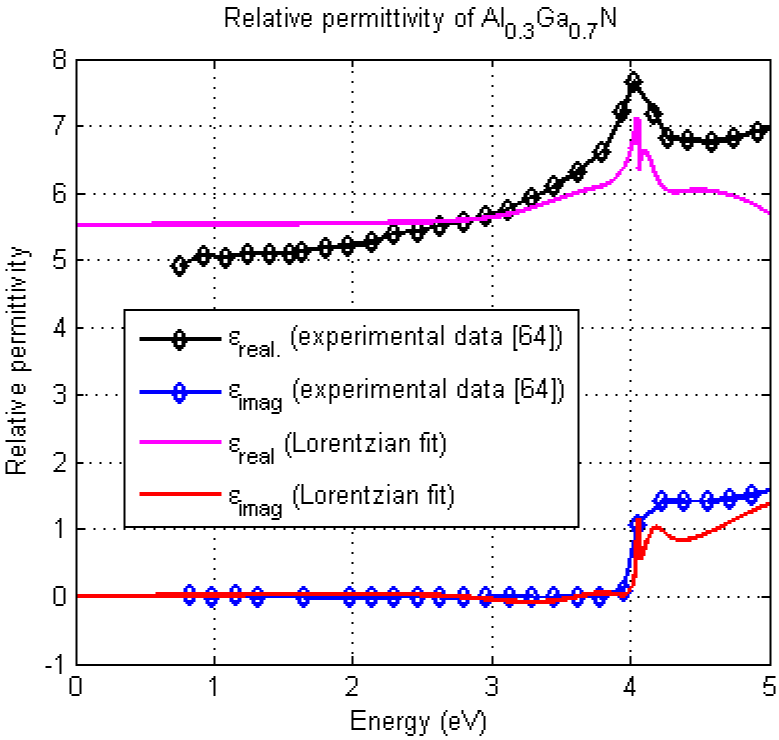

Figure 5.2 Relative permittivity of $Al_{0.3}Ga_{0.7}N$ (Lorentz fit (5 poles) and experimental data [64]).

Table 5.2 Fitting parameters for $Al_{0.3}Ga_{0.7}N$ relative permittivity (5-pole Lorentzian function).

Pole (i)	a	b	c	d
1	0.1×10^{30}	37.93×10^{30}	0.02×10^{15}	1.0
2	2.2×10^{30}	39.81×10^{30}	0.4×10^{15}	1.0
3	37×10^{30}	65.78×10^{30}	3×10^{15}	1.0
4	-4×10^{30}	28.09×10^{30}	2×10^{15}	1.0
5	-2×10^{30}	37.34×10^{30}	0.5×10^{15}	1.0

5.2.3 Aluminum (Al) complex permittivity

The complex permittivity data of Al is fitted into 5-pole Lorentz-Drude model with fitting parameters given in [65] and is shown in Figure 5.3. The Lorentz-Drude parameters are given in Table 5.3.

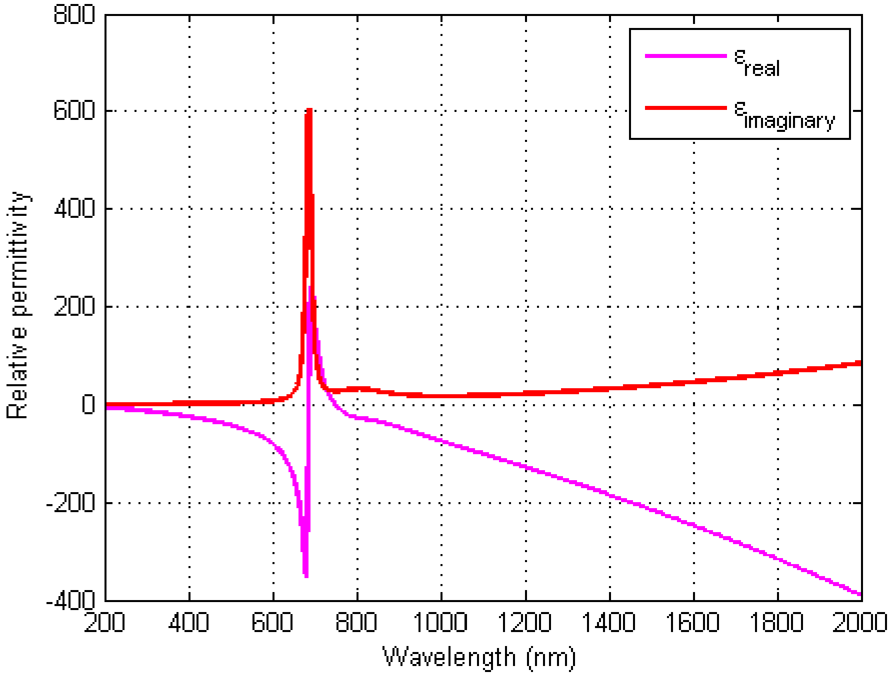

Figure 5.3 Aluminum (Au) relative permittivity (5-pole Lorentz-Drude model) ([65]).

Table 5.3 Fitting parameters for Aluminum (Al) relative permittivity (5-pole Lorentz-Drude model).

Pole (i)	a	b	c	d
1	2.708×10^{32}	0.0	7.14×10^{13}	1.0
2	1.176×10^{32}	6.057×10^{28}	5.059×10^{14}	1.0
3	2.589×10^{31}	5.502×10^{30}	4.74×10^{14}	1.0
4	8.598×10^{31}	7.545×10^{30}	5.253×10^{13}	1.0
5	1.553×10^{31}	2.784×10^{31}	5.138×10^{15}	1.0

5.2.4 Gold (Au) and Silver (Ag) complex permittivity

The complex permittivity data of Au and Ag is fitted into 6-pole Lorentz-Drude model [65] and is shown in Figure 5.4 and Figure 5.5.

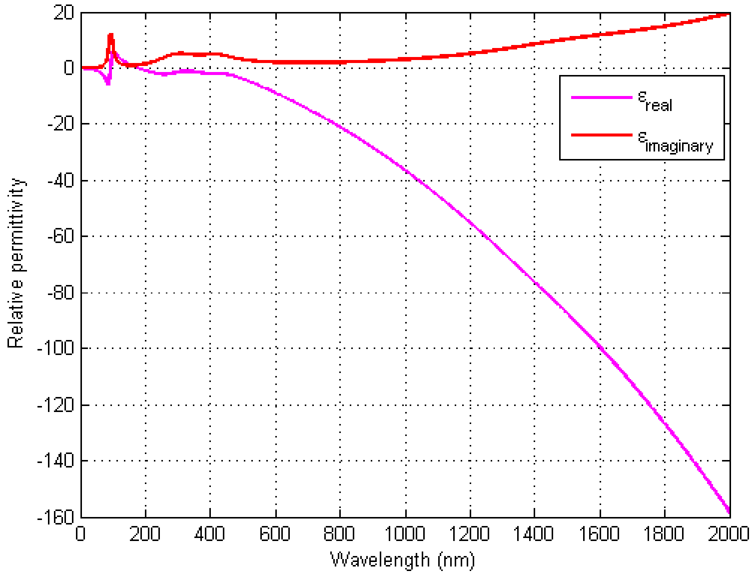

Figure 5.4 Gold (Au) relative permittivity (6-pole Lorentz-Drude model) ([65]).

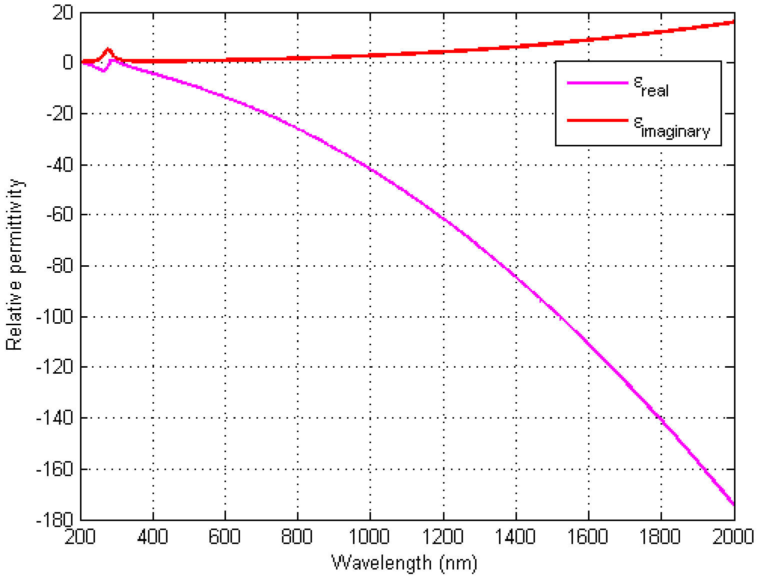

Figure 5.5 Silver (Ag) relative permittivity (6-pole Lorentz-Drude model) ([65]).

5.3 Optical simulation of GaN LEDs

In this section, the optical simulation of the homojunction and DH GaN LED structures is investigated using the ADE- FDTD algorithm. The material dispersion of GaN and AlGaN is incorporated in the FDTD algorithm using the five pole lorentzian function given in Table 5.1and Table 5.2. The effect of material dispersion on light propagation in GaN LEDs is investigated through these simulations. The light absorption due to dispersive behavior of the material is demonstrated through the optical generation rate and output optical power.

The optical carrier generation rate G is obtained from the absorbed optical power densities

$$G = \frac{Absorbed\ power}{Photon\ energy} = \frac{W}{E_{ph}} \tag{5.5}$$

where,

$\mathrm{W} = -\nabla.\mathrm{S}\,, \vec{S} = \vec{E} \times \vec{H}, S$ is the power density and $E_{ph} = \frac{hc_0}{\lambda}$ is the photon energy. (5.6)

For a 2D TM case, the generation rate is calculated as

$$G(x,y) = -\frac{-\nabla.S(x,y)}{E_{ph}} \quad , \overrightarrow{S} = \vec{E} \times \vec{H} = \left(E_y H_z\right)\overrightarrow{a_x} - (E_x H_z)\overrightarrow{a_y} \tag{5.7}$$

Thus, $\mathrm{G(x,y)}$ simplifies to

$$G(x,y) = -\frac{\left(\frac{\partial}{\partial x}(E_y H_z) - \frac{\partial}{\partial y}(E_x H_z)\right)}{E_{ph}} \tag{5.8}$$

For a 2D domain, the optical power is calculated by integrating the pointing vector over a line as follows

$$P = \int_{S1} S.\hat{n}\, dl = \int_{S1} (E \times H).\hat{n}\, dl \tag{5.9}$$

$$P_x = \int_{S1} (E_y H_z)\, dl \tag{5.10}$$

$$P_y = \int_{S1} (E_x H_z)\, dl \tag{5.11}$$

5.3.1 Inputs to the optical model

For the LED structures simulated using the proposed optical model, the input time source is a Gaussian pulse line source with a carrier wavelength of 365 nm, which corresponds to the emission wavelength of GaN LED. It is given by the following equation.

$$J_x(t) = J_y(t) = Aexp\left(-\left(\frac{t-t_0}{t_p}\right)^2\right)\cos\left(\frac{2\pi}{\lambda}t\right) \tag{5.12}$$

where $\lambda = 365\ nm$ (GaN emission frequency), $t_0 = 10\ fs$, $t_p = 30\ fs$

Therefore, the input source current densities J_x and J_y to be used in the FDTD algorithm to study light propagation inside a GaN LED structure are given by equation **(**5.12**)**. The source pulse in time domain and in wavelength domain is shown in Figure 5.6 and Figure 5.7 respectively. The FDTD simulation domain of both homojunction and DH LED structures is $1000\,nm \times 3400\,nm$ with spatial step $\Delta x = \Delta y = 10\,nm$ and time step $\Delta t = 0.021$ fs.

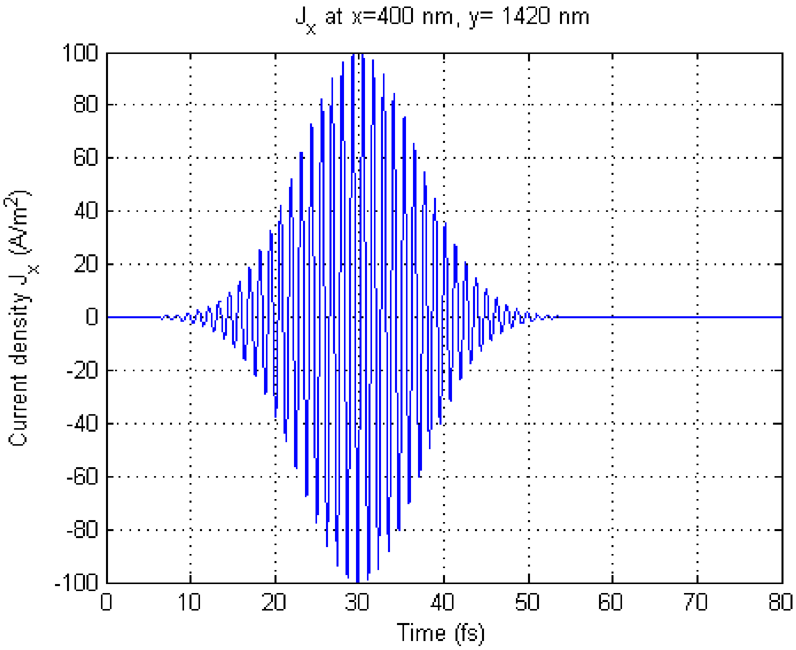

Figure 5.6 Input Gaussian pulse in the time domain.

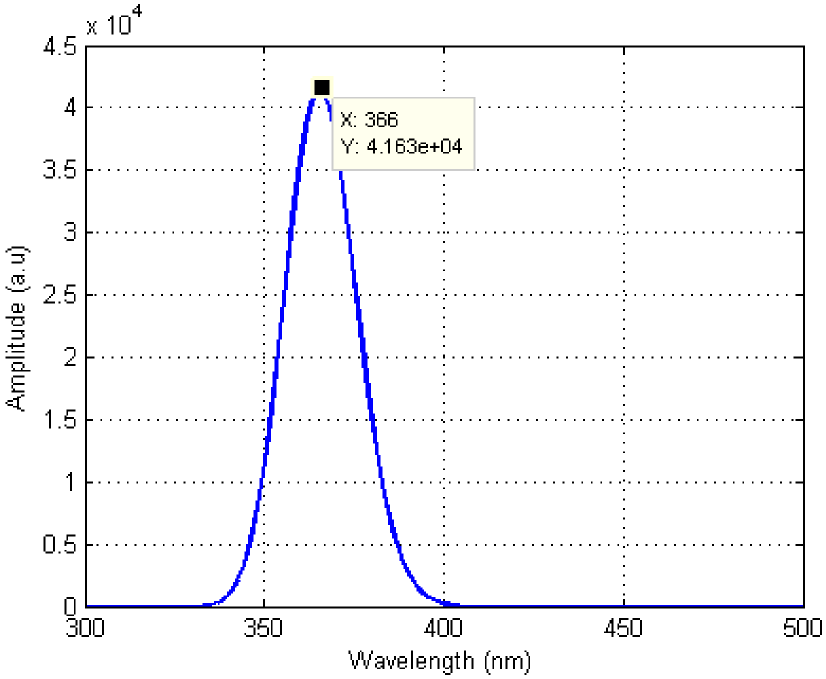

Figure 5.7 Input pulse in the frequency/ wavelength domain.

5.3.2 Optical simulation results of p-GaN/ n-GaN homojunction LED

The FDTD simulation domain of p-GaN/ n-GaN homojunction LED is shown in Figure 5.8. The structure is excited by a Gaussian pulse line source at the edge of the active region i.e. $y = 1420\ nm$ as shown in Figure 5.8.

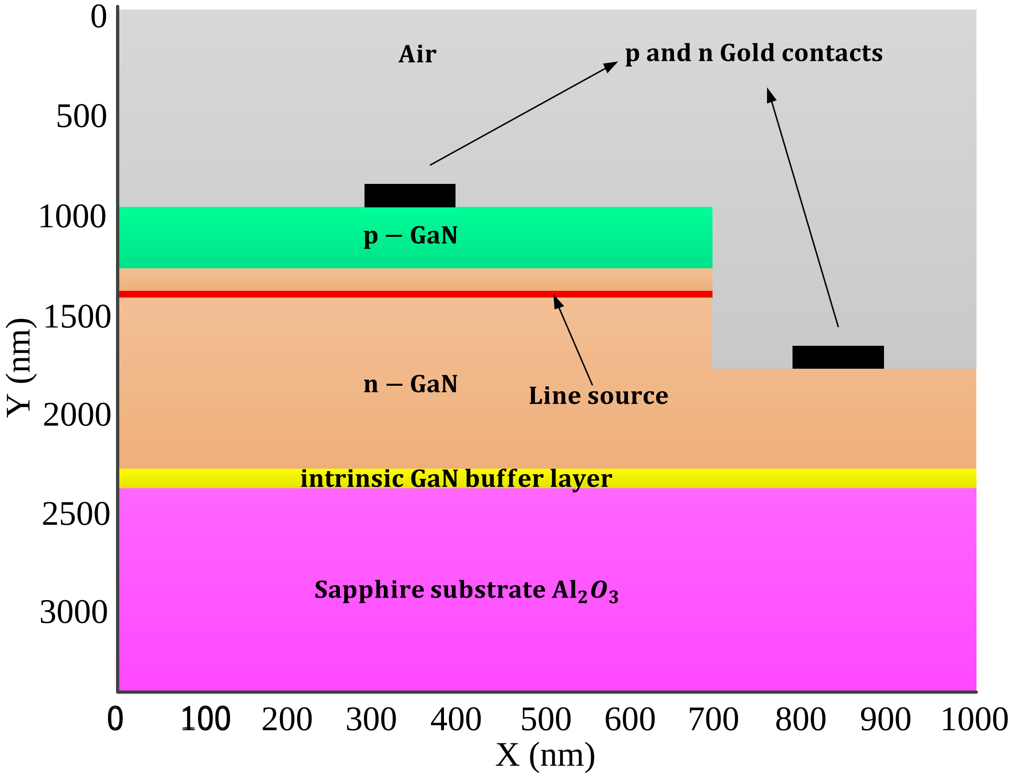

Figure 5.8 FDTD Simulation domain of p-n homojunction GaN LED.

The effect of GaN dispersion on EM fields propagating inside the LED structure is shown in Figure 5.9 to Figure 5.11. The difference in the strengths of the field intensities inside the GaN layers with and without dispersion effect can be seen from Figure 5.9 and Figure 5.10. The broadening and low amplitudes of magnetic field intensity measured in the air region with GaN dispersion as compared to no dispersion can be observed in Figure 5.11.

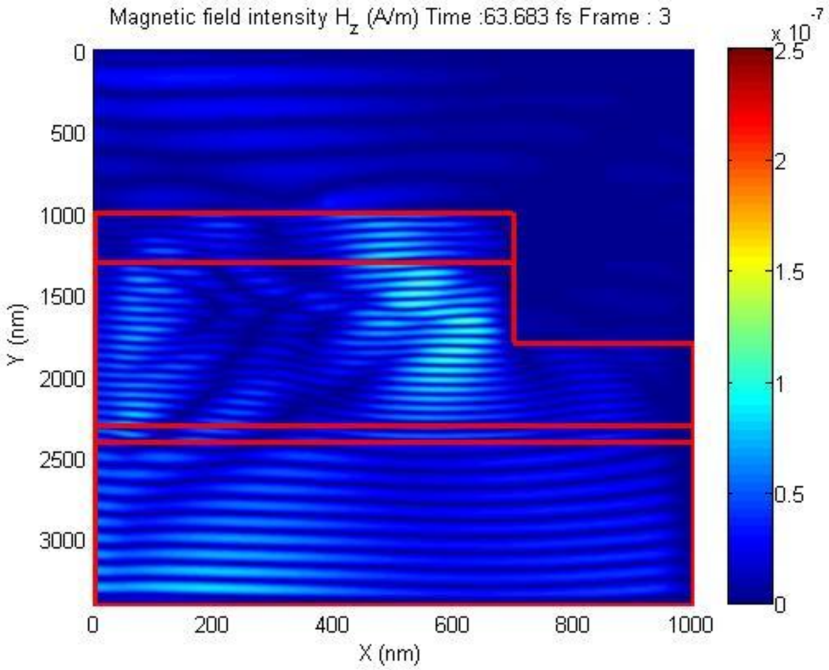

Figure 5.9 Snapshot of Magnetic field distribution- with GaN dispersion at time t=63.83 fs (p-n homojunction LED).

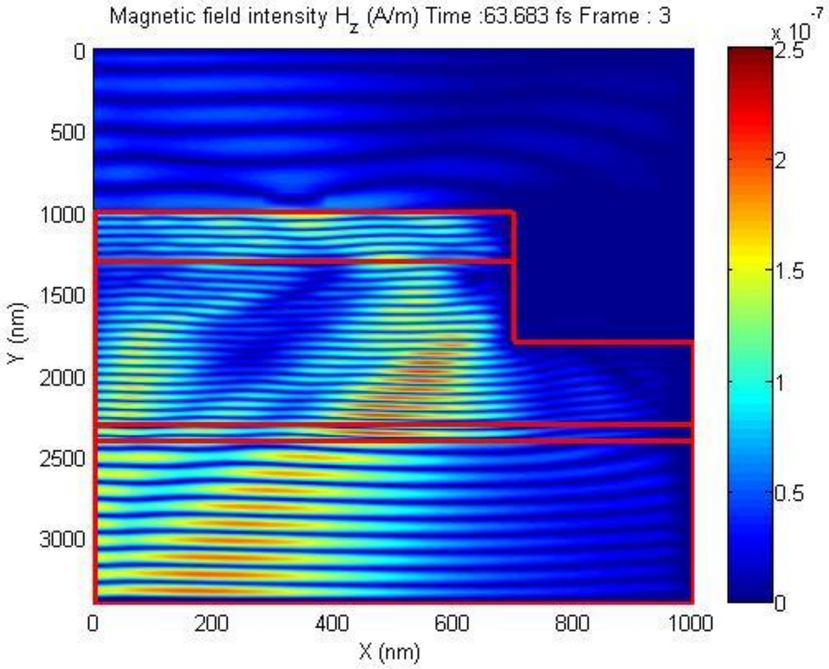

Figure 5.10 Snapshot of Magnetic field distribution- without GaN dispersion at time t=63.83 fs (p-n homojunction LED).

The dispersion effect is also demonstrated on the optical generation rates and optical power as shown in Figure 5.12 and Figure 5.13. It is evident from Figure 5.12 that the dispersion effect yields high optical generation rate that indicates high light absorption.

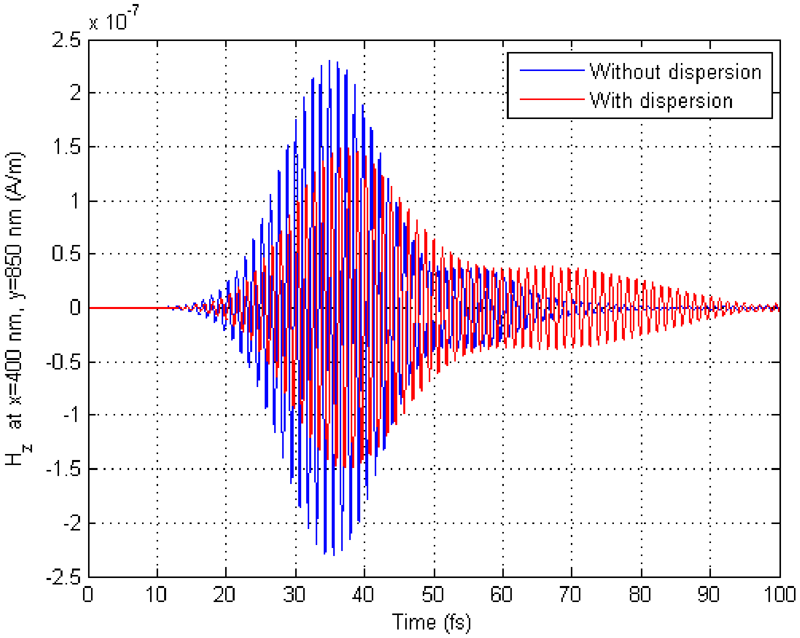

Figure 5.11 Magnetic field intensity measured in air region (p-n homojunction LED).

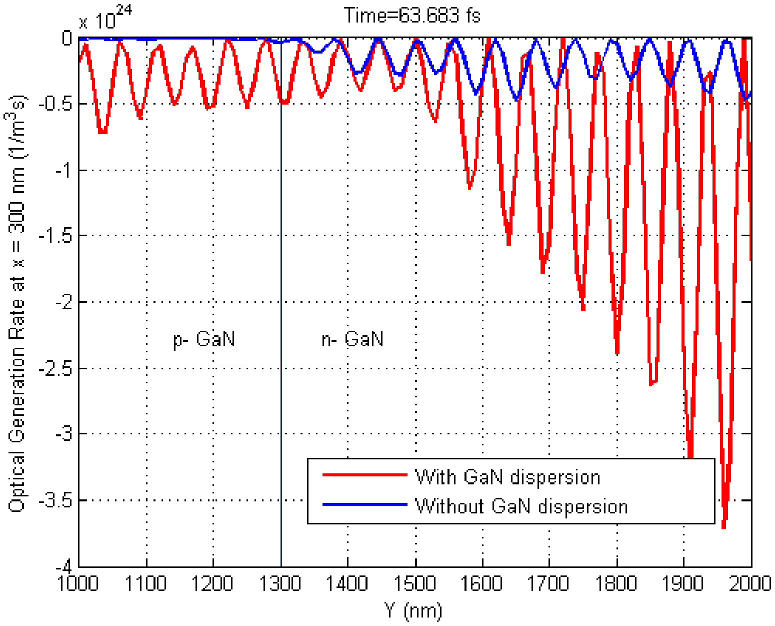

Figure 5.12 Optical Generation Rate along the width of p-n homojunction LED.

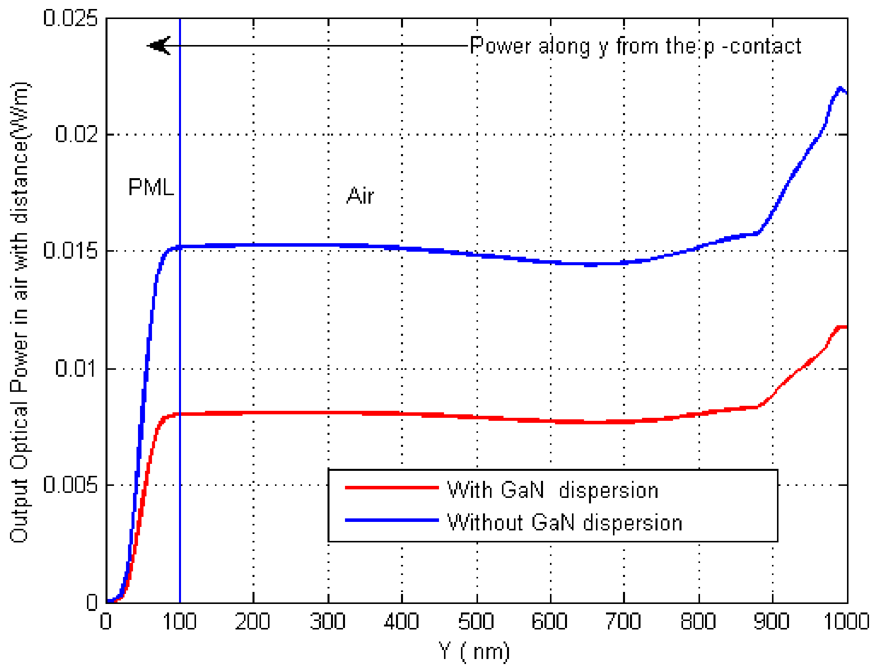

Figure 5.13 Output optical power measured in air region with distance Y (p-n homojunction LED).

5.3.3 Optical simulation results of P-AlGaN/ n-GaN/ N-AlGaN DH LED

To overcome the high light absorption in GaN layers at the emission wavelength 365 nm, the GaN layers are replaced with $Al_{0.3}Ga_{0.7}N$ layers except in the active region. It is well known that the imaginary part of dielectric permittivity accounts for light absorption losses as the light propagates in a material. It can be seen from Figure 5.1 and Figure 5.2 that $Al_{0.3}Ga_{0.7}N$ has low imaginary part of relative permittivity as compared to that of that of GaN at GaN emission energies. Therefore, the AlGaN layers improve both the electronic and optical performance of GaN LEDs through carrier confinement and low absorption.

Therefore, an AlGaN/ GaN DH LED structure analyzed in chapter 4 is investigated for light propagation using the optical model. Figure 5.14 shows the FDTD simulation domain of this LED structure. The input is a Gaussian pulse (Figure 5.6) line source located in the active GaN layer.

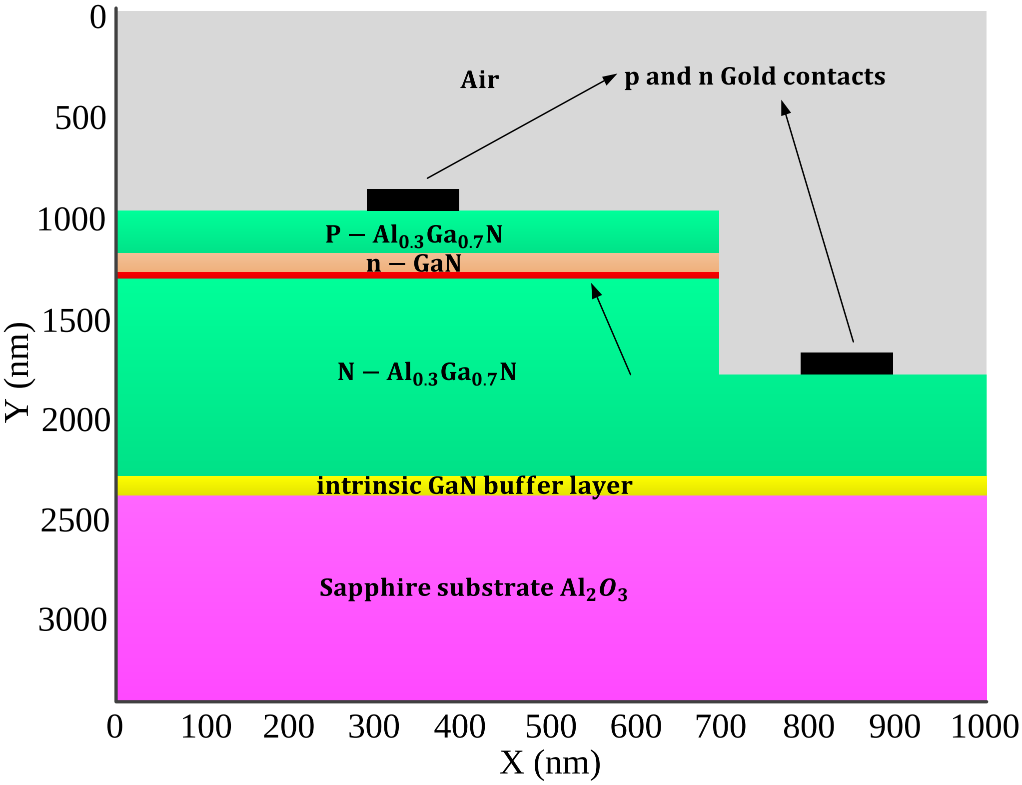

Figure 5.14 FDTD Simulation domain of P-n-N AlGaN/ GaN DH LED.

The dispersion effect of $Al_{0.3}Ga_{0.7}N$ and GaN layers on magnetic fields is shown in Figure 5.15 and Figure 5.16. The fields inside these layers undergo dispersion as they propagate which is also clear from Figure 5.17.

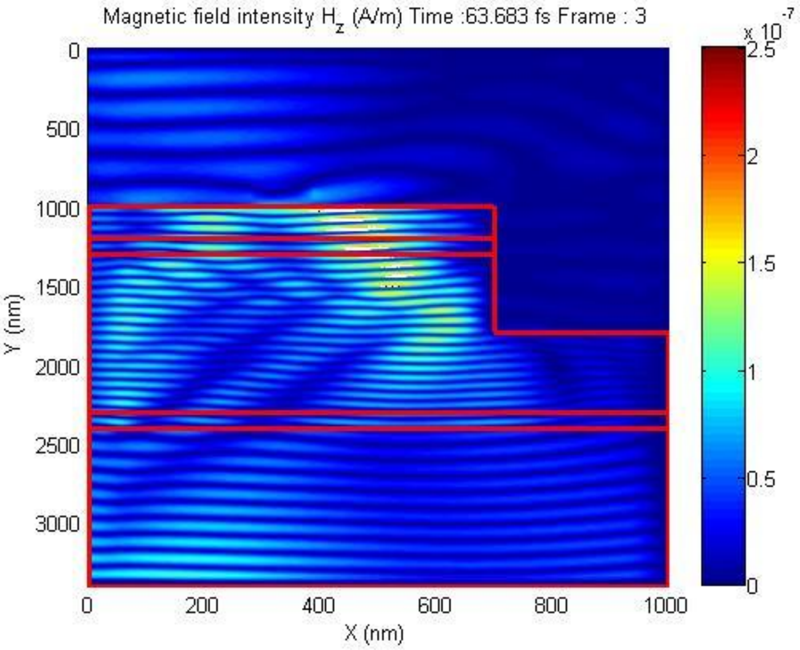

Figure 5.15 Snapshot of Magnetic field distribution- with GaN dispersion at time t=63.83 fs (P-n-N AlGaN/ GaN DH LED).

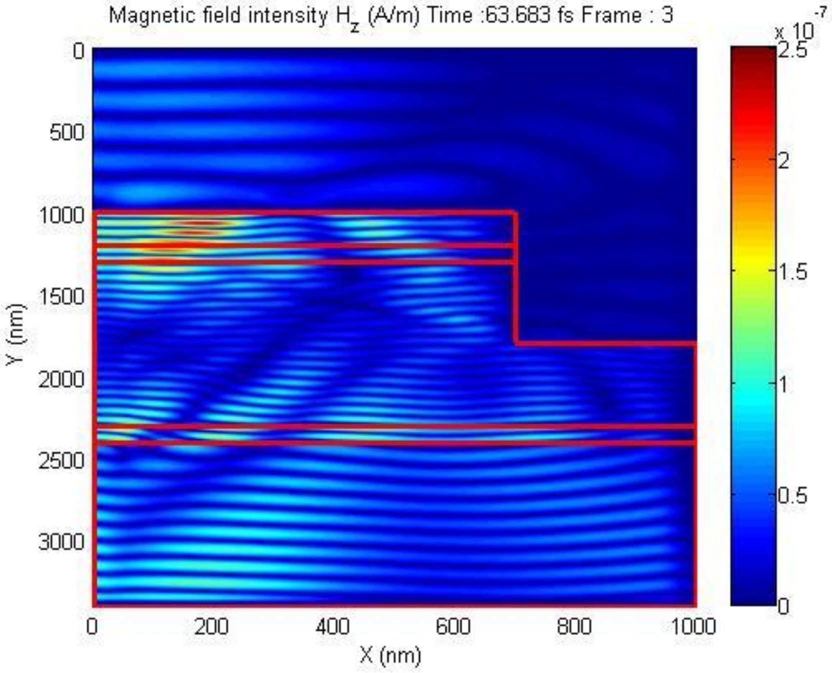

Figure 5.16 Snapshot of Magnetic field distribution- without GaN dispersion at time t=63.83 fs (P-n-N AlGaN/ GaN DH LED).

High generation rates in $P - Al_{0.3}Ga_{0.7}N$ layers can be observed in Figure 5.18 as compared to that of case with no dispersion. The dispersion effect can also be seen in Figure 5.19 on the optical power measured in air region.

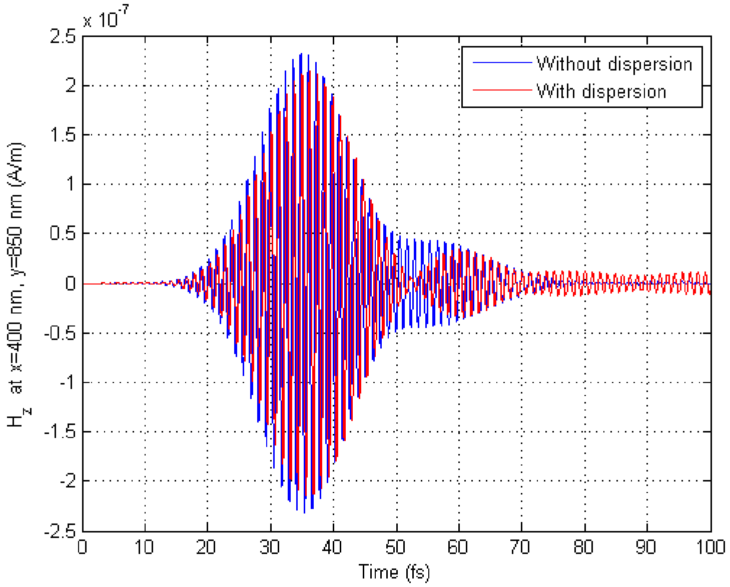

Figure 5.17 Magnetic field intensity measured in air region (P-n-N AlGaN/ GaN DH LED).

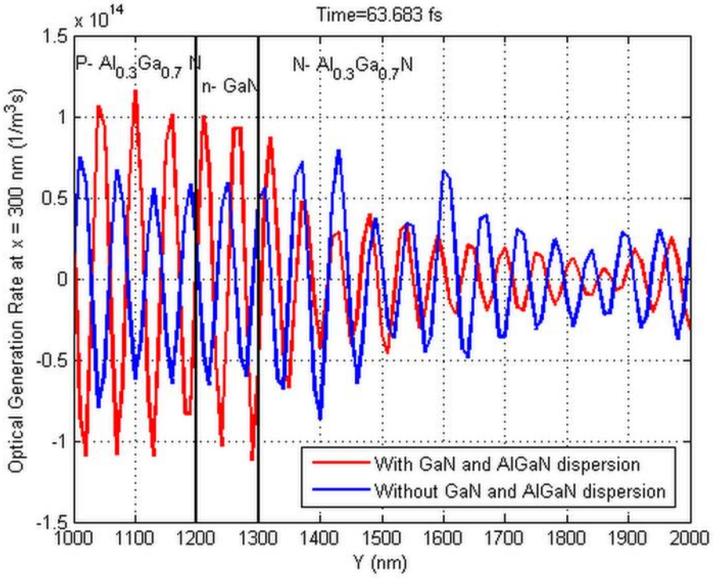

Figure 5.18 Optical Generation Rate along the width of P-n-N AlGaN/ GaN DH LED.

The generation rates and output optical powers for homojunction and DH GaN LEDs are compared in Figure 5.20 and Figure 5.21. It is apparent from these figures that the low absorption in $Al_{0.3}Ga_{0.7}N$ leads to lower generation rates and higher optical power.

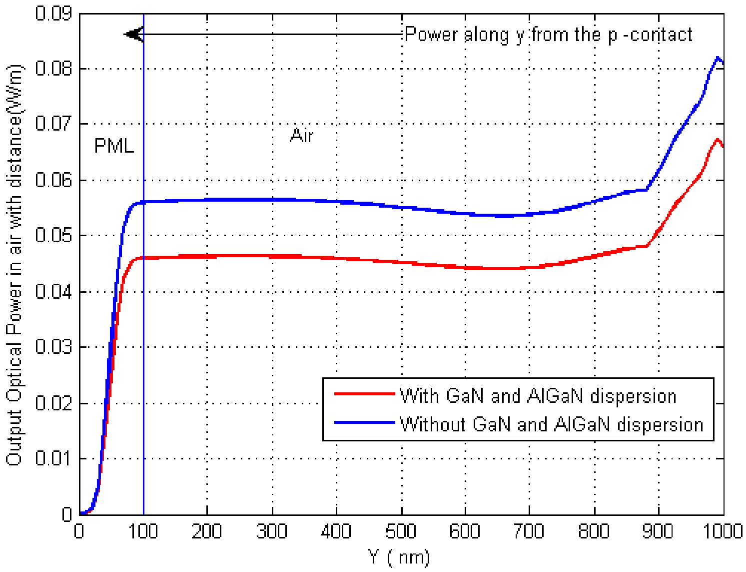

Figure 5.19 Output optical power measured in air region with distance Y (P-n-N AlGaN/ GaN DH LED).

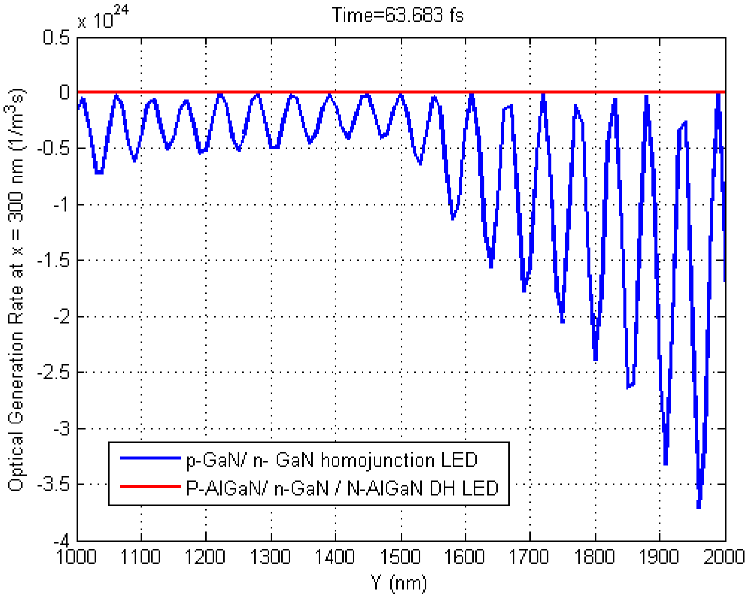

Figure 5.20 Optical Generation Rate along the width of the device (p-n LED vs. P-n-N AlGaN/ GaN DH LED).

Figure 5.22 shows the optical powers measured with gold (Au), silver (Ag) and aluminum (Al) contacts. It can be seen from this figure that the aluminum contact has high output power as compared to silver and gold contacts because of the low absorption loss property of Al at GaN emission frequencies (Figure 5.3).

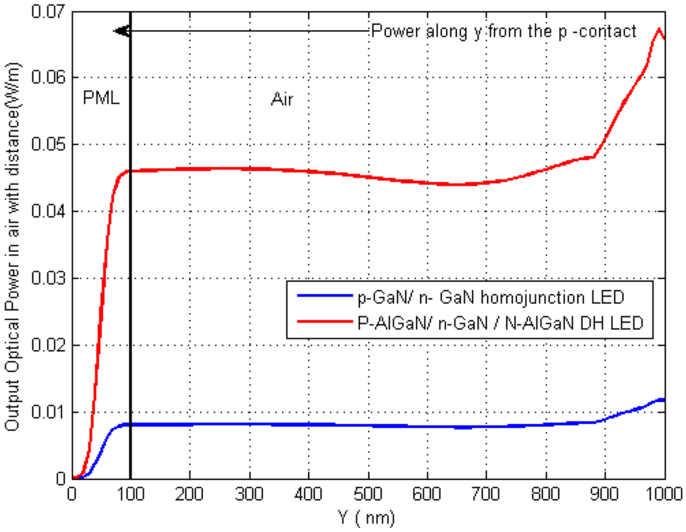

Figure 5.21 Output optical power with distance Y (p-n LED vs. P-n-N AlGaN/ GaN DH LED).

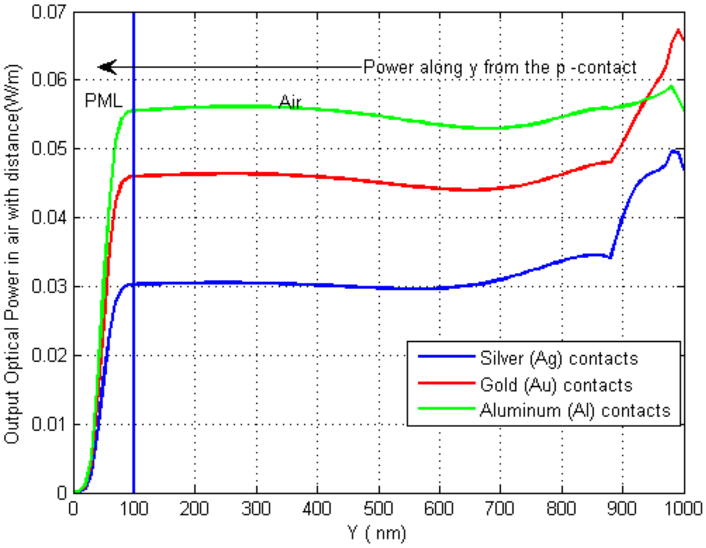

Figure 5.22 Output optical power with distance Y for P-n-N AlGaN/ GaN DH LED (Ag, Au, and Al contacts).

5.4 Summary

Light propagation inside homojunction and heterojunction GaN LEDs discussed in chapter 4 is studied using the ADE-FDTD algorithm. The structures are tested with a temporal Gaussian pulse line source with a carrier wavelength of 365 nm. Analysis shows that the material dispersion decreases the amplitudes of the EM fields and the optical power at the output due to absorption losses. The output optical powers are higher for the case of DH LEDs because shift in the absorption peak towards higher energies. The optical powers are also compared with Al, Au and Ag contacts. LEDs with Al contacts demonstrated high optical powers due to low absorption losses at GaN emission frequency.

CHAPTER 6

COUPLED ELECTRONIC-OPTICAL SIMULATION OF GaN LEDs

6.1 Introduction

This chapter investigates the coupling method to combine the carrier transport with photon emission by coupling electronic model with the optical model. The electronic-optical simulation of homojunction and heterojunction LED structures discussed in chapter 4 and 5 is investigated using the coupled model.

6.2 Coupling procedure

The photon emission is related to the band to band or radiative recombinations. Its propagation in an LED structure also depends on the absorption coefficient which is related to the absorbed power. Thus, there are two major terms that are involved in coupling the two models that are discussed in the following sections.

6.2.1 Electron-hole pair recombination for light generation

In a time domain simulation of GaN LEDs, the electron- hole pair recombinations are represented by time dependent dipole sources J_x and J_y. These dipole sources have to be modeled explicitly since the FDTD solution of optical model requires modeling the time sources explicitly. Thus, the source distribution J_x or J_y is a function of these electron-hole pair radiative recombinations and a time source. These dipole sources should have random orientations such that they have random polarizations and phases. Thus, for this work, the simulation model of GaN LED consists of an excitation or a dipole source that should be a continuous time signal and should also have emission linewidth in the output spectrum representing the emission spectrum.

The weight of dipole source at each grid point (i, j) in the simulation domain and at each time step (i.e. $J_x^{k+\frac{1}{2}}(i,j) or\, J_y^{k+\frac{1}{2}}(i,j)$) depends directly on the corresponding radiative recombination rate ($R_{radiative}^{k}(i,j)$) that is calculated from the time domain drift diffusion model. Hence from these observations, we formulate an appropriate relation between the electron-hole pair recombinations and the dipole sources that forms an important step towards coupling the two models. Thus, the expressions for the time dependent random dipole sources to be used in the coupled model are given by the following equations.

$$J_x(i,j,t) = K \times R_{rad}(i,j) \times px_r(i,j) \times s(t) \tag{6.1}$$

$$J_y(i,j,t) = K \times R_{rad}(i,j) \times py_r(i,j) \times s(t) \tag{6.2}$$

where

- $K = q \times W_{active} \times 1.102 \times 10^{-5}$ is the gauging factor given in C-m.
- W_{active} is the width of active region and q is the magnitude of electronic charge.
- The value of K is gauged by calibrating the EQE of homojunction GaN LED with the experimental values for p-GaN/ n- GaN LED given in [6] .

- R_{rad} is the radiative recombination rate that is obtained from the solution of time domain DD model.
- px_r and py_r are the random numbers (for random dipole sources) such that $px_r^2 + py_r^2 = 1$ and $0 < px_r \leq 1$, $0 < py_r \leq 1$.
- $s(t)$ is the continuous time signal with multiple output frequencies representing the continuous light emission through radiative recombinations.

6.2.1.1 Modeling time source $s(t)$

The continuous time signal with linewidth in the output spectrum is generated by summation of multiple continuous wave (CW) sources with random phases, where the weight of each CW source is given by a Gaussian distribution. Therefore, $s(t)$ is given by the following equation

$$s(t) = \sum_{k=1}^{N} G(\lambda_k) \times \left(1 - \exp\left(-(t/t_p)^2\right) \times \cos\left(\frac{2\pi}{\lambda_k} t - \phi_r\right) \qquad (6.3)$$

$G(\lambda_k)$ is a Gaussian distribution function and ϕ_r is the random phase function. $G(\lambda_k)$ is given as

$$G(\lambda) = \exp\left(-\frac{(\lambda - \lambda_0)^2}{\lambda_p^2}\right) \quad (Symmetric\ distribution) \qquad (6.4)$$

Or,

$$G(\lambda) = \exp\left(-\left(4log2\left[\frac{(\lambda - \lambda_0)^2}{r_p^2}\right]\right)\right), r_p = \frac{2\lambda_p}{1 + a(\lambda - \lambda_0)} \ (Assymetreic\ distribution) \qquad (6.5)$$

The time response of such signal is continuous and the output spectrum consists of emission linewidth with Gaussian distribution. In conclusion, the electron-hole pair radiative recombinations can be converted into a continuous random dipole sources with emission frequencies that can be used as an excitation to FDTD coupled model.

6.2.2 Light absorption for electron-hole pair generation

The electron-hole pair generation resulting from the absorption of light as it propagates inside the LED structure is also studied to couple the two models. The optical generation rate G calculated from the absorbed optical power densities are linked to the electronic part through the carrier continuity equation given by the following equations:

$$\frac{\partial n}{\partial t} = G - R + \frac{1}{q}\nabla.\boldsymbol{J_n} \tag{6.6}$$

$$\frac{\partial p}{\partial t} = G - R + \frac{1}{q}\nabla.\boldsymbol{J_p} \tag{6.7}$$

The optical carrier generation rate G is calculated from the EM fields obtained from coupled model simulation. It is given by the following equation as discussed in chapter 5.

$$G(x,y) = -\frac{\left(\frac{\partial}{\partial x}\left(E_y H_z\right) - \frac{\partial}{\partial y}\left(E_x H_z\right)\right)}{E_{ph}} \tag{6.8}$$

Figure 6.1 shows the FDTD algorithm for the coupled model. The link shown in the figure to couple the two models is based on calculating the current densities at each time step using the radiative recombinations obtained from the solution of electronic model.

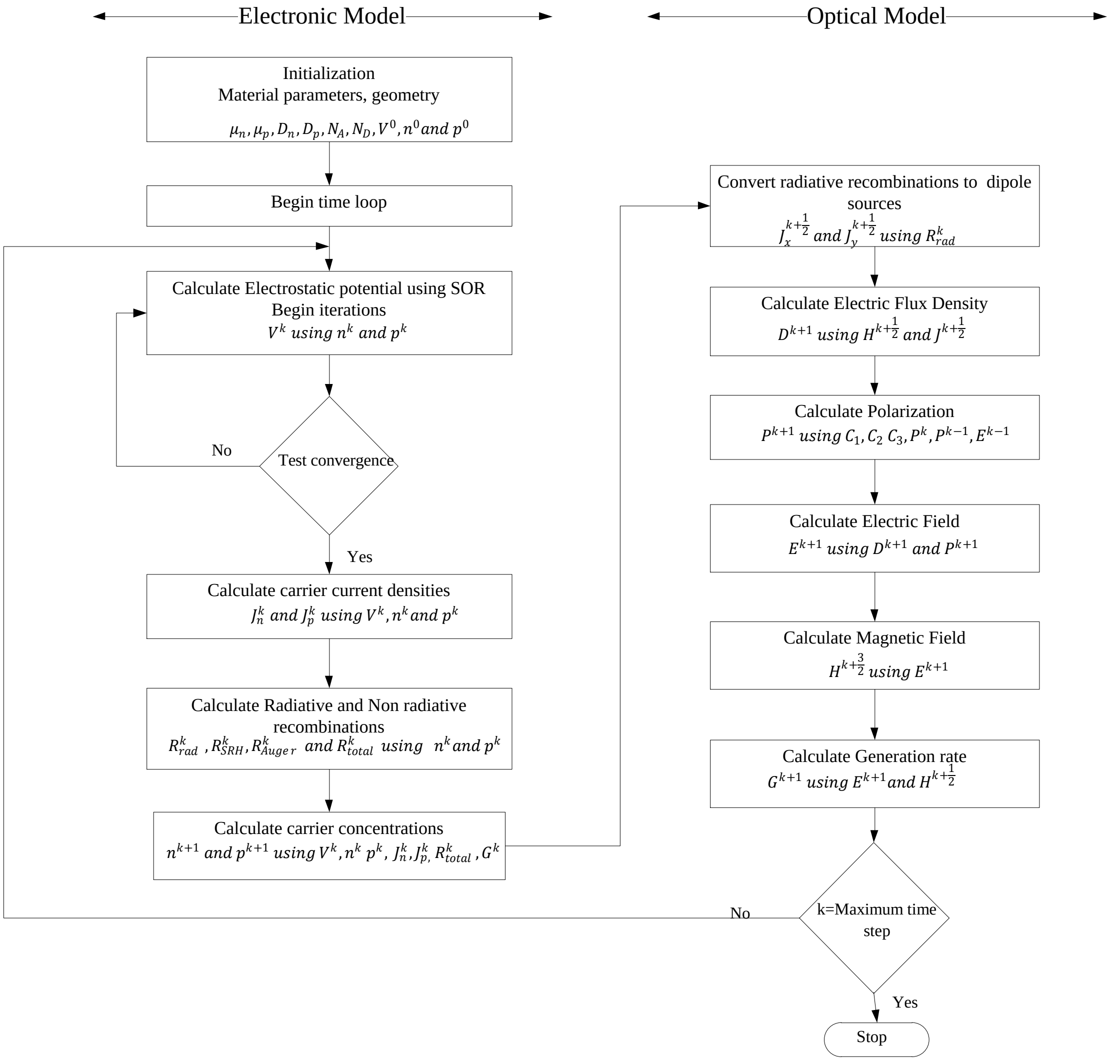

Figure 6.1 Coupled model algorithm.

6.3 Coupled model simulation of GaN LED structures

The simulation of homojunction and DH GaN LED structures discussed in chapter 4 and 5 is investigated using the coupled model algorithm. The LED structures are compared in terms of optical power and external quantum efficiencies (EQE). The light generation is demonstrated by the radiative recombination rates and the light absorption by the material dispersion and optical generation rates.

6.3.1 Inputs to the coupled model

For all the LED structures that are studied using the coupled model, the input source is a continuous random dipole source with linewidth that is modeled using the procedure discussed in section 6.2 using equations (6.1)-(6.5). Figure 6.2 shows the input dipole source of homojunction GaN LED (Figure 5.7) measured at $x = 300\ nm, y = 1300\ nm$. Such input sources are initialized at all the grid points inside the LED structure. The strength of dipole source at each point and each time is given by the radiative recombination rate at that point.

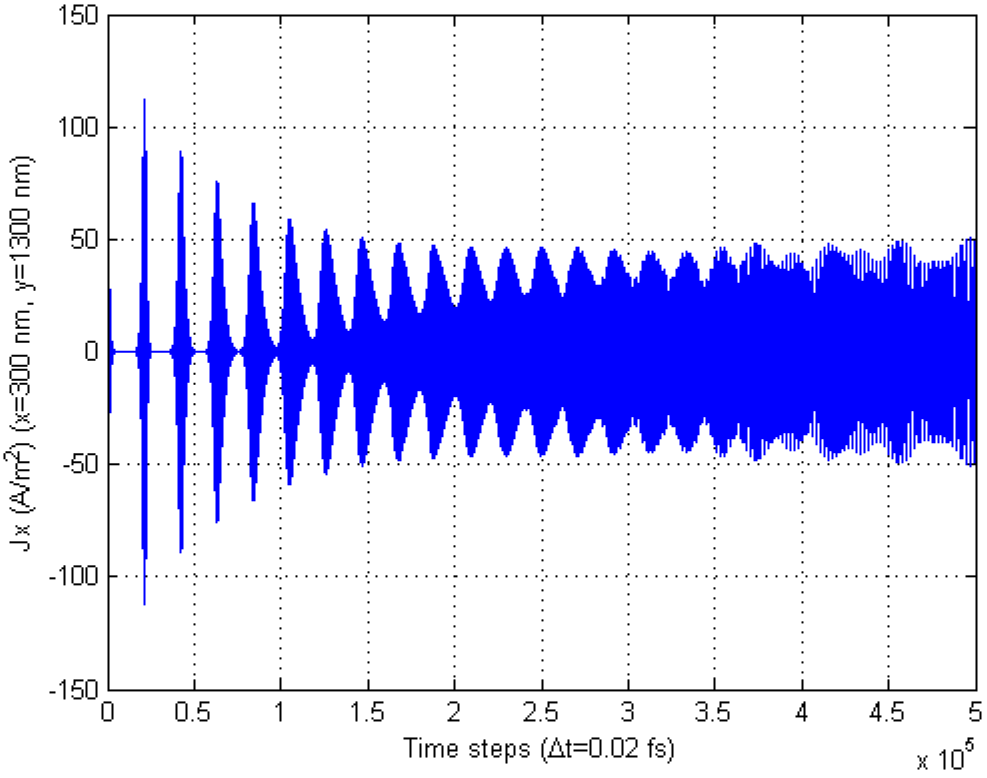

Figure 6.2 Input continuous wave for simulation of GaN LEDs with Coupled Model.

6.3.2 Coupled model simulation results of GaN LED structures

As it can be seen from the coupled model algorithm shown in Figure 6.1, the radiative recombination rates calculated from the electronic model are used in the optical model to calculate the dipole sources, whereas the optical generation rate calculated from the optical model is used in the electronic model to calculate the electron and hole concentrations. This procedure basically couples the two models as discussed in section 6.2. The generation rate and the recombination rates have to be compared in order to see the effect of optical generation rate on electronic model through the continuity equation (equations (6.6)-(6.7)).

Figure 6.3 compares the radiative recombination and generation rates for a homogeneous GaN LED structure. The radiative recombination rate is more effective than the generation rate when these values are substituted in continuity equation because of low amplitudes of generation rates. This implies that the generation rates have no significant effect on the solutions of electronic model. Therefore, the radiative recombination rate is the most important term that couples the two models.

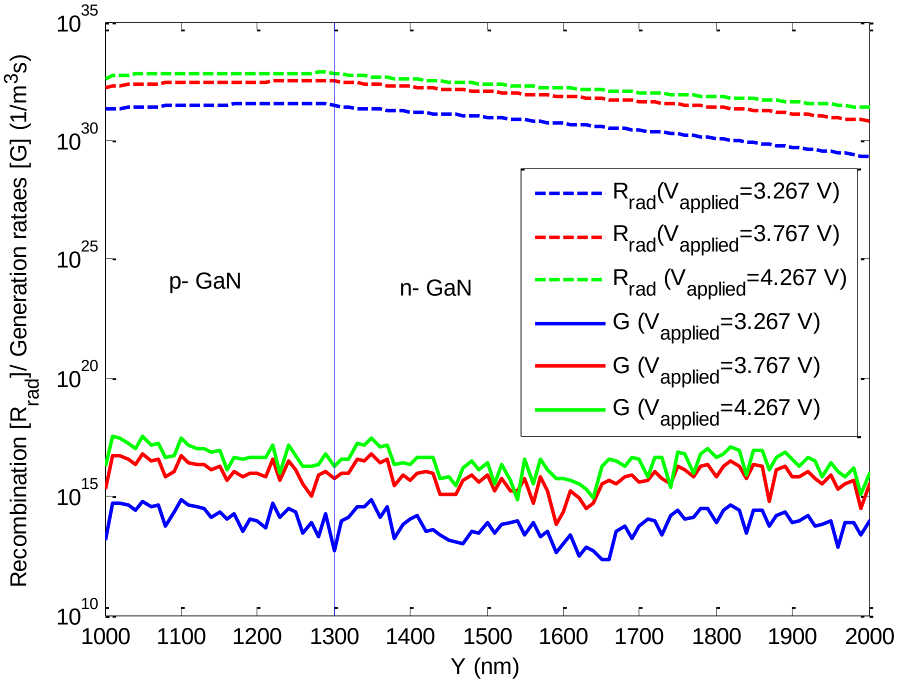

Figure 6.3 Comparison of Recombination and Generation rates of homojunction GaN LED.

The field distribution inside a homojunction GaN LED simulated using the coupled model with random dipole sources is shown in Figure 6.4 describing the propagation of EM field inside this device.

The emission spectrum of homojunction GaN LED is compared with the experimental result [5] as shown in Figure 6.5. The fabricated p-n homojunction GaN UV-LED [5] consisting of a p-type GaN layer doped at $2 \times 10^{20}\ cm^{-3}$, and an n-type GaN layer doped at $2 \times 10^{17}\ cm^{-3}$ emits at 370 nm as seen in Figure 6.5 whereas the simulated result has an emission around 366 nm with an emission linewidth of 20 nm.

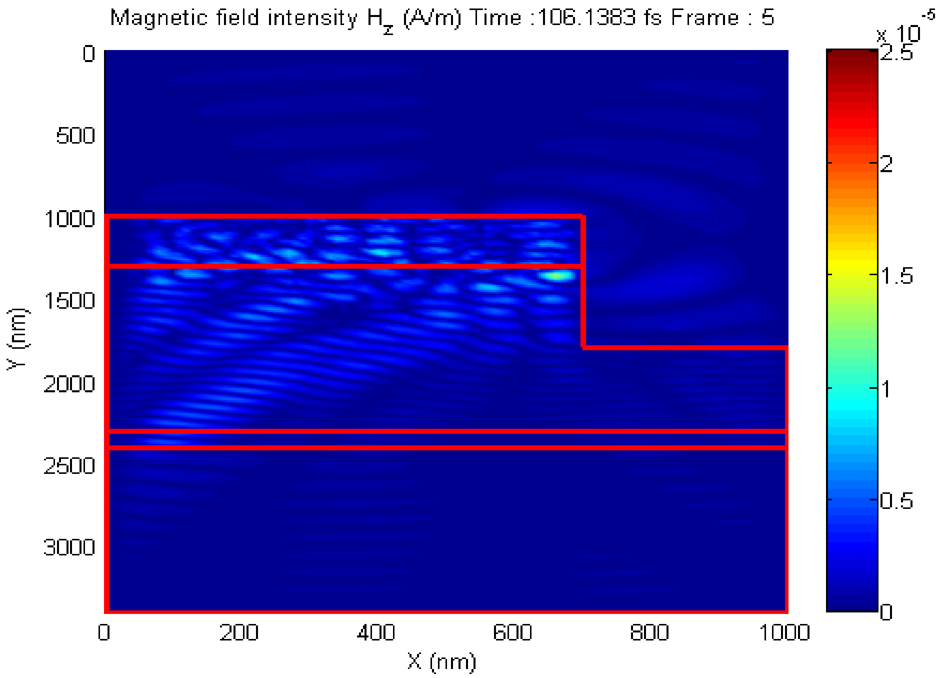

Figure 6.4 Snapshot of Magnetic field distribution for p-n homojunction LED at time $t = 106.13\ fs$ (Δt=0.02 fs, V$_{\text{applied}}$ =4.267 V).

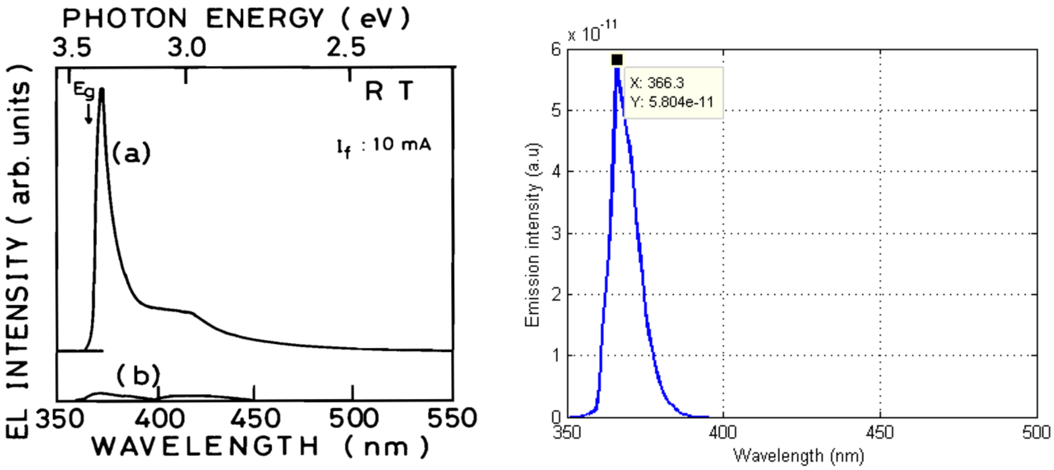

(a) **(b)**

Figure 6.5 Emission spectrum of p-n homojunction GaN LED a) Experimental result ([5]) b) Coupled model simulation.

Figure 6.6 and Figure 6.7 show the optical power and EQE of homojunction GaN LED with and without the effect of dispersion respectively. It can be verified from these figures that the dipersion of GaN leads to low optical power or EQE. The maximum EQE measured for this strucuture was $0.1755\,\%$ at a forward voltage of $4.267\,V$. The experimental value of EQE for p-n homojunction GaN LED is 0.18% [6] at forward voltage of 4 V.

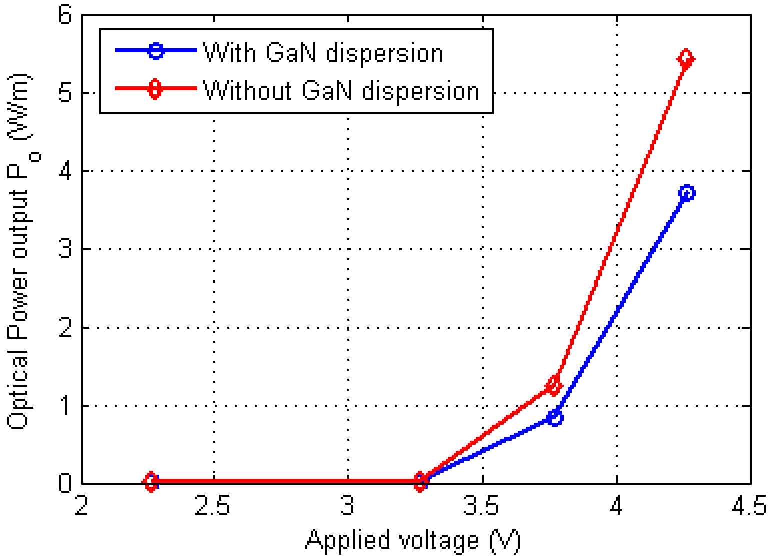

Figure 6.6 Optical power of p-n homojunction GaN LED vs. applied voltage- with and without GaN dispersion.

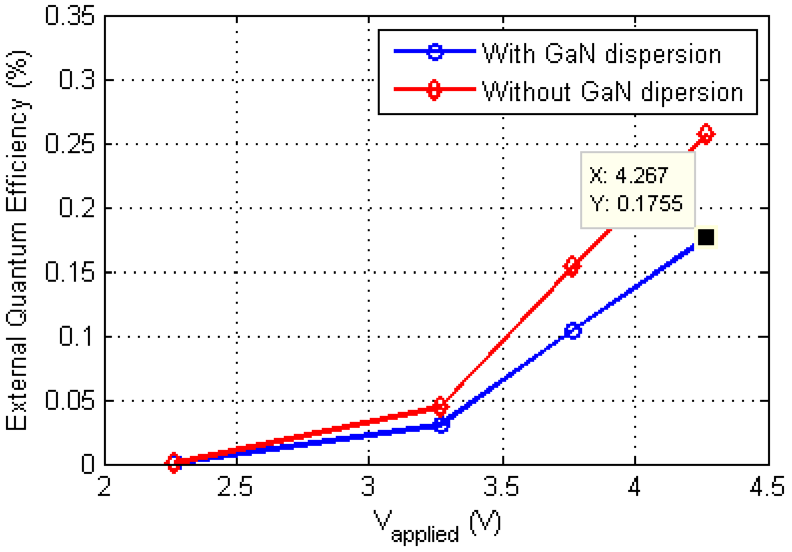

Figure 6.7 External quantum efficiency (EQE) of p-n homojunction GaN LED vs. applied voltage- with and without GaN dispersion.

Next, the optical power and EQE of p-i-n GaN LED are compared with p-n GaN LED as shown in Figure 6.11 and Figure 6.12. The addition of an intrinsic GaN layer increases the effective recombination area and therefore has high EQE as compared to that of p-n GaN LED. The maximum EQE of this structure was found to be 0.39 % at $V_{applied} = 4.267\ V$. The improvement in the EQE for p-i-n GaN LED results from high radiative recombinations inside the active region as compared to that of p-n LED.

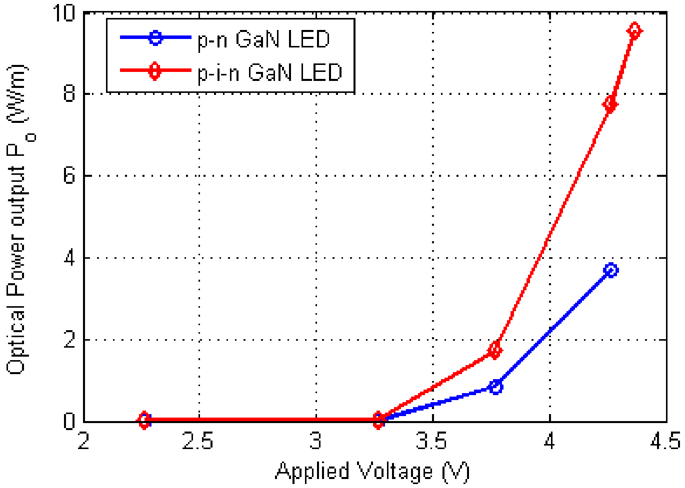

Figure 6.8 Output optical power vs. applied voltage (p-n vs. p-i-n GaN LED).

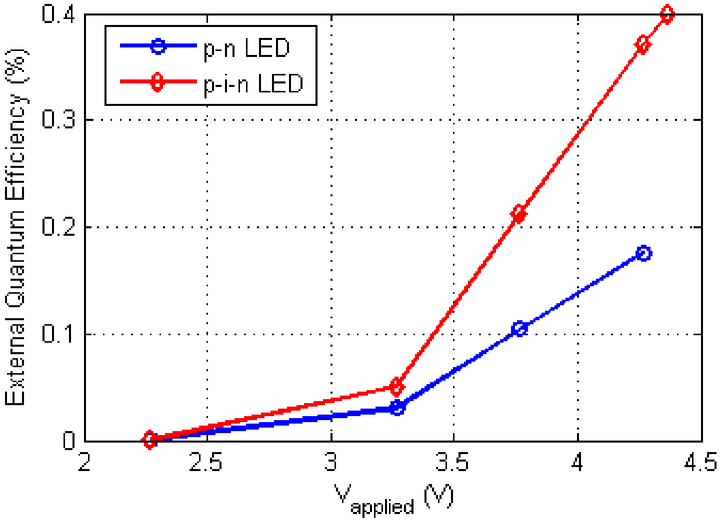

Figure 6.9 EQE vs. applied voltage (p-n vs. p-i-n GaN LED).

Finally, the optical power and EQE of DH LED is compared with p-i-n LED. It can be seen that the magnetic fields in an AlGaN/ GaN DH LED have low absorption loss as compared to homojunction GaN LED that is clear from the field amplitudes as shown in Figure 6.4 and Figure 6.10. The optical power and EQE of AlGaN/ GaN DH LED are shown in Figure 6.11 and Figure 6.12. The maximum EQE was found to be 1.03 % at a forward voltage of $4.101\,V$ (Figure 6.12). The improvement in the EQE using DH is because of improvements in both recombination rates and optical power.

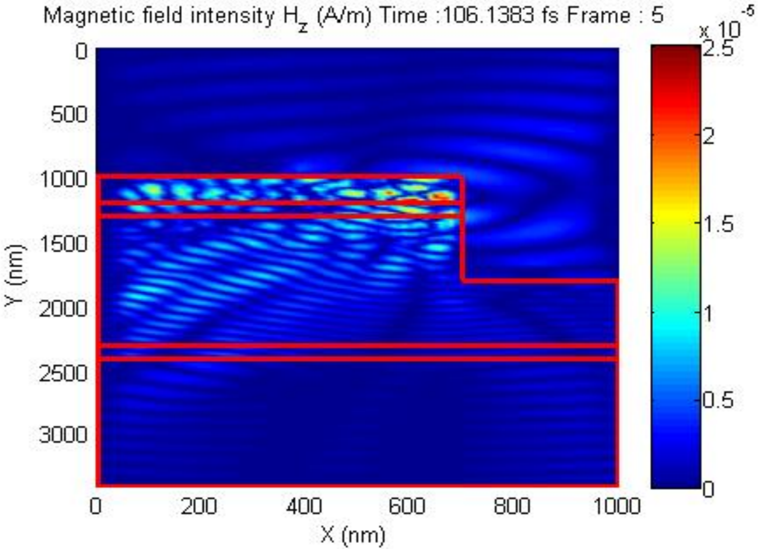

Figure 6.10 Snapshot of Magnetic field distribution for AlGaN/ GaN DH LED at time $t = 106.13\ fs$.

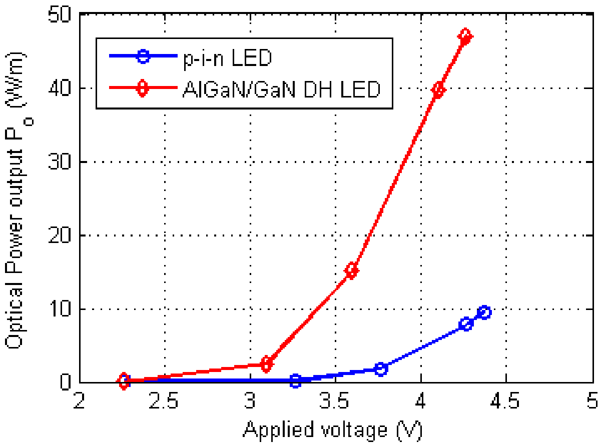

Figure 6.11 Output optical power vs. applied voltage (p-i-n GaN LED vs. AlGaN/ GaN DH LED).

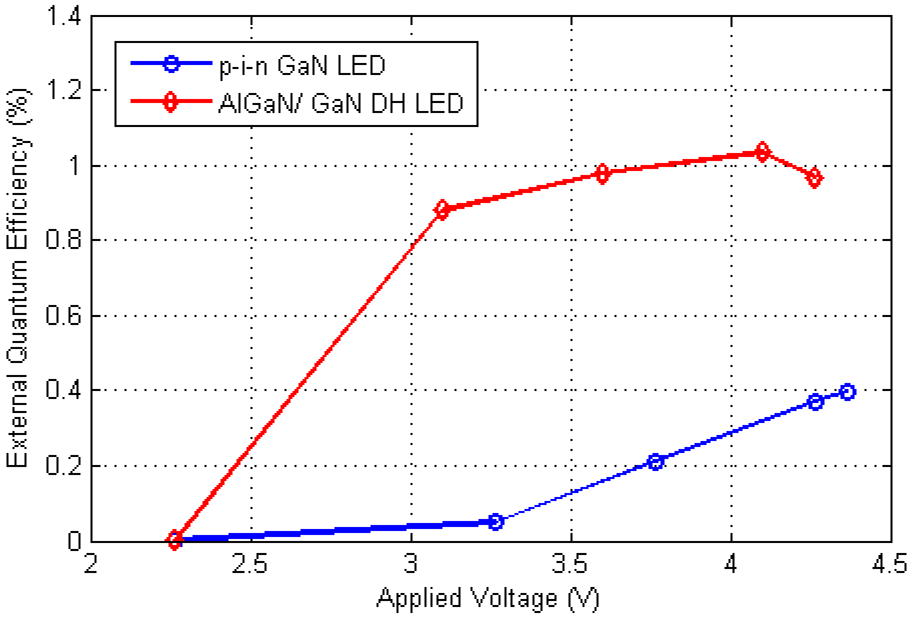

Figure 6.12 EQE vs. applied voltage (p-i-n GaN LED vs. AlGaN/ GaN DH LED).

6.4 Summary

The electron-hole pair radiative recombination rate is found to be the major parameter to couple the electronic and the optical model. The expressions involving the conversion of recombination rates to random dipole sources are presented in the coupling procedure. The coupled model simulation results of homojunction and heterojunction GaN LEDs discussed in chapters 4 and 5 are explained. The optical power and EQE obtained from coupled model and EQE is found higher for DH LEDs that are explained as a combined effect of carrier transport and optical simulation results.

CHAPTER 7

APPLICATIONS OF THE COUPLED MODEL

7.1 Introduction

In this chapter, two applications of the coupled model for investigating the improved LED designs in both electronic and optical aspects are presented. First, an AlGaN/ GaN DH LED with holes in the metal contact i.e. array of metal contacts is proposed to achieve enhanced optical power through extraordinary transmission (EOT) that occurs only for TM polarization. Second, an AlGaN/ GaN multiple heterojunction (MH) LED with array of metal contacts is proposed to achieve both enhanced optical power and carrier confinement.

Various studies have been proposed in the literature to increase the external efficiencies such as the use of metal nanoparticles, surface plasmons, nanoantennas, dielectric nanoantenna arrays, optical nanoholes [66]–[68] coupled with the light emission. The metal nanoparticles have the property to manipulate light at sub-wavelength scales and they can resonate at optical frequencies that can be tuned with their sizes, shapes and configuration. The basic idea in such studies is to resonate the metal nanoparticles at emission frequency of GaN LED structures. However, these investigations involve only optical simulation assuming that the enhancement is only due to the resonance of EM fields inside the device.

We will therefore investigate AlGaN/ GaN DH and MH LEDs with array of silver contacts using the coupled model that can demonstrate the light enhancement resulting from both the electronic and optical parameters.

7.2 AlGaN/GaN DH LED with subwavelength array of silver contacts

Figure 7.1 shows the AlGaN/ GaN DH LED with array of silver contacts of length L, thickness H and spacing S. The field enhancement can be achieved through extra ordinary transmission (EOT) through these sub wavelength metal contacts. This EOT is caused due to the localized surface plasmon resonances (LSPR) at the surface of metal contacts. The surface plasmon resonances (SPR) are the coherent oscillations of electrons close to metal surface when excited by properly polarized light [69]. When surface plasmons are excited in a metal nanoparticle, they are called localized SPR. They can be enhanced and localized on the metal surface and can be confined to sub wavelength scales. Therefore, for the field enhancement, the array of metal contacts placed on top surface of GaN LED should resonate at emission wavelength.

Therefore, the first step is to determine the configuration of these metal contacts such that they resonate at emission wavelength of GaN. The resonance of the array of metal contacts can be found by determining the scattered power spectrum since these contacts scatter more power at resonance than at off-resonance. Further optimization of the configuration is done by determining the transmission spectrum of metal contacts (Silver)/ dielectric (AlGaN) configuration to find enhancement in optical powers. Finally, this configuration is used in a real LED structure i.e. AlGaN/ GaN DH LED structure and is investigated with the electronic, optical and coupled model.

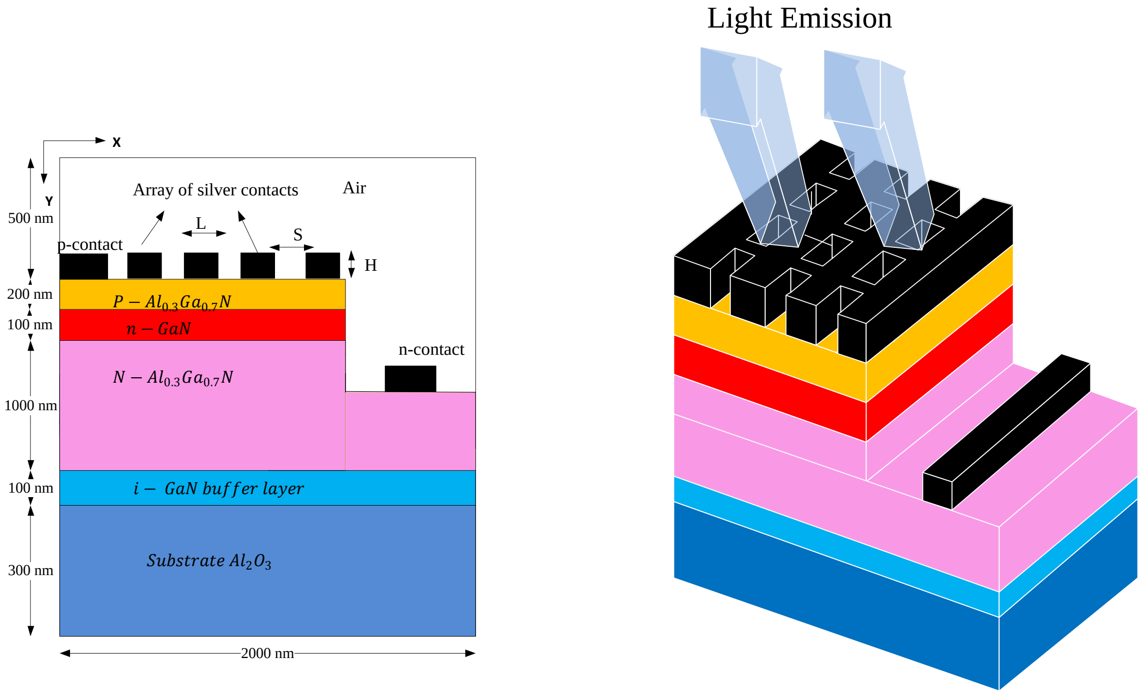

Figure 7.1 Schematic of AlGaN/ GaN DH LED with holes in the metal contact (silver contact array).

7.2.1 Scattered power spectrum

The resonance of silver contact array is determined from the scattering power spectrum calculated from scattered fields that are solved using TFSF theory. Figure 7.2 shows the FDTD-TFSF simulation domain to study the scattering properties of the metal contact array. The scattered power is given by the following expression

$$P_{sca} = \oint_{S1} S_{sca}.\hat{n} \;\; dl = \oint_{S1} (E_{sca} \times H_{sca}).\hat{n} \;\; dl \tag{7.1}$$

where, S_1 is closed rectangular path through the scattered field region, E_{sca} and H_{sca} are the EM fields in the scattered field region.

Figure 7.3 shows the input to FDTD-TFSF domain i.e. a Gaussian in time plane wave with a central wavelength of 600 nm that covers entire optical frequencies.

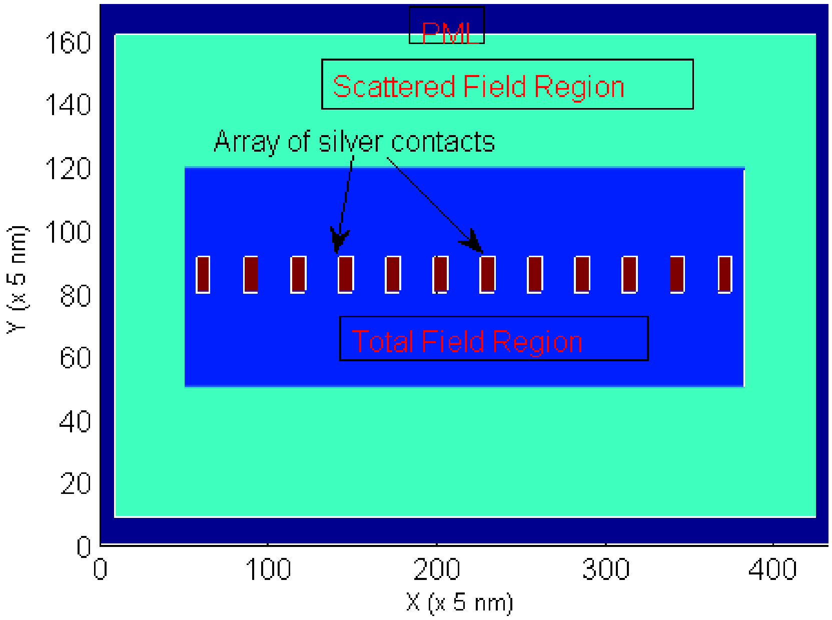

Figure 7.2 FDTD-TFSF Simulation domain to determine resonance of silver contact array.

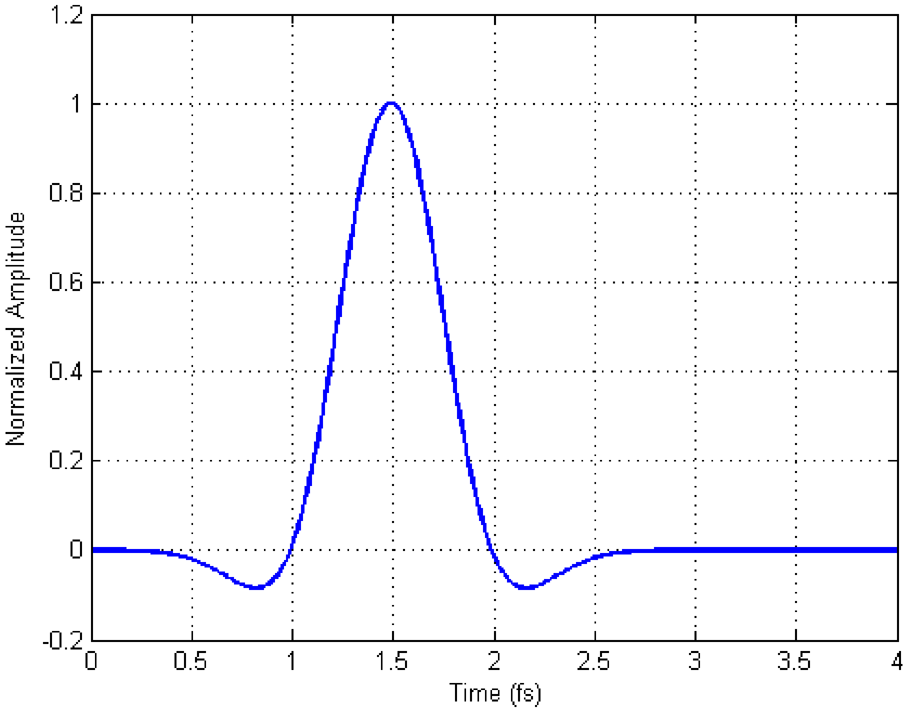

Figure 7.3 Input Gaussian temporal pulse for FDTD- TFSF simulation.

Figure 7.4 shows the scattering of magnetic field as it propagates inside the medium. The figure also shows the strongly coupled magnetic fields at the surfaces of the metal contacts that indicate the presence of localized surface plasmon waves confined at metal/ dielectric interface. Figure 7.4 (a) shows the plane wave at time 2.2407 fs, before it interacts with the array of silver contacts. Later at time 3.361 fs, the plane wave is transmitted through silver contact array and the coupled TM polarized waves that are confined and localized at the surface of silver contact can be seen in Figure 7.4 (b) that also shows the localized surface plasmon resonances on the surface of silver contacts.

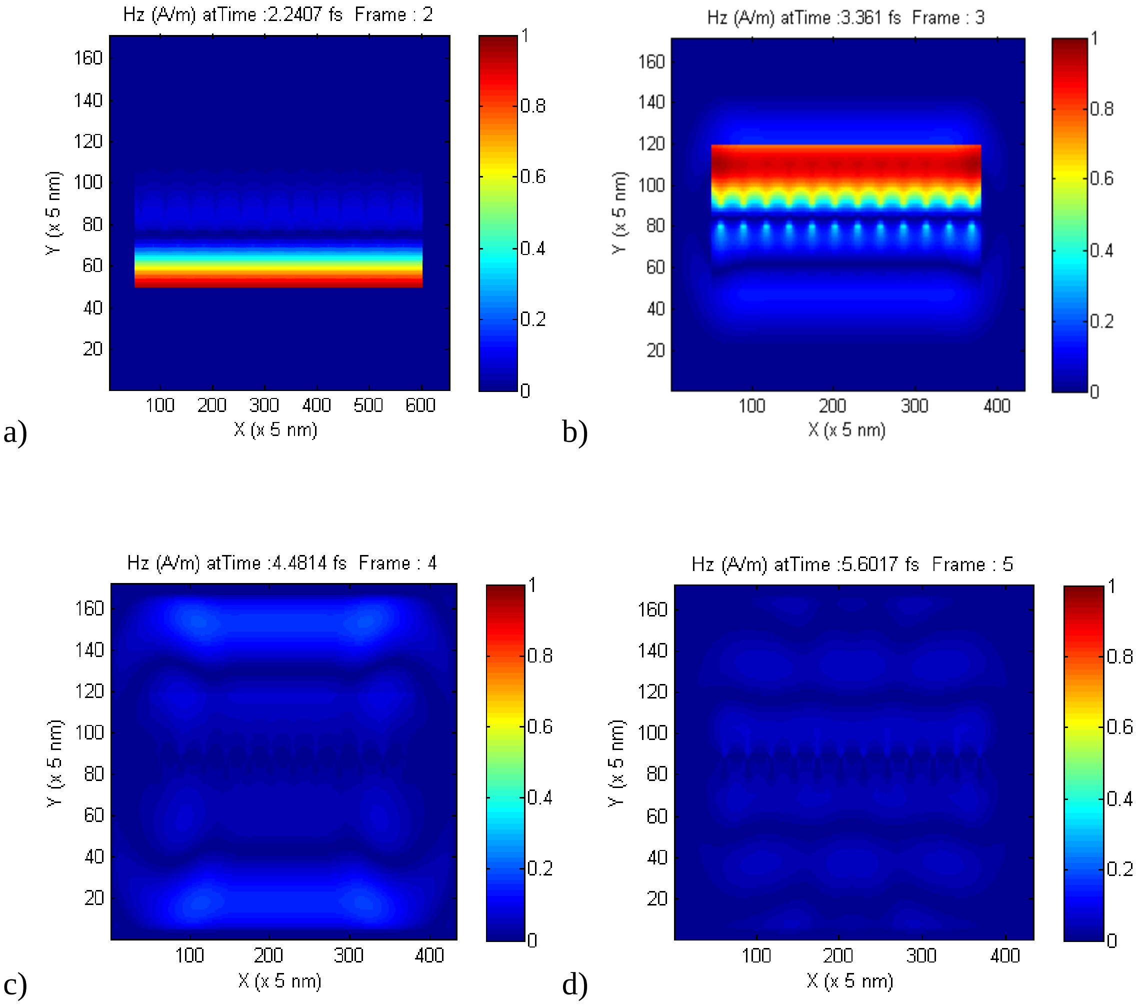

Figure 7.4 Snapshots showing the scattering of a plane wave as it propagate in FDTD-TFSF simulation domain.

To determine the configuration of the metal contact array for which they resonate at $365\,nm$, we study the effect of the dimensions and spacing of the metal contacts. The following configurations are studied to achieve resonance at emission wavelength using TFSF theory .

- Configuration-I: Number of metal contacs $N = 2$, Thickness of the contact $H = 50\,nm$, Spacing between the contacts $S = 100\,nm$, Varying parameter: $L = 100\,nm\ to\ 50\,nm$
- Configuration-II: $L = 40\,nm$, $H = 50\,nm$, $S = 100\,nm$, Varying parameter: $N = 2\ to\ 12$
- Configuration-III: $L = 40\,nm$, $H = 50\,nm$, $N = 12$, Varying parameter: $S = 50\,nm\ to\ 100\,nm$

Figure 7.5 shows the scattering power spectrum of configuration-I. The peak wavelength of the scattering spectrum corresponds to the resonance wavelength of that configuration. It can be noticed that scattering spectrum redshifts ($353\,nm\ to\ 425\,nm$) and broadens with increase in the lengths of contacts ($20\,nm\ to\ 100\,nm$). It is also found that the the configuartion-I resonates at $366\,nm$ (emission wavelength) for $L = 40\,nm$.

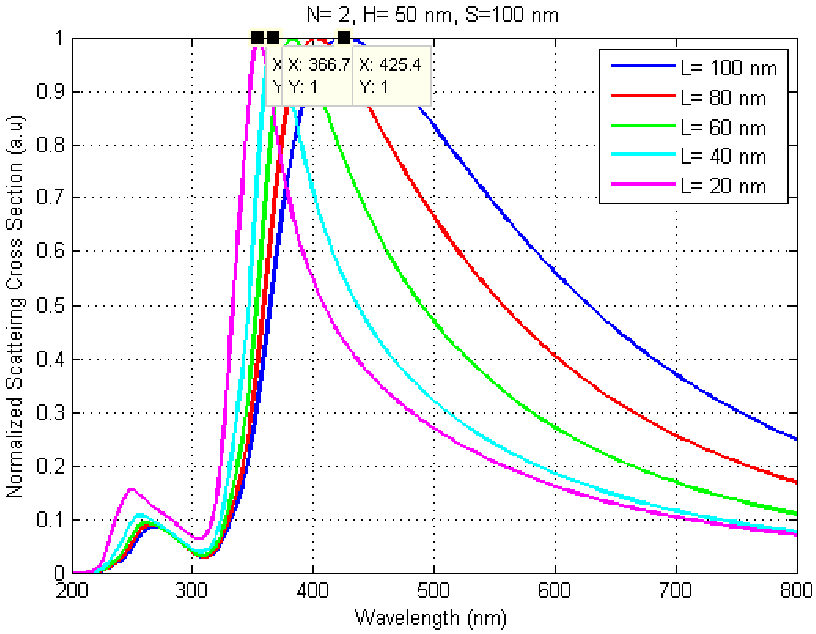

Figure 7.5 Scattering cross section of configuration-I: N=2, H= 50 nm, S= 100 nm and L= 100nm to 50 nm.

It can be seen from Figure 7.6 that the increase in the number of metal contacts results in the broadening of spectrum with same resonant wavelength.

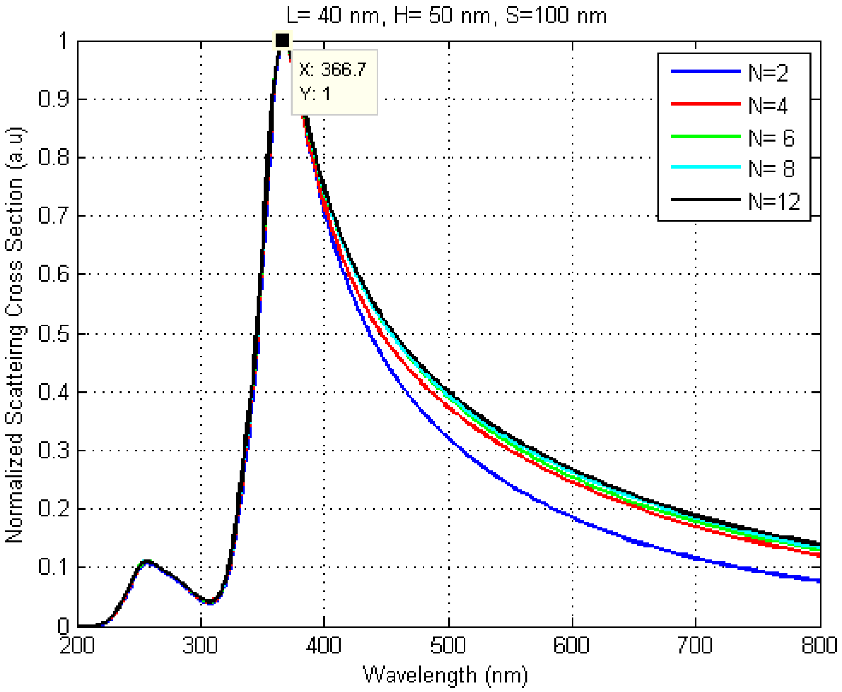

Figure 7.6 Scattering cross section of configuration-II: L=40 nm, H= 50 nm, S= 100 nm and N= 2 to 12.

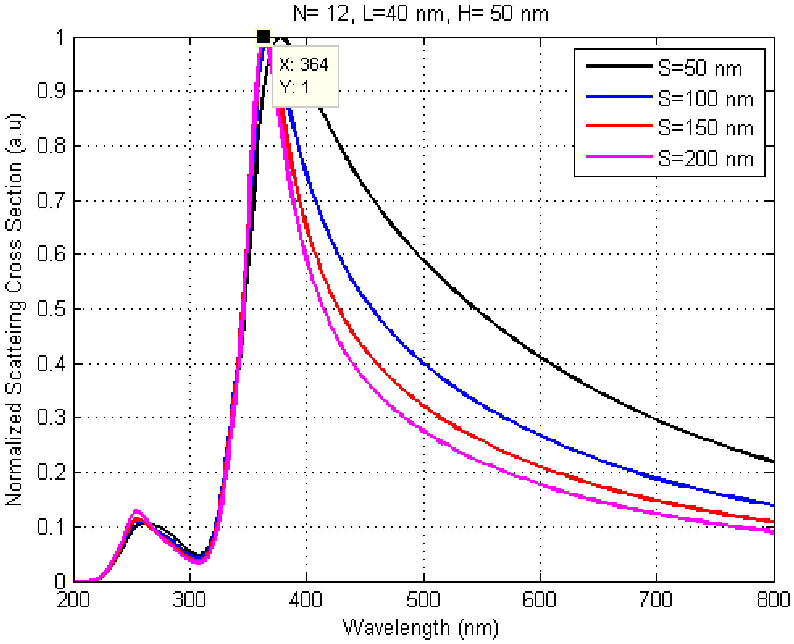

Figure 7.7 Scattering cross section of configuration-III: L=40 nm, H= 50 nm, N= 12 and S=50 nm to 100 nm.

Finally, the increase in the spacing between the contacts causes a slight redshift and broadening of the spectrum as can be seen from the scattering spectrum of configuration-III shown in Figure 7.7.

Therefore, with these studies, the configuration that can be used for resonance at $365\ nm$ is configuration- II i.e. $L = 40\ nm$,$H = 50\ nm$, $S = 100\ nm$ and $N = 2\ to\ 12$.

7.2.2 Transmission spectrum of silver contact array with AlGaN layer

The configuration is further optimized by studying the transmission properties of array of silver contact configuration with AlGaN layers as shown in Figure 7.13. In this test the power spectrum is calculated at the output with and without the silver contact array to determine the frequencies that are enhanced. The input to the structure is a short Gaussian time pulse line source ($t_0 = 0.5\ fs$) modulated with a carrier wavelength of $365\ nm$ that covers entire optical frequencies as shown in Figure 7.9 and Figure 7.10 .

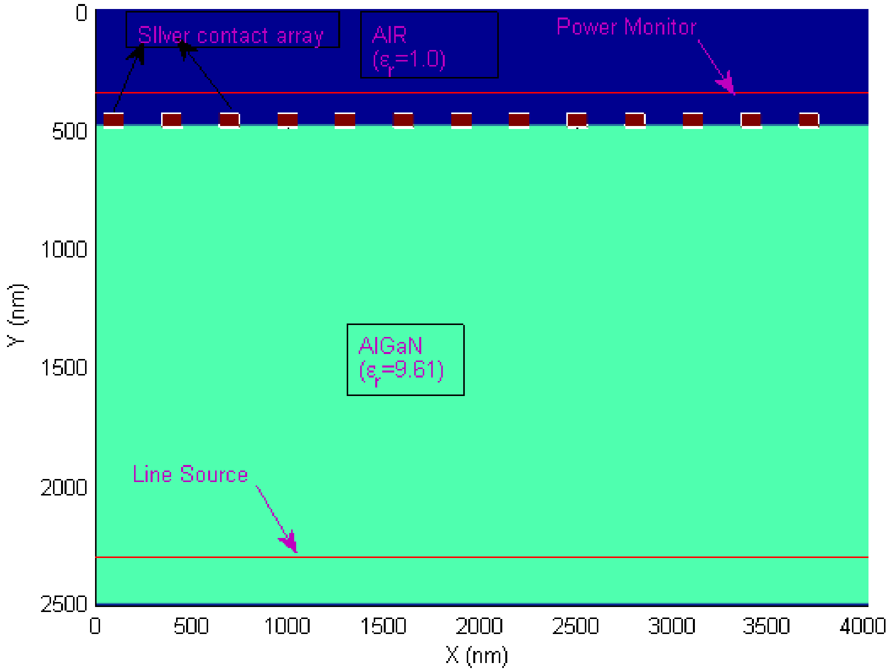

Figure 7.8 FDTD simulation domain (Silver contacts with AlGaN layers).

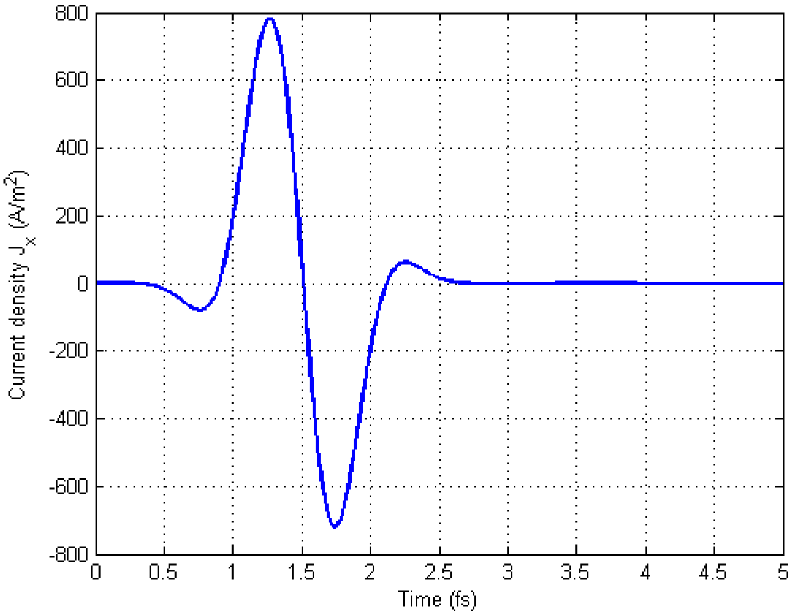

Figure 7.9 Input Gaussian temporal pulse (for structure in Figure 7.8).

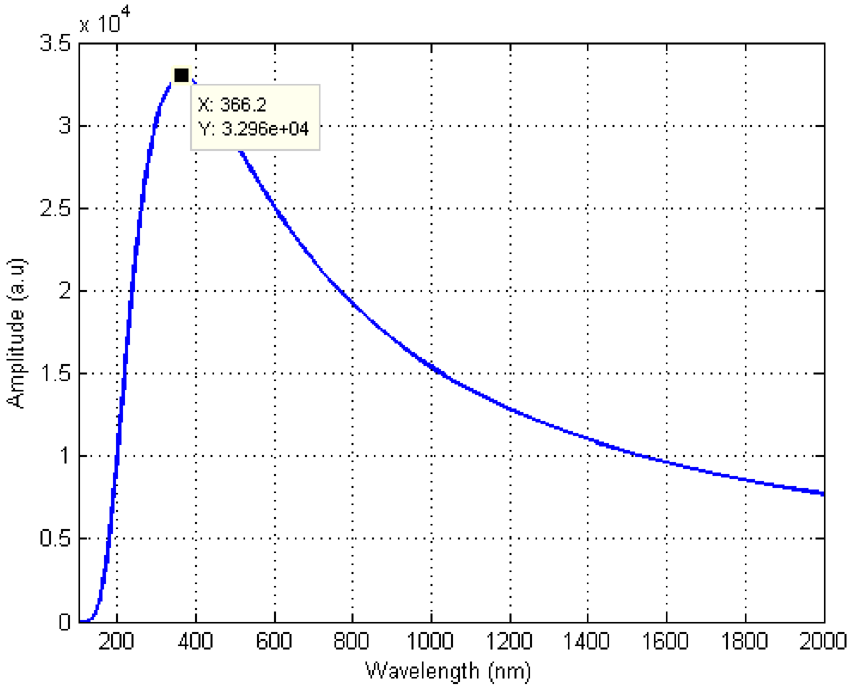

Figure 7.10 Input pulse in wavelength domain (for structure in Figure 7.8).

The transmitted and reflected magnetic fields can be seen from Figure 7.11. To determine the field enhancement, the transmission spectrum is determined as the ratio of power spectrum measured at the output with silver contact array and power spectrum measured without silver contact array. The calculated transmission spectrum is shown for the silver contact configuration obtained in previous study for varying lengths in Figure 7.12. It can be observed that the smaller lengths of silver contact enhance the output powers at 365 nm wavelength. For example, the enhancement in the optical power for length L=20 nm is found to be ~ 5 % as can be seen in Figure 7.12.

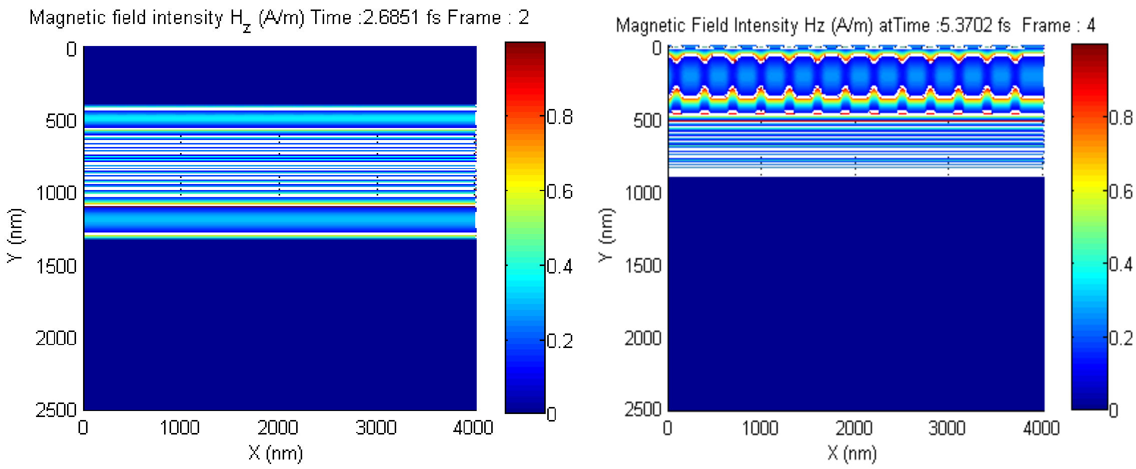

Figure 7.11 Magnetic field propagating inside AlGaN layers/ silver contact array (N=10, L=100 nm, H= 50 nm, S= 200 nm).

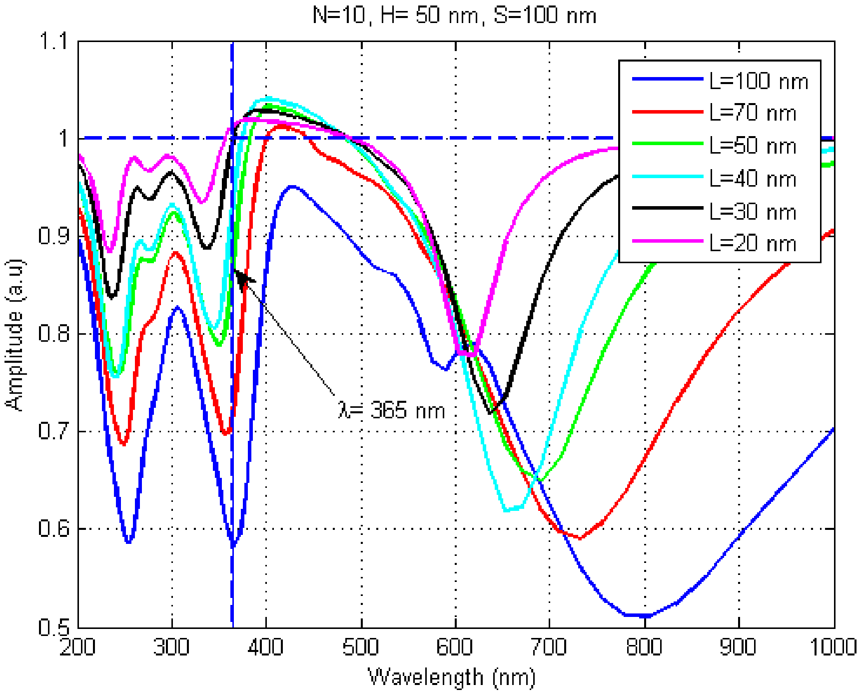

Figure 7.12 Transmission spectrum of AlGaN layers/ silver contact array for varying L.

7.2.3 Simulation results of DH LED with optimized configuration

The optimized configuration of silver contact array from the two studies that is used in the AlGaN/ GaN DH LED structure is $N = 12, L = 20\ nm, H = 50\ nm$ and $S =$

$100\,nm$ as shown in Figure 7.13 The simulation domain is $2000\,nm \times 2200\,nm$ with $\Delta x = 5\,nm, \Delta y = 10\,nm, \Delta t_{electronic} = 0.5\,fs$, $\Delta t_{optical} = 0.02\,fs, V_{applied} = 4.101\,V$.

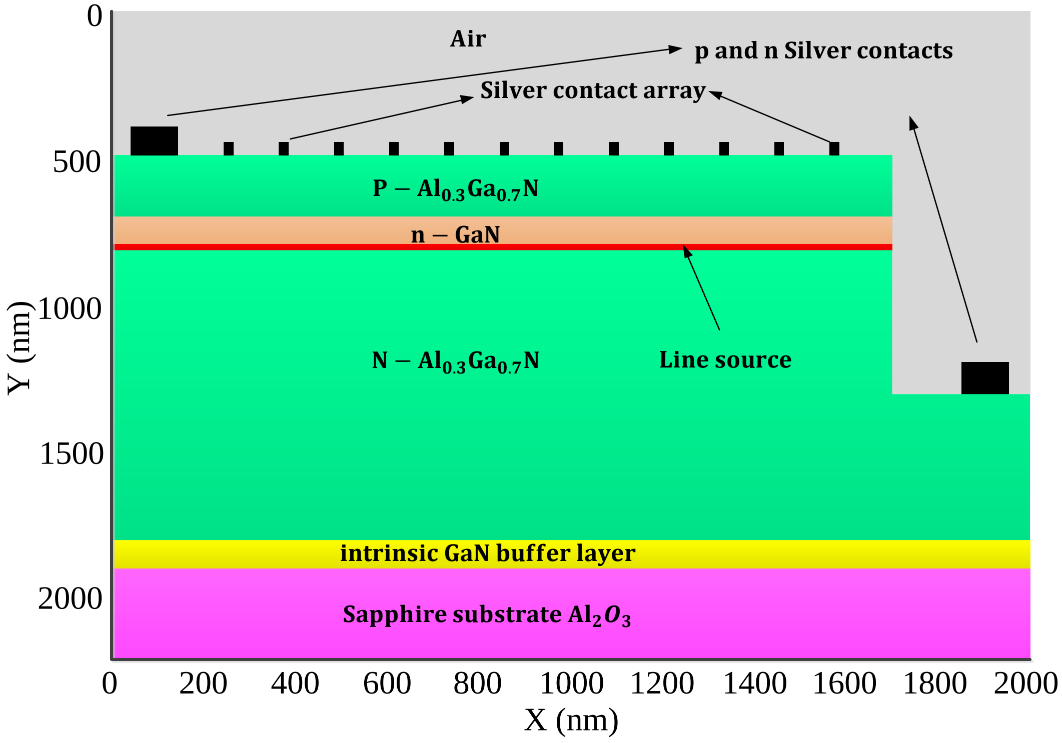

Figure 7.13 FDTD simulation domain of AlGaN/ GaN DH LED with silver contact array.

Figure 7.14 and Figure 7.15 shows the simulated potential distribution with and without silver contact array. It can be observed that the structure with silver contact array has high potential distribution at the surface and also inside the GaN LED structure as compared to that of GaN LED with single p-contact. The LED structure with the silver contact array also improves the current spreading in the device. This can be seen from Figure 7.16 and can be compared with the current distribution inside the LED without silver contact array shown in Figure 7.17. The current in Figure 7.17 has a non-uniform spreading; it is maximum near the electrodes and decreasing in the other regions. This type of current spreading in the device affects the electronic performance of the device in terms of recombination rates and injection currents.

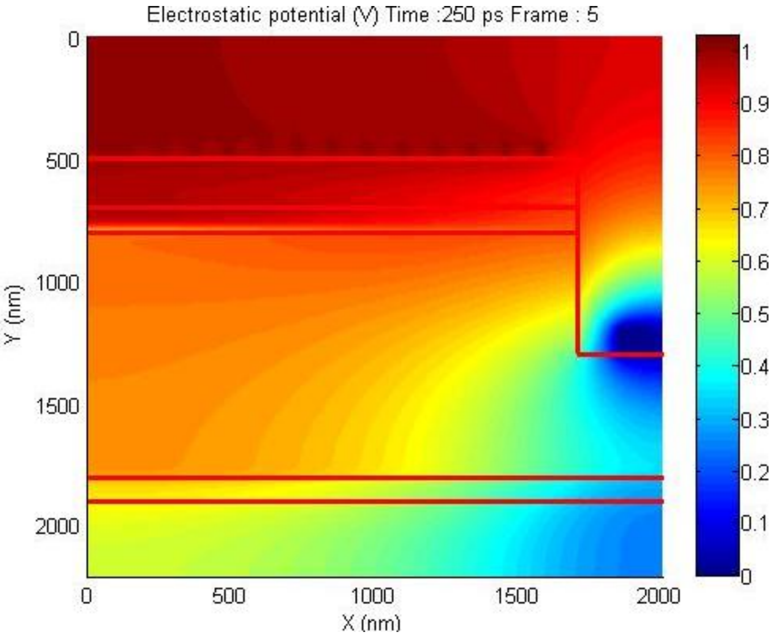

Figure 7.14 Snapshot of the Electrostatic potential distribution- with silver contact array.

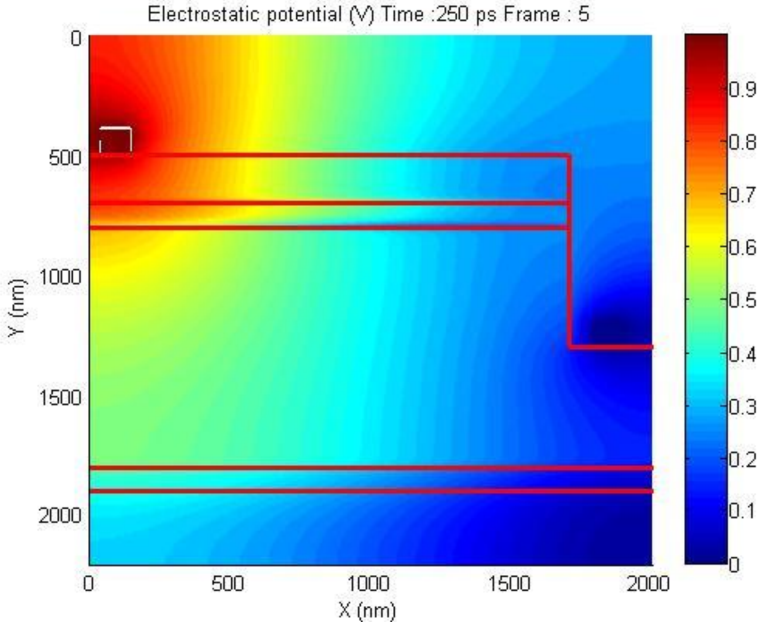

Figure 7.15 Snapshot of the Electrostatic potential distribution- without silver contact array.

Therefore, the problem of current spreading is improved with the metal contact array as compared to the structure without these contacts.

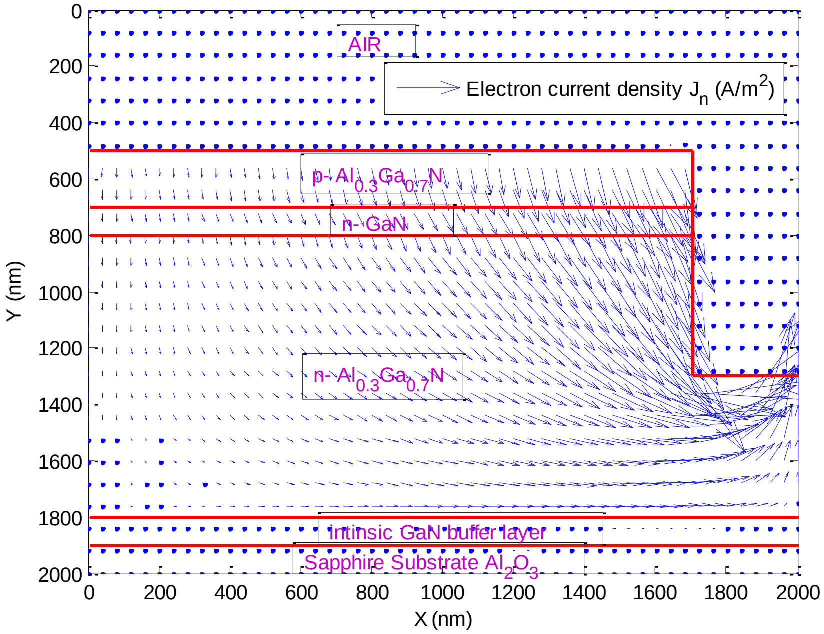

Figure 7.16 Electron current density distribution- with silver contact array.

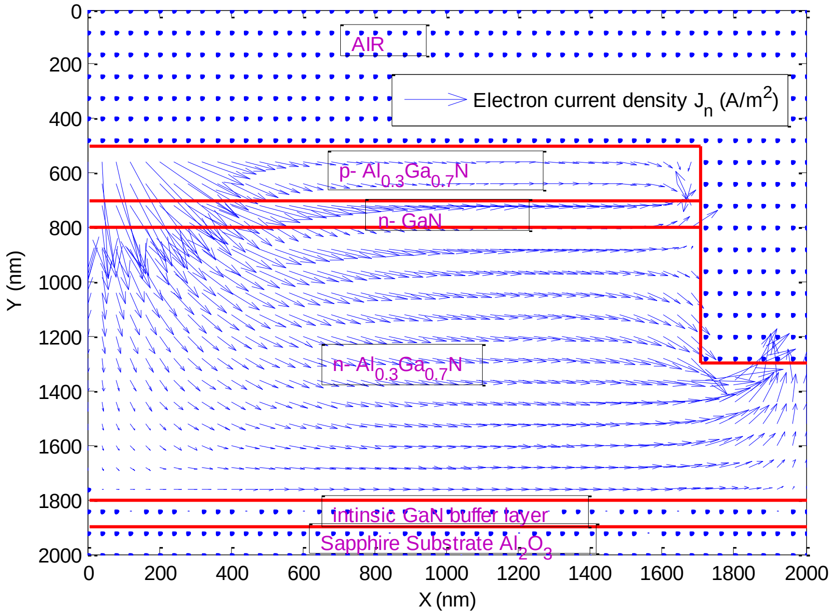

Figure 7.17 Electron current density distribution- without silver contact array.

As can be seen from the Figure 7.18, the injection currents are higher with the array of metal contacts because of high potential distribution inside the LED structure. Besides injection current, the radiative recombinations are also improved because of the improvements in the current spreading as shown in the Figure 7.19.

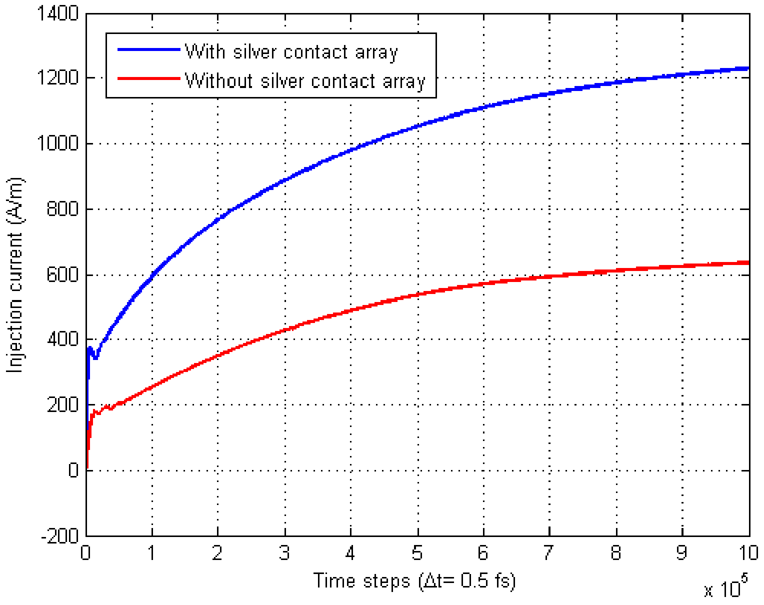

Figure 7.18 Injection currents- with and without silver contact array.

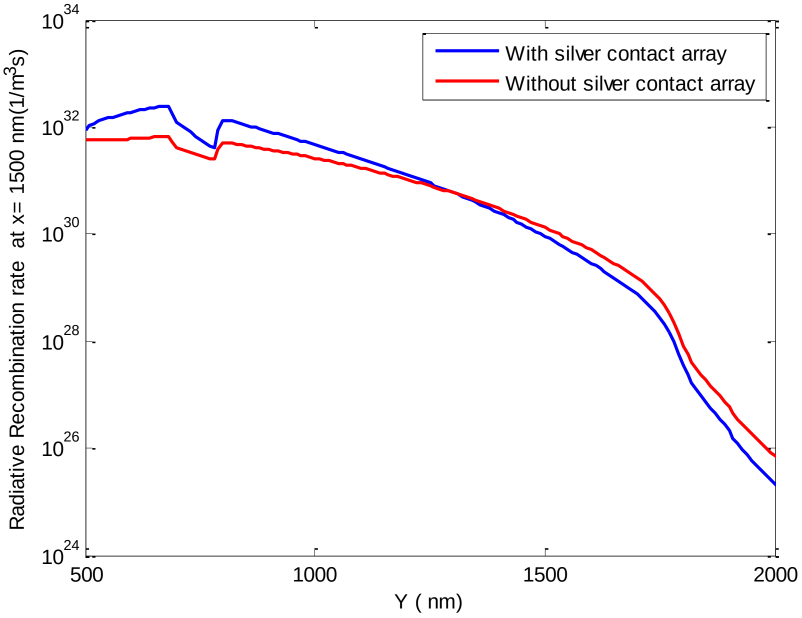

Figure 7.19 Radiative recombination rates- with and without silver contact array.

Figure 7.20 and Figure 7.21 shows the magnetic field distribution with and without silver contact array simulated using the optical model. The difference in the fields at the LED metal contact surface can be observed in these figures.

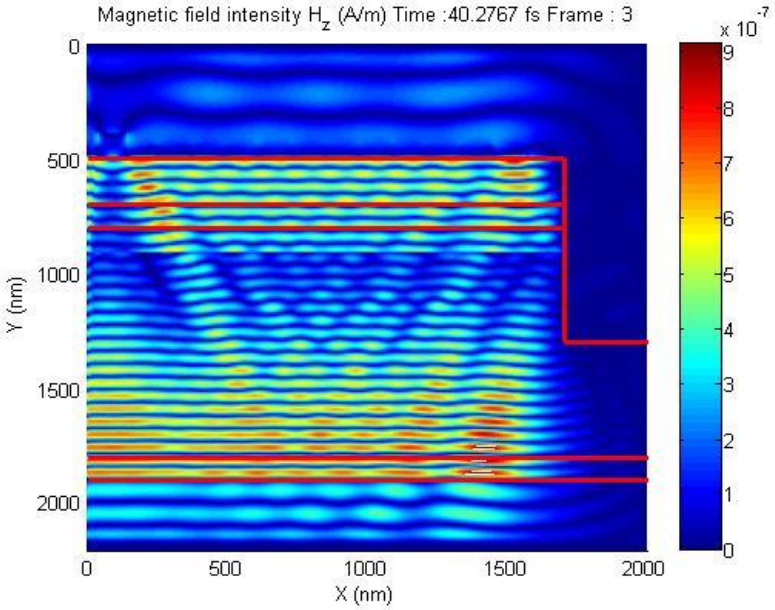

Figure 7.20 Snapshot of magnetic field distribution- with silver contact array.

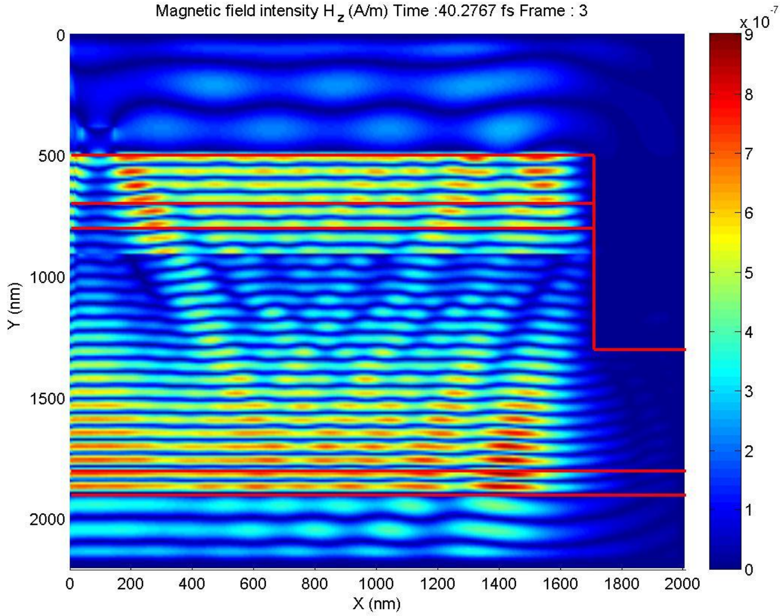

Figure 7.21 Snapshot of magnetic field distribution- without silver contact array.

The optical power found to increase with these contacts because of localized fields at the interface of AlGaN/ Silver contact array as seen in Figure 7.22 and Figure 7.23 corresponding to optical and coupled model respectively. The optical power increases by almost thrice as compared to that of the case without the silver contact array (Figure 7.23).

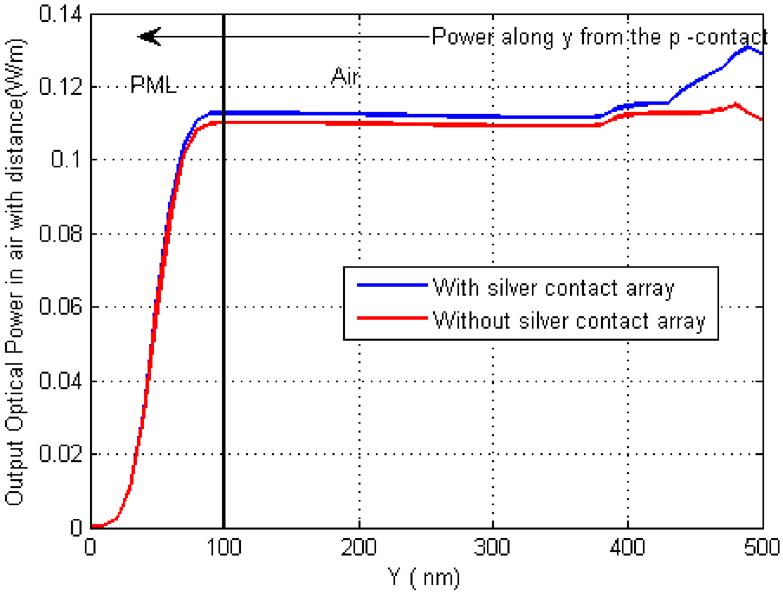

Figure 7.22 Output optical power from optical model – with and without silver contact array.

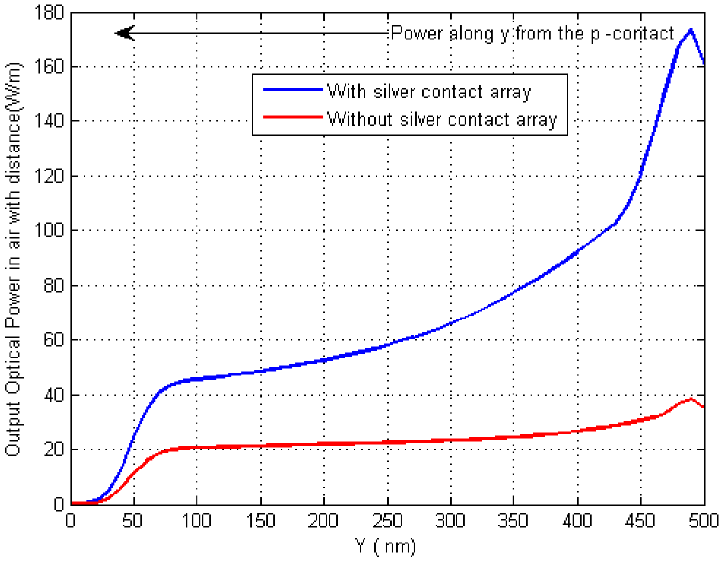

Figure 7.23 Output optical power from coupled model – with and without silver contact array.

Therefore, the combined effect of both electronic and optical model i.e. improved currents, radiative recombinations and enhanced EM fields is reflected in the coupled model output optical powers and EQE. With these improvements, the EQE of AlGaN/ GaN DH LED increased from 1.03 % to 1.825 % with the silver contact array.

7.3 AlGaN/ GaN Multiple Heterojunction (MH) LED

Further enhancement in the electronic and optical parameters is achieved by investigating a multiple heterojunction (MH) AlGaN/ GaN LED using the coupled model as shown in Figure 7.24 It consists of two 100 nm GaN layers separated by $Al_{0.3}Ga_{0.7}N$ layers to form four heterojunctions. The simulation domain is same as that of DH LED for comparison.

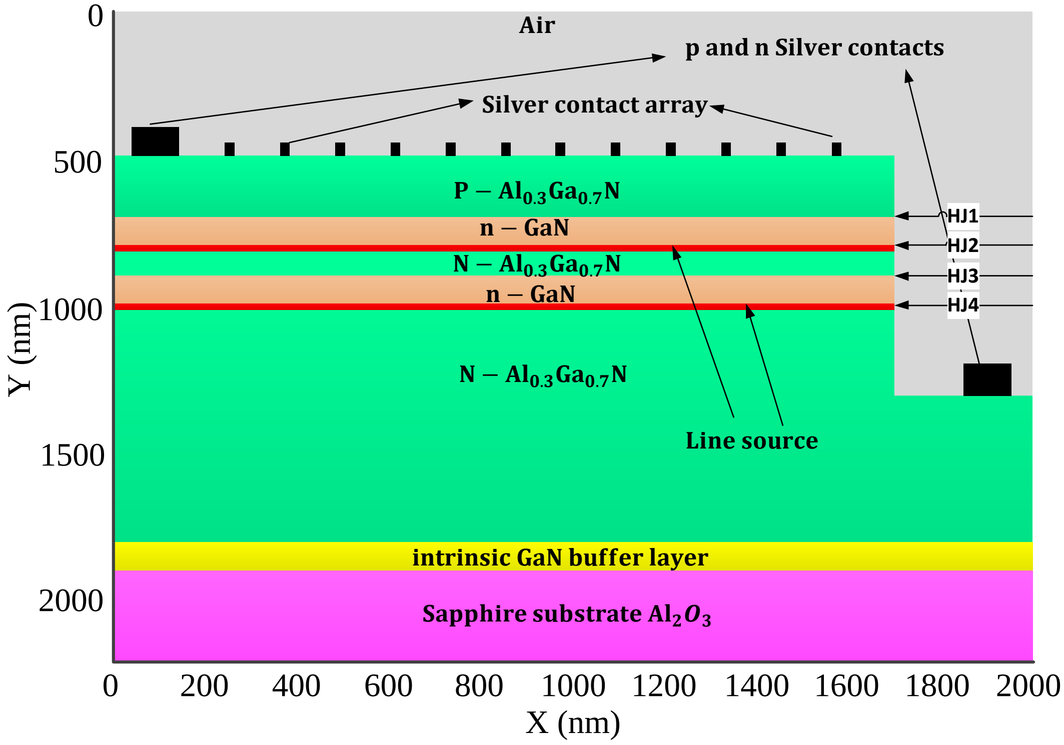

Figure 7.24 FDTD simulation domain of AlGaN/ GaN MH LED with silver contact array.

The offset in the conduction bands and valence bands at the four heterointerfaces can be seen from energy band diagram shown in Figure 7.25. This type of arrangement i.e. narrow bandgap GaN layers placed in between wide bandgap $Al_{0.3}Ga_{0.7}N$ layers increases the effective area of the radiative recombination rates because of the band offsets in the CB and VB that confines the carriers in the active region.

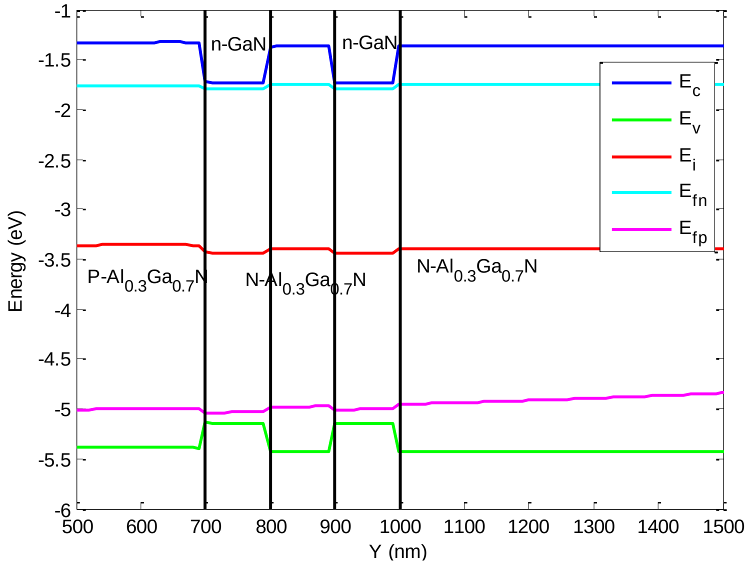

Figure 7.25 Energy band diagram of AlGaN/ GaN MH LED at forward bias.

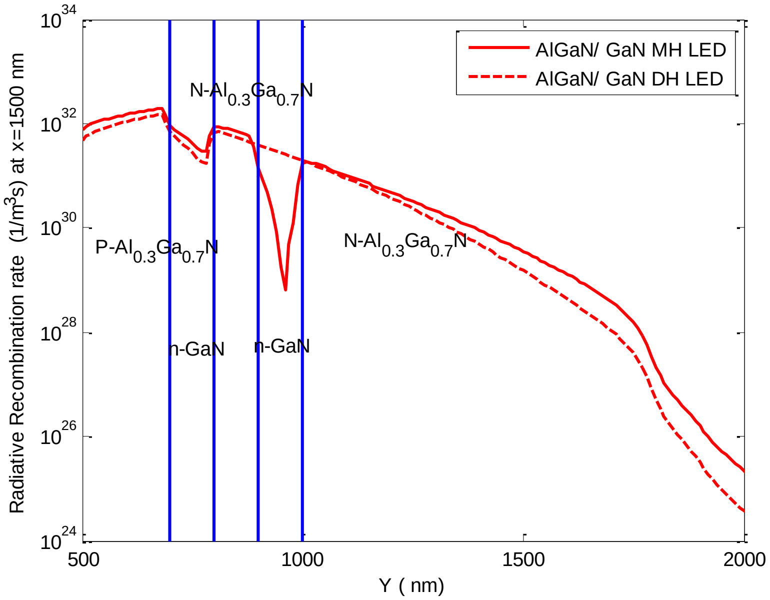

Figure 7.26 Radiative recombination rates (DH LED vs. MH LED).

The radiative recombination rates and injection currents follow the same behavior as that of DH LED i.e. they are higher with silver contact array because of high potential distribution as shown in Figure 7.27 and Figure 7.28. The injection currents of MH LED are also compared with DH LED and are found to increase with silver contact array.

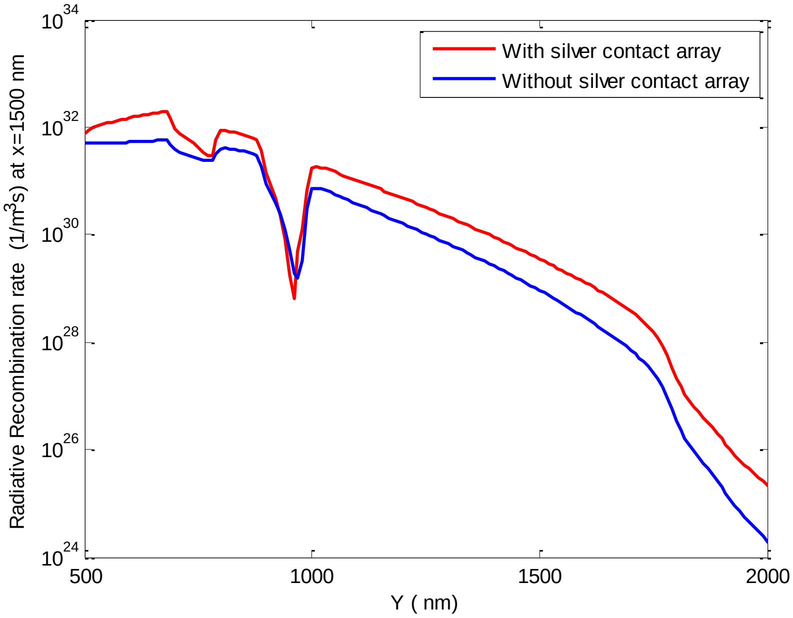

Figure 7.27 Radiative recombination rates of MH LED- With and without silver contact array

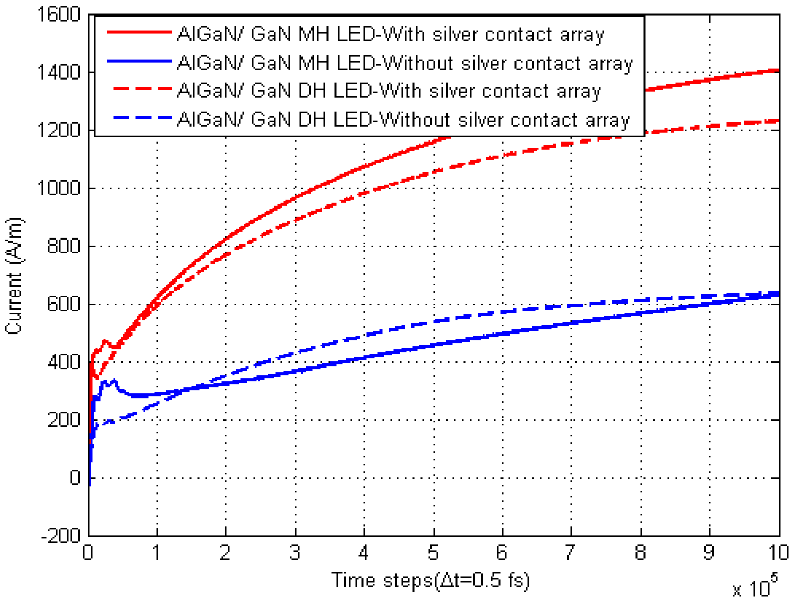

Figure 7.28 Injection currents (MH vs. DH LED).

It can be seen in Figure 7.29 that the power obtained from the optical model also increase for MH LED case because of two active GaN layers producing light. Therefore, the overall effect of two models is seen on power obtained from coupled model as shown in Figure 7.30. With these improvements, the EQE with and without silver contact array is found to be 5.295 % and 4.23 % respectively.

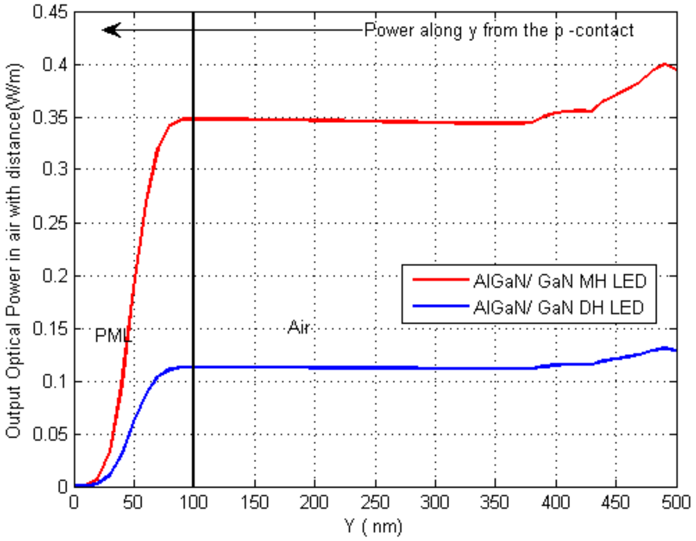

Figure 7.29 Output optical power from optical model – MH vs. DH LED.

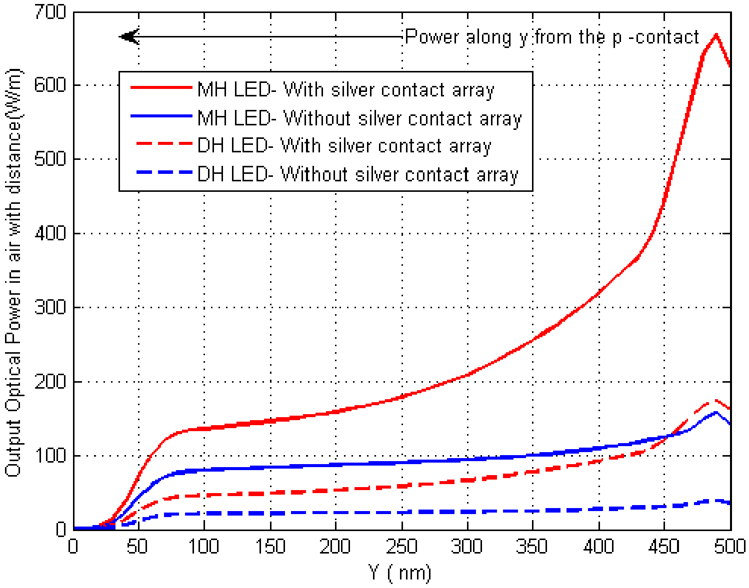

Figure 7.30 Output optical power from coupled model - MH vs. DH LED.

7.4 Summary and Discussion

Two applications demonstrating the strengths of the coupled model to investigate LED structures for improved EQEs through combined improvements in the electronic and optical characteristics are investigated. First, a DH LED with subwavelength metal contact holes (array of silver contact) instead of a single continuous contact is studied with the coupled model and the improvement in the EQE resulting from improved recombination rates, injection currents and optical power is observed. Second, a MH LED is studied that show further enhancement in the EQE due to improved recombinations and power resulting from carrier and light confinement.

CHAPTER 8

SUMMARY AND CONCLUSIONS

The coupled model can be used to simulate real time domain carrier-wave interactions in III-Nitride LEDs that cannot be performed by steady state electronic simulators or FDTD optical simulators alone. Therefore, to simulate carrier transport in conjunction with light propagation with time, the time domain electronic model coupled with the optical model is expected to find innovative applications in the field of solid state lighting. The overall summary, conclusions and future work is discussed in the following sections.

8.1 Summary and Thesis Contributions

In this thesis, a coupled time domain electronic-optical model is developed to simulate GaN LED structures for SSL applications. An FDTD-DD algorithm for simulation of carrier transport and an ADE-FDTD algorithm for simulation of light propagation are presented. The coupled model is used to study and analyze time domain carrier- photon interactions inside GaN LED structures. The research work done in this thesis is summarized as follows

- A time domain simulator for electronic and optical models is developed using DD and Maxwell’s equations respectively based on FDTD numerical technique for simulation of GaN LEDs.

- The transport properties of GaN i.e. field dependent transport models, built-in polarization models and recombination models are incorporated in the DD simulator.
- The optical properties of III-Nitride materials and metal contacts i.e. complex dielectric permittivity is modeled using multi-pole Lorentzian function.
- A coupling procedure has been developed which is based on representing electron-hole pair recombinations with the random dipole sources. The conversion of electron-hole pair recombinations to current densities is formulated by modeling a continuous time source whose weight is given by radiative recombinations gauged to an appropriate value. This weight factor is gauged by calibrating the EQE of homojunction GaN LED with the experimental value in [6].
- The FDTD analysis of p-n and p-i-n homojunction GaN LEDs, P-n-N and P-p-N double heterojunction LEDs is performed with the electronic, optical and coupled model.
- Double heterojunction and multiple heterojunction GaN/ AlGaN LEDs with holes in the metal electrode (silver contact array) are investigated as applications of the coupled model.

8.2 Conclusions

The following points can be concluded from the simulation results of GaN LED structures tested with the electronic, optical and coupled models.

- The parameters that affect the radiative recombination rates or injection currents are: the applied voltage, radiative recombination coefficients, dislocation densities and field dependent transport parameters and also the CB and VB alignment of III-Nitride materials. The recombination rates increases with applied voltage and radiative recombination coefficient as seen from electronic model results.
- Symmetric and asymmetric P-p-N DH LED simulations show that the asymmetry on P-side or high conduction band offset at P-p heterojunction increases the radiative recombinations.
- It can also be concluded that the dispersion of III-Nitride materials have a significant effect on the optical power and EQE as seen from optical model or coupled model results.
- The radiative recombination rates are found to be the major parameter in coupling the two models. On contrary, the optical generation rate calculated from coupled model has no significant effect on the solutions of the electronic model because of relatively low magnitudes as compared to recombination rates.
- For the specific simulation cases, the maximum EQE of homojunction p-n and p-i-n LEDs is found to be $0.1755\ \%$ and $0.39\ \%$ respectively, at a forward voltage of $4.267\ V$. The high EQE for p-i-n is attributed to the increase in the

recombination area by increasing the width of active region with the addition of an intrinsic layer.

- The maximum EQE of P-n-N AlGaN/GaN DH LED is found to be $1.03\,\%$ at a forward voltage of $4.101\,V$. This increase in the EQE results from high recombinations in the active region due to carrier confinement as observed from the electronic transport simulation results and low absorption inside AlGaN layers as seen from optical simulation results.
- The EQE of DH LED is improved by using an array of silver contacts instead of a single continuous contact i.e. AlGaN/ GaN DH LED with silver contact array. This structure is investigated with the coupled model as an application. The EQE is improved from $1.03\,\%$ to $1.825\,\%$. This increase is attributed to the improved current spreading and recombinations as seen from the electronic simulation and increased optical powers resulting from EOT through sub-wavelength metal contact array. However, the complexity and cost increases for this structure as compared to DH LED without silver contact array. Overall, this structure expected to find advantage over the other.
- Further enhancement in the optical powers and recombination rates is achieved by investigating a multiple heterojunction AlGaN/ GaN LED with the coupled model as a second application. The MH LED further increases the recombination area and light output due to the carrier and light confinement in the active region. The maximum EQE achieved for this LED is $4.23\,\%$ and $5.295\,\%$ with single metal contact and array of metal contacts, respectively.

8.3 Future Work

The time domain analysis offered by the coupled model can be utilized to improve the performance through combined effect of both electronic and optical simulation. Therefore, the possible extensions can be in both electronic part and optical part through innovative and new LED designs. Specific suggestions for extending this research work are:

- Combining LEDs with plasmonics is a new and exciting domain to enhance light emission through SPP resonance as seen in the application of the coupled model demonstrated. GaN LEDs with plasmonic structures of different configurations i.e. size, shape and densities can be illustrated with the coupled model to achieve high degree of enhancement through combined electronic-optical effects.
- The coupled model can be used to investigate the time domain electronic-optical characteristics of AlGaN/InGaN quantum wells or quantum dots LEDs by incorporating the quantum transport equations in the FDTD-DD algorithm.
- New designs that improve output power can be tested by reducing the total internal reflections at the air/emitter interface through roughened, patterned, textured or corrugated surfaces.
- New material models accounting the effect of temperature on the GaN LED parameters i.e. recombination coefficients, efficiencies or built-in polarizations can also be incorporated in the coupled model.

References

[1] C. J. Humphreys, "Solid-State Lighting," *MRS Bull.*, vol. 33, no. 04, pp. 459–470, 2008.

[2] M. R. Krames, O. B. Shchekin, R. Mueller-Mach, G. O. Mueller, L. Zhou, G. Harbers, and M. G. Craford, "Status and Future of High-Power Light-Emitting Diodes for Solid-State Lighting," *J. Disp. Technol.*, vol. 3, no. 2, pp. 160–175, 2007.

[3] M. H. Crawford, "LEDs for Solid-State Lighting: Performance Challenges and Recent Advances," *IEEE J. Sel. Top. Quantum Electron.*, vol. 15, no. 4, pp. 1028–1040, 2009.

[4] M. S. Shur and A. Zukauskas, "Solid-State Lighting: Toward Superior Illumination," *Proc. IEEE*, vol. 93, no. 10, pp. 1691–1703, 2005.

[5] H. Amano, M. Kito, K. Hiramatsu, and I. Akasaki, "P-Type Conduction in Mg-Doped GaN Treated with Low-Energy Electron Beam Irradiation (LEEBI)," *Jpn. J. Appl. Phys.*, vol. 28, no. Part 2, No. 12, pp. L2112–L2114, 1989.

[6] S. Nakamura, T. Mukai, and M. Senoh, "High-Power GaN P-N Junction Blue-Light-Emitting Diodes," *Jpn. J. Appl. Phys.*, vol. 30, no. Part 2, No. 12A, pp. L1998–L2001, 1991.

[7] S. Nakamura, M. Senoh, and T. Mukai, "High-power InGaN/GaN double-heterostructure violet light emitting diodes," *Appl. Phys. Lett.*, vol. 62, no. 19, pp. 2390–2392, May 1993.

[8] E. F. Schubert, *Light-Emitting Diodes*. Cambridge University Press, 2006.

[9] E. F. Schubert and J. K. Kim, "Solid-State Light Sources Getting Smart," *Science*, vol. 308, no. 5726, pp. 1274–1278, May 2005.

[10] L. M. Tolbert, B. Ozpineci, S. K. Islam, and M. S. Chinthavalli, "Wise Bandgap Semiconductors for Utility Applications," presented at the Power and Energy Systems.

[11] R. T. Kemerley, H. B. Wallace, and M. N. Yoder, "Impact of wide bandgap microwave devices on DoD systems," *Proc. IEEE*, vol. 90, no. 6, pp. 1059–1064, Jun. 2002.

[12] W. Fichtner, D. J. Rose, and R. E. Bank, "Semiconductor Device Simulation," *SIAM J. Sci. Stat. Comput.*, vol. 4, no. 3, pp. 391–415, Sep. 1983.

[13] C. M. Snowden, “Semiconductor device modelling,” *Reports Prog. Phys.*, vol. 48, no. 2, p. 223, Feb. 1985.

[14] R. E. Bank, D. J. Rose, and W. Fichtner, “Numerical methods for semiconductor device simulation,” *IEEE Trans. Electron Devices*, vol. 30, no. 9, pp. 1031–1041, Sep. 1983.

[15] C. M. Snowden and E. Snowden, *Introduction to Semiconductor Device Modelling*. World Scientific, 1998.

[16] M. N. O. Sadiku, *Numerical Techniques in Electromagnetics, Second Edition*. CRC Press, 2000.

[17] S. J. Pearton, C. R. Abernathy, M. E. Overberg, G. T. Thaler, A. H. Onstine, B. P. Gila, F. Ren, B. Lou, and J. Kim, “New applications advisable for gallium nitride,” *Mater. Today*, vol. 5, no. 6, pp. 24–31, Jun. 2002.

[18] S. Nakamura, M. Senoh, and T. Mukai, “P-GaN/N-InGaN/N-GaN Double-Heterostructure Blue-Light-Emitting Diodes,” *Jpn. J. Appl. Phys.*, vol. 32, no. Part 2, No. 1A/B, pp. L8–L11, 1993.

[19] B. Monemar and G. Pozina, “Group III-nitride based hetero and quantum structures,” *Prog. Quantum Electron.*, vol. 24, no. 6, pp. 239–290, Nov. 2000.

[20] B. S. Mashford, M. Stevenson, Z. Popovic, C. Hamilton, Z. Zhou, C. Breen, J. Steckel, V. Bulovic, M. Bawendi, S. Coe-Sullivan, and P. T. Kazlas, “High-efficiency quantum-dot light-emitting devices with enhanced charge injection,” *Nat. Photonics*, vol. 7, no. 5, pp. 407–412, May 2013.

[21] J. Piprek, T. M. Katona, S. P. DenBaars, and S. Li, “3D simulation and analysis of AlGaN/GaN ultraviolet light-emittings diodes,” 2004, vol. 5366, pp. 127–136.

[22] Y.-K. Kuo, T.-H. Wang, and J.-Y. Chang, “Blue InGaN Light-Emitting Diodes With Multiple GaN-InGaN Barriers,” *IEEE J. Quantum Electron.*, vol. 48, no. 7, pp. 946–951, 2012.

[23] J. Piprek, “Efficiency droop in nitride-based light-emitting diodes,” *Phys. Status Solidi*, vol. 207, no. 10, pp. 2217–2225, 2010.

[24] A. A. Efremov, N. I. Bochkareva, R. I. Gorbunov, D. A. Lavrinovich, Y. T. Rebane, D. V. Tarkhin, and Y. G. Shreter, “Effect of the joule heating on the quantum efficiency and choice of thermal conditions for high-power blue InGaN/GaN LEDs,” *Semiconductors*, vol. 40, no. 5, pp. 605–610, May 2006.

[25] T. Lu, S. Li, K. Zhang, C. Liu, Y. Yin, L. Wu, H. Wang, X. Yang, G. Xiao, and Y. Zhou, “Effect of the thickness of undoped GaN interlayers between multiple quantum wells and the p-doped layer on the performance of GaN light-emitting diodes,” *Opt. Express*, vol. 19, no. 19, pp. 18319–18323, Sep. 2011.

[26] G. Traetta, A. Passaseo, M. Longo, D. Cannoletta, R. Cingolani, M. Lomascolo, A. Bonfiglio, A. D. Carlo, F. D. Sala, P. Lugli, A. Botchkarev, and H. Morkoç, "Effects of the spontaneous polarization and piezoelectric fields on the luminescence spectra of GaN/Al0.15Ga0.85N quantum wells," *Phys. E Low-Dimens. Syst. Nanostructures*, vol. 7, no. 3–4, pp. 929–933, May 2000.

[27] J. Piprek and S. Li, "Electron leakage effects on GaN-based light-emitting diodes," *Opt. Quantum Electron.*, vol. 42, no. 2, pp. 89–95, Jan. 2010.

[28] C. Wiesmann, K. Bergenek, N. Linder, and U. t. Schwarz, "Photonic crystal LEDs – designing light extraction," *Laser Photonics Rev.*, vol. 3, no. 3, pp. 262–286, Apr. 2009.

[29] Y. Fu, K. Li, and F. Kong, "ANALYSIS OF THE OPTICAL TRANSMISSION THROUGH THE METAL PLATE WITH SLIT ARRAY," *Prog. Electromagn. Res.*, vol. 82, pp. 109–125, 2008.

[30] L. Landström, D. Brodoceanu, D. Bäuerle, F. J. Garcia-Vidal, S. G. Rodrigo, and L. Martin-Moreno, "Extraordinary transmission through metal-coated monolayers of microspheres," *Opt. Express*, vol. 17, no. 2, pp. 761–772, Jan. 2009.

[31] C.-H. Chan, C.-H. Hou, S.-Z. Tseng, T.-J. Chen, H.-T. Chien, F.-L. Hsiao, C.-C. Lee, Y.-L. Tsai, and C.-C. Chen, "Improved output power of GaN-based light-emitting diodes grown on a nanopatterned sapphire substrate," *Appl. Phys. Lett.*, vol. 95, no. 1, p. 011110, Jul. 2009.

[32] F. M. Abou El-Ela and A. Z. Mohamed, "Electron Transport Characteristics of Wurtzite GaN," *ISRN Condens. Matter Phys.*, vol. 2013, pp. 1–6, 2013.

[33] V. O. Turin, "A modified transferred-electron high-field mobility model for GaN devices simulation," *Solid-State Electron.*, vol. 49, no. 10, pp. 1678–1682, Oct. 2005.

[34] M. Farahmand, C. Garetto, E. Bellotti, K. F. Brennan, M. Goano, E. Ghillino, G. Ghione, J. D. Albrecht, and P. P. Ruden, "Monte Carlo simulation of electron transport in the III-nitride wurtzite phase materials system: binaries and ternaries," *IEEE Trans. Electron Devices*, vol. 48, no. 3, pp. 535–542, 2001.

[35] L.-A. Yang, Y. Hao, Q. Yao, and J. Zhang, "Improved Negative Differential Mobility Model of GaN and AlGaN for a Terahertz Gunn Diode," *IEEE Trans. Electron Devices*, vol. 58, no. 4, pp. 1076–1083, 2011.

[36] E. Bellotti and F. Bertazzi, "Transport Parameters for Electrons and Holes," in *Nitride Semiconductor Devices: Principles and Simulation*, J. Piprek, Ed. Wiley-VCH Verlag GmbH & Co. KGaA, 2007, pp. 69–93.

[37] N. D. Arora, J. R. Hauser, and D. J. Roulston, “Electron and hole mobilities in silicon as a function of concentration and temperature,” *IEEE Trans. Electron Devices*, vol. 29, no. 2, pp. 292–295, 1982.

[38] S. Wang, H. Liu, J. Fan, F. Ma, and X. Lei, “Anisotropic longitudinal electron diffusion coefficient in wurtzite gallium nitride,” *Appl. Phys.*, vol. 112, no. 4, pp. 933–938, Sep. 2013.

[39] F. Bernardini, “Spontaneous and Piezoelectric Polarization: Basic Theory vs. Practical Recipes,” in *Nitride Semiconductor Devices: Principles and Simulation*, J. Piprek, Ed. Wiley-VCH Verlag GmbH & Co. KGaA, 2007, pp. 49–68.

[40] F. Bernardini and V. Fiorentini, “Polarization fields in nitride nanostructures: 10 points to think about,” *Appl. Surf. Sci.*, vol. 166, no. 1–4, pp. 23–29, Oct. 2000.

[41] T. J. Kim, J. S. Byun, Y. D. Kim, Y.-C. Chang, and H. Kim, “Optical Properties of GaN by Using Ellipsometry and a Band Calculation,” *J. Korean Phys. Soc.*, vol. 53, no. 3, p. 1575, Sep. 2008.

[42] E. T. Yu, X. Z. Dang, P. M. Asbeck, S. S. Lau, and G. J. Sullivan, “Spontaneous and piezoelectric polarization effects in III #x2013;V nitride heterostructures,” *J. Vac. Sci. Technol. B Microelectron. Nanometer Struct.*, vol. 17, no. 4, pp. 1742–1749, 1999.

[43] R. Mirzavand, A. Abdipour, G. Moradi, and M. Movahhedi, “Full-wave semiconductor devices simulation using meshless and finite-difference time-domain approaches,” *IET Microwaves Antennas Propag.*, vol. 5, no. 6, pp. 685–691, Apr. 2011.

[44] Q. Dai, Q. Shan, J. Wang, S. Chhajed, J. Cho, E. F. Schubert, M. H. Crawford, D. D. Koleske, M.-H. Kim, and Y. Park, “Carrier recombination mechanisms and efficiency droop in GaInN/GaN light-emitting diodes,” *Appl. Phys. Lett.*, vol. 97, no. 13, p. 133507, Sep. 2010.

[45] A. E. Chernyakov, M. M. Sobolev, V. V. Ratnikov, N. M. Shmidt, and E. B. Yakimov, “Nonradiative recombination dynamics in InGaN/GaN LED defect system,” *Superlattices Microstruct.*, vol. 45, no. 4–5, pp. 301–307, Apr. 2009.

[46] H. Z. Ronald A Arif, “Radiative efficiency and spontaneous recombination rate of staggered InGaN quantum well LED at 420-510 nm,” 2008.

[47] S. Y. Karpov, “Visible Light-Emitting Diodes,” in *Nitride Semiconductor Devices: Principles and Simulation*, J. Piprek, Ed. Wiley-VCH Verlag GmbH & Co. KGaA, 2007, pp. 303–325.

[48] Y. C. Shen, G. O. Mueller, S. Watanabe, N. F. Gardner, A. Munkholm, and M. R. Krames, “Auger recombination in InGaN measured by photoluminescence,” *Appl. Phys. Lett.*, vol. 91, no. 14, p. 141101, Oct. 2007.

[49] J. Iveland, L. Martinelli, J. Peretti, J. S. Speck, and C. Weisbuch, “Direct Measurement of Auger Electrons Emitted from a Semiconductor Light-Emitting Diode under Electrical Injection: Identification of the Dominant Mechanism for Efficiency Droop,” *Phys. Rev. Lett.*, vol. 110, no. 17, p. 177406, Apr. 2013.

[50] L. Riuttanen, P. Kivisaari, N. Mäntyoja, J. Oksanen, M. Ali, S. Suihkonen, and M. Sopanen, “Recombination lifetime in InGaN/GaN based light emitting diodes at low current densities by differential carrier lifetime analysis,” *Phys. Status Solidi C*, vol. 10, no. 3, pp. 327–331, 2013.

[51] G. Kim, J. H. Kim, E. H. Park, D. Kang, and B.-G. Park, “Extraction of recombination coefficients and internal quantum efficiency of GaN-based light emitting diodes considering effective volume of active region,” *Opt. Express*, vol. 22, no. 2, pp. 1235–1242, Jan. 2014.

[52] M. A. AlSunaidi and A. A. Al-Jabr, “A General ADE-FDTD Algorithm for the Simulation of Dispersive Structures,” *IEEE Photonics Technol. Lett.*, vol. 21, no. 12, pp. 817–819, 2009.

[53] W. H. P. Pernice, F. P. Payne, and D. F. G. Gallagher, “An FDTD method for the simulation of dispersive metallic structures,” *Opt. Quantum Electron.*, vol. 38, no. 9–11, pp. 843–856, Jul. 2006.

[54] K. S. Yee, “Numerical solution of initial boundary value problems involving Maxwell’s equations in isotropic media,” *IEEE Trans Antennas Propag.*, pp. 302–307, 1966.

[55] A. Taflove and S. C. Hagness, *Computational electrodynamics: the finite-difference time-domain method*. Boston: Artech House, 2005.

[56] G. I. Marcuk and G. I., Marcuk, Gurij Ivanovic, Marcuk, Gurij Ivanovic Marcuk, *Methods of numerical mathematics*. New York, Springer, 1982.

[57] A. Nicholls and B. Honig, “A rapid finite difference algorithm, utilizing successive over-relaxation to solve the Poisson–Boltzmann equation,” *J. Comput. Chem.*, vol. 12, no. 4, pp. 435–445, 1991.

[58] J.-P. Berenger, “A perfectly matched layer for the absorption of electromagnetic waves,” *J. Comput. Phys.*, vol. 114, no. 2, pp. 185–200, Oct. 1994.

[59] A.-P. Zhao, J. Juntunen, and A. V. Raisanen, “Generalized material-independent PML absorbers for the FDTD simulation of electromagnetic waves in arbitrary anisotropic dielectric and magnetic media,” *IEEE Microw. Guid. Wave Lett.*, vol. 8, no. 2, pp. 52–54, 1998.

[60] M. E. Levinshtein, S. L. Rumyantsev, and M. S. Shur, *Properties of Advanced Semiconductor Materials: GaN, AIN, InN, BN, SiC, SiGe*. John Wiley & Sons, 2001.

[61] S. P. Grabowski, M. Schneider, H. Nienhaus, W. Mönch, R. Dimitrov, O. Ambacher, and M. Stutzmann, “Electron affinity of AlxGa1−xN(0001) surfaces,” *Appl. Phys. Lett.*, vol. 78, no. 17, pp. 2503–2505, Apr. 2001.

[62] M. S. Lundstrom and R. J. Schuelke, “Modeling semiconductor heterojunctions in equilibrium,” *Solid-State Electron.*, vol. 25, no. 8, pp. 683–691, Aug. 1982.

[63] K. Horio and H. Yanai, “Numerical modeling of heterojunctions including the thermionic emission mechanism at the heterojunction interface,” *IEEE Trans. Electron Devices*, vol. 37, no. 4, pp. 1093–1098, Apr. 1990.

[64] R. Goldhahn, C. Buchheim, P. Schley, A. T. Winzer, and H. Wenzel, “Optical Constants of Bulk Nitrides,” in *Nitride Semiconductor Devices: Principles and Simulation*, J. Piprek, Ed. Wiley-VCH Verlag GmbH & Co. KGaA, 2007, pp. 95–115.

[65] A. D. Rakic, A. B. Djuri?ic, J. M. Elazar, and M. L. Majewski, “Optical Properties of Metallic Films for Vertical-Cavity Optoelectronic Devices,” *Appl. Opt.*, vol. 37, no. 22, pp. 5271–5283, Aug. 1998.

[66] G. Sun, J. B. Khurgin, and R. A. Soref, “Plasmonic light-emission enhancement with isolated metal nanoparticles and their coupled arrays,” *J. Opt. Soc. Am. B*, vol. 25, no. 10, pp. 1748–1755, Oct. 2008.

[67] Y. Alaverdyan, B. Sepúlveda, L. Eurenius, E. Olsson, and M. Käll, “Optical antennas based on coupled nanoholes in thin metal films,” *Nat. Phys.*, vol. 3, no. 12, pp. 884–889, Dec. 2007.

[68] G. Lozano, D. J. Louwers, S. R. Rodríguez, S. Murai, O. T. Jansen, M. A. Verschuuren, and J. Gómez Rivas, “Plasmonics for solid-state lighting: enhanced excitation and directional emission of highly efficient light sources,” *Light Sci. Appl.*, vol. 2, no. 5, p. e66, May 2013.

[69] S. A. Maier and H. A. Atwater, “Plasmonics: Localization and guiding of electromagnetic energy in metal/dielectric structures,” *J. Appl. Phys.*, vol. 98, no. 1, pp. 011101–011101–10, Jul. 2005.

Vitae

Name	: Mohammed Zia Ullah Khan
Nationality	: Indian
Date of Birth	: 4/13/1990
Email	: mz29.khan@gmail.com, mdzia@kfupm.edu.sa
Address	: House # 8-9-76/3, Plot # B/1, Dhatu Nagar, Midhani Enclave, Hyderabad, India, 500058
Academic Background	: Master of Science (M.S) in Electrical Engineering (Major: Photonics/Electromagnetics), KFUPM, April 2014, 3.857/4 GPA. Bachelor of Engineering (B.E) in Electronics and Communication Engineering, Osmania University, Hyderabad, June 2011, First-class Honors with Distinction, 89.96%
Work Experience	: Worked as a Research Assistant at Center of Research Excellence in Renewable Energy (CoRE-RE), Research Institute, KFUPM, Sept. 2011-May 2014.

Research Publications : **M. Ziaullahkhan**, M.T.M. Mujahid, and M. Alsunaidi. “TE Photonic Modes in Metal-insulator-metal Structures.” In Electronics, Communications and Photonics Conference (SIECPC), 2013 Saudi International, 1–4, 2013. *(IEEE Xplore).*

M. Ziaullahkhan and M. A. Alsunaidi, “Photonic TE Modes in Metal-Insulator-Metal Waveguides,” *META’13-4th International Conference on Metamaterials, Photonic Crystals, and Plasmonics*, Sharjah, UAE, March 2013 *(Conference Proceedings).*

(Invited) W.W. Ahmed, M. T. Mujahid, **M. Ziaullahkhan** and M. A. Alsunaidi, “Light extraction enhancement of GaN Light emitting diodes,” 2nd IEEE International Conference on Electronics, Communication, and Photonics (SIECPC), Riyadh, Saudi Arabia, April 2013.